MICROFLUIDIC LOGIC DEVICES AND CIRCUITS

By

RUCHI GUPTA, B.Eng.

A Thesis
Submitted to the School of Graduate Studies
in Partial Fulfilment of the Requirements
for the Degree
Master of Applied Science

McMaster University

MICROFLUIDIC LOGIC DEVICES AND CIRCUITS

MASTER OF APPLIED SCIENCE (2007)
(Engineering Physics)

McMaster University
Hamilton, Ontario

TITLE: MICROFLUIDIC LOGIC DEVICES AND CIRCUITS

AUTHOR: Ruchi Gupta, B.Eng. (Nanyang Technological University, Singapore)

SUPERVISOR: Dr. Rafael N. Kleiman

NUMBER OF PAGES: xvi, 149

ABSTRACT

The motivation for this project is to mimic an electronic microprocessor in the fluidic domain to enable on-chip decision making for lab-on-a-chip applications. Microfabrication can increase the economic feasibility of microfluidic computing by lowering the cost per chip. Monolithic integration also has the potential to reduce the packaging costs and reduce the interconnect delays.

In this thesis a high reliability no-moving part microfluidic NOR gate was modeled and optimized using modern and widely-accepted computational fluid dynamics tools. Our optimized microfluidic NOR satisfies all the stringent device requirements needed to make a computing system. The transfer curves are non-linear, the fan-out is greater than 12, the input and output signals are in the same domain and the flow of information is only in one direction. Fabricating the microfluidic circuits with components of a single fixed geometry is very attractive. The NOR is a universal gate and thus all logic functions can be realized by a combination of NORs.

Three important components of computing: a half adder, a static memory/latch and a clock were also modeled. We have also studied the dynamics of the device, and have understood the origin of the switching time. The performance of the device is only dependent on the Reynolds number of the supply jet. Thus the performance of the device for any fluid: air, water, oil etc, will remain unaltered at the same Reynolds number. Based on our understanding of the power vs. geometry we can predict the critical dimension of the device that can operate at the desirable power consumption.

Finally, we envision applying the designed microfluidic NOR to a newly emerging technology – i.e. Lab-on-a-chip. We envision fabricating an integrated assembly of microfluidic devices to make a microfluidic processor for lab-on-a-chip systems. This work could have a major impact for biomedical applications.

ACKNOWLEDGEMENTS

First and foremost I would like to thank my supervisor Dr. Rafael N. Kleiman for giving me an opportunity to carry out this research. This research wouldn't have been completed without his invaluable suggestions. I learnt from him that the best way to find an optimized point in an infinitely huge space is to be systematic. Thesis writing was a daunting process, but thanks for being patient to teach me something as simple as fitting curves using origin.

I am also grateful to Dr. Ravi Selavaganapathy for his advice and suggestions. He was very encouraging at the time when my research wasn't progressing at all and I had no clue of how to progress.

I decided to be a graduate student at McMaster University because of the wonderful experience I had here when I was an exchange student in 2003. The opportunity to return here as a graduate student was like a dream come true. Thanks to Nanyang Technological University, Singapore and my parents who encouraged me to participate in the exchange program.

I would also like to thank my colleagues and friends who have helped me both academically and socially. In particular I am grateful to Sherif Abdou who helped in learning ANSYS-CFX. Edgar Huante Ceron and Andrey Zdanovich helped in reading the initial drafts which were full of unorganized thoughts. Special thanks to Yuan He, Edgar Huante Ceron, Ali Abu-El-Magd, Andrey Zdanovich and Zareena for making this place a home away from home.

I would like to express my gratitude to Mrs. Natalie Sobel for her help in the initial months to adjust to the new place. I am also grateful to my friend's parents for spending

their several weekends with me. And thanks aunty for packing the nicest food I could find here on my way back to the hostel.

Finally, I would like to thank my parents and sisters for their constant support, patience, encouragement and love. Mom, you have supported me so much that I know I couldn't have done this without you. Moving to Canada to do my graduate studies was a big decision for me. Thank you very much for supporting my decision. I wouldn't have been here without your support. Thanks for taking care of me – for reminding me not to skip my meals. Thanks for being my banker dad! Thanks Ritu and Rinku for making me smile with your cute jokes.

TABLE OF CONTENTS

Topic **Page**

Abstract.. iii

Acknowledgements.. iv

Table of Contents.. vi

List of Figures.. ix

List of Tables.. xvi

Chapter 1 Overview... 1

1.1 Introduction.. 1

1.2 Outline... 5

Chapter 2 Fluidic Logic... 6

2.1 Momentum interaction devices................................. 6

2.2 Wall-attachment or Coanda effect devices.................... 10

2.3 Turbulence amplifiers.. 12

2.4 Vortex devices.. 14

Chapter 3 Laminar NOR (Walker and Trask, 1967) 16

Chapter 4 Recent Microfluidic Logic.. 27

4.1 Logic using special fluids... 27

4.2 Logic using nonlinearities in the system functional response 28

4.3 Turbulent regime flip-flop and AND gate........................ 28

4.4 A microfluidic amplifier.. 30

4.5 A microfluidic oscillator.. 31

Topic **Page**

Chapter 5 Introduction to Boolean logic and digital circuits.............. 33

Chapter 6 Computational Fluid Dynamics..................................... 40

Chapter 7 Results and Discussions.. 43
  7.1 Vent near outlet.. 50
  7.2 Optimization... 55
    7.2.1 Width of control ports...................................... 56
    7.2.2 Outlet width.. 59
    7.2.3 Length of the device.. 66
  7.3 Transfer curves of a loaded element & driven elements.... 77
  7.4 Constant velocity vs. constant pressure supply............... 89
    7.4.1 Symmetrical performance of control ports A and B for constant supply velocity.............................. 89
    7.4.2 Symmetrical performance of control ports A and B for constant supply pressure.............................. 92
  7.5 Reynolds number scaling... 99

Chapter 8 Fundamental Dependencies.. 105
  8.1 Geometry scaling.. 105
  8.2 Switching time vs. geometry..................................... 108
  8.3.1 Power vs. geometry.. 109
  8.3.2 Temperature change vs. geometry............................ 110
  8.4 Summary of scaling at constant Reynolds number 111
  8.5 Physical basis for non-linearity in transfer curves........... 111

Topic **Page**

8.6 Physical basis for switching time.................................. 117

8.6.1 Transit time (τ_T)... 121

8.6.2 Jet deflection time (τ_J)....................................... 123

Chapter 9 Microfluidic logic devices... 126

9.1 Half adder.. 126

9.2 Clock... 129

9.3 Latch... 133

Chapter 10 Conclusions... 137

10.1 Device design and capabilities.................................. 137

10.2 Suitability for lab-on-a-chip....................................... 138

Chapter 11 Future work 142

References.. 146

Appendix... 149

LIST OF FIGURES

No **Description** **Pg**

Figure 1-1 Advantages of information processing in the microfluidic domain over information processing in the electrical domain.................... 2

Figure 2-1 Momentum interaction of two jets 7

Figure 2-2 Momentum interaction EQUIVALENCE gate............................ 9

Figure 2-3 Momentum interaction AND gate.. 9

Figure 2-4 A laminar jet entraining fluid particles on all sides....................... 10

Figure 2-5 Jet deflecting from the centerline and attaching to one of the walls due to wall-attachment or Coanda effect.................................. 11

Figure 2-6 Geometric parameters studied in late 1960s for wall-attachment effect.. 12

Figure 2-7 Turbulence Amplifier (a) ON state (b) OFF state......................... 13

Figure 2-8 A vortex diode.. 14

Figure 2-9 Swirl motion of a vortex diode in the backward flow direction......... 15

Figure 3-1 Basic NOR geometry considered in an investigation in 1967........... 17

Figure 3-2 Momentum and pressure interaction of a jet and flow.................... 18

Figure 3-3 (a) A=0, B=0, ON-state, (b) A=1, B=0, OFF-state, (c) A=0, B=1, OFF-state and (d) A=1, B=1, OFF-state.................................... 21

Figure 3-4 (a): Transfer curves and (b) output characteristic curve, load line and the minimum pressure required to switch the device from ON to OFF for first control port and second control port............................. 22

Figure 3-5 Velocity profile when 10KPa is applied to (a) first control port and (b) second control port (xy plane at z=25μm)............................ 24

Figure 4-1 Microfluidic electrochemical diode... 27

Figure 4-2 Bistable flip-flop... 29

Figure 4-3 AND gate... 30

No **Description** **Pg**

Figure 4-4 Schematic of microfluidic amplifier.. 31
Figure 4-5 Schematic of microfluidic oscillator.. 32
Figure 5-1 General block diagram of a logic gate circuit............................... 33
Figure 5-2 An AND gate using a combination of NORs.............................. 36
Figure 5-3 (a) Half adder (b) clock and (c) latch realized by cascading NOR gates.. 38
Figure 5-4 A transfer curve which has a lower susceptibility to variations......... 39
Figure 6-1 A picture showing finer mesh regions in our model...................... 41
Figure 7-1 An arbitrary transfer curve$\left(y = 0.5\tanh(5(0.5 - x) + 1)\right)$................ 44
Figure 7-2 A value above Pc* regress to maximum..................................... 45
Figure 7-3 (a) Transfer characteristic curve (L=15w, W_c=90μm, W_o=2w and Re=600).. 46
Figure 7-3 (b) Output characteristic curve (L=15w, W_c=90μm, W_o=2w and Re=600).. 47
Figure 7-3 (c) Load line (L=15w, W_c=90μm, W_o=2w and Re=600)............... 48
Figure 7-4 A plot showing the superimposed Pc* obtained from the transfer curve, output characteristic curve and the load line (L=15w, W_c=90μm, W_o=2w and Re=600)... 49
Figure 7-5 First modeled NOR (Width of supply nozzle=50μm, height=50μm and length=750μm)... 50
Figure 7-6 Low output pressure recovery (xy plane at z=25μm)..................... 50
Figure 7-7 Design with symmetrical vents (Width of supply nozzle=50μm, height=50μm and length=750μm).. 51
Figure 7-8 Increased output pressure for a symmetrical design (xy plane at z=25μm) 52
Figure 7-9 Transfer curves of a device with symmetrical vents (L=15w, W_o=1.5w, W_c= 70μm & 100μm, Re~600 and P_{omax}=P_{cmax}=20KPa)... 53

No **Description** **Pg**

Figure 7-10 Design with straight bottom wall and a vent close to the outlet (size and position of the bottom vent are also marked)........................54

Figure 7-11 Transfer curves of a design with symmetrical vents and a design with a straight bottom wall and a vent close to the outlet (L=15w, W_o=1.5w, Re~600 and $P_{omax}=P_{cmax}$=20KPa)............................55

Figure 7-12 Design used for optimization..56

Figure 7-13 Transfer functions for different widths of the control port (Re~600, L=15w, W_o=1.5w and $P_{omax}=P_{cmax}$=20KPa).....................................57

Figure 7-14 Fan-out as a function of control port width (Re~600, L=15w, W_o=1.5w)...58

Figure 7-15 Explanation for a point of maximum fan-out with respect to control port width (Re~600, L=15w and W_o=1.5w)..................................59

Figure 7-16 Transfer function for different outlet width (Re~600, L=15w, $P_{omax}=P_{cmax}$=20KPa and W_c corresponding to $P_c^*=P_{omax}/2$).................60

Figure 7-17 Fan-out vs. outlet width (Re~600, L=15w and W_c corresponding to $P_c^*=P_{omax}/2$)...62

Figure 7-18 (a) Explanation for a point of maximum fan-out with respect to outlet width for L=15w (Re~600 and W_c corresponding to $P_{c\_min}=P_{omax}/2$)...63

Figure 7-18 (b)Explanation for a point of maximum fan-out with respect to outlet width for L=18w (Re~600 and W_c corresponding to $P_{c\_min}=P_{omax}/2$)...64

Figure 7-18 (c)Explanation for a point of maximum fan-out with respect to outlet width for L=21w (Re~600 and W_c corresponding to $P_{c\_min}=P_{omax}/2$)...65

Figure 7-18 (d)Explanation for a point of maximum fan-out with respect to outlet width for L=24w (Re~600 and W_c corresponding to $P_{c\_min}=P_{omax}/2$)...66

Figure 7-19 Fan-out vs. outlet width for different lengths (Re~600 and W_c satisfying Equation 7-1)...67

Figure 7-20 Plot of the output width corresponding to maximum fan-out (W_o^*) vs. Length (L)..68

No **Description** **Pg**

Figure 7-21 Plot of no-load mass flow rate through the outlet for varying outlet width for different lengths and Reynolds number~600.................. 69

Figure 7-22 Outlet width to capture ~90% of the supply jet for different lengths and Reynolds number~600... 70

Figure 7-23 Maximum fan-out vs. length (Re~600).......................................71

Figure 7-24 The angle (θ^*) by which the jet has to deflected to turn the device from ON to OFF and vice-versa... 72

Figure 7-25 A plot of W_c^* for L=15w to L=24w..75

Figure 7-26 Plot of Q_c vs. P_c without the supply jet, with a supply jet of Re~300 and with a supply jet of Re~600 (W_c=80μm).............................. 76

Figure 7-27 Plot of Q_c vs. P_c without the supply jet, with a supply jet of Re~300 and with a supply jet of Re~600 (L=18w, W_o=3.5w and W_c=80μm)...79

Figure 7-28 An inset showing ΔP_{in} and plane AA' (L=18w, W_o=3.5w and W_c=80μm)...80

Figure 7-29 (a) Plot of Q_c vs. ΔP_{in} to obtain the input impedance of the device with a supply jet of Re=600 (L=18w, W_o=3.5w and W_c=80μm)....... 81

Figure 7-29 (b) Plot of control port impedance vs. ΔP_{in} to obtain the control impedance of the device with a supply jet of Re=600 (L=18w, W_o=3.5w & W_c=80μm)... 82

Figure 7-29 (c)Plot comparing Q vs. P of a square cross-section (50μm×50μm) of different lengths and Qc vs. P_c (L=18w, W_o=3.5w & W_c=80μm and Re~600)...83

Figure 7-30 (a) Figure showing one dummy load reflected geometrically........... 84

Figure 7-30 (b) Figure showing five dummy load reflected geometrically...........84

Figure 7-31 Plot of the transfer curve of an element for different loading conditions (L=18w, W_o=3w, W_c=80μm and Re~600)...................86

No **Description** **Pg**

Figure 7-32 Derivative of transfer curves of the driven elements when the driving element was loaded with different number of elements (L=18w, W_o=3w, W_c=80μm and Re~600).. 87
Figure 7-34 A design with a vent adjacent to the second control port................ 90
Figure 7-35 (a) Transfer curves for the first and second control ports for the design with a vent downstream of the second control port..............91
Figure 7-35 (b) Fan-out for the first and second control ports for the design with a92 vent adjacent to the second control port...................................
Figure 7-36 Microfluidic NOR...93
Figure 7-37 Change in supply velocity on applying higher control pressures to the first control port at constant supply pressure (a) P_s=20KPa, P_{c1}=0KPa and V_s=10m/s (b) P_s=20KPa, P_{c1}=16KPa and V_s=5.28m/s (xy plane and z=25μm)..94
Figure 7-38 (a) The output curve and load line for constant pressure supply and constant velocity of both the control ports................................95
Figure 7-37 (b) The transfer curves for constant pressure supply and constant velocity of both the control ports..96
Figure 7-39 (a) Design with a vent upstream of the first control..........................97
Figure 7-39 (b) Velocity profile for the design with vent A, P_s=20KPa, P_{c1}=16KPa and V_s=10m/s (xy plane and z=25μm)...................... 97
Figure 7-40 Transfer curve of the first and the second control ports with vent A...98
Figure 7-41 Plot of no-load mass flow rate through the outlet for varying outlet width for different lengths and Reynolds number....................... 99
Figure 7-42 Outlet width to capture 65% of the supply jet for different lengths and Reynolds number..100
Figure 7-43 Velocity profile of a supply jet of Reynolds number (a) 300 and (b) 600 (xy plane and z=25μm)... 102

No **Description** **Pg**

Figure 7-44 (a) Transfer curves at Re~300 and Re~600 (L=12w, W_o=1.5w and W_c=50µm)..103

Figure 7-44 (b) The corresponding non-linearity curves at Re~300 and Re~600 (L=12w, W_o=1.5w and W_c=50µm)..104

Figure 8-1 (a) The transfer curves for base geometry, 10×base geometry and 0.1×base geometry (L=15w, W_o=1.5w and W_c=100µm)................ 106

Figure 8-1 (b) The output characteristic curve and the load line for base geometry, 10×base geometry and 0.1×base geometry (L=15w, W_o=1.5w and W_c=100µm)...107

Figure 8-2 Temperature profile vs. depth of the device (L=18w, W_o=3w and W_c=80µm; Assumption: walls are adiabatic)............................ 110

Figure 8-3 Blocked-load output pressure recovery and no-load output velocity as a function of control pressure (L=15w, W_o=1.5w and Re=600)..... 112

Figure 8-4 (a) A comparison of the jet deflection of two designs on applying a pressure of 6KPa to the second control port (L=15w, W_o=1.5w, Re=600 and xy plane at z=25µm)...113

Figure 8-4 (b) A comparison of the pressure profile near bottom wall for the two designs on applying a pressure of 6KPa to the second control port (L=15w, W_o=1.5w, Re=600 and xy plane at z=25µm)...................114

Figure 8-5 Jet velocity profile for different control pressures (Re~600, W_o=1.5w, W_c=80µm) (x=550µm, z=25µm)..............................116

Figure 8-6 (a) Inset showing the angle of deflection (α) of the supply jet.......... 118

Figure 8-6 (b) Inset showing x=100µm and x=500µm...............................119

Figure 8-7 Switching time of a device with critical dimension of 50µm, Wc=80µm, L=15w and Re~600..120

Figure 8-8 Transit time of a device with critical dimension of 50µm and Re~600123

Figure 8-9 Required parameters to define the capacitance of the device........... 124

Figure 9-1 Microfluidic half-adder... 126

No **Description** **Pg**

Figure 9-2 (a) A=0, B=0, Carry=0, Sum=0 and (b) A=0, B=1, Carry=0, Sum=1.. 127

Figure 9-2 (c) A=1, B=0, Carry=0, Sum=1 and (d) A=1, B=1, Carry=1, Sum=0.. 128

Figure 9-3 Microfluidic clock... 129

Figure 9-4 Clock cycles of the ring-oscillator... 130

Figure 9-5 (a) Trigger=1, output =0 (b) Trigger=0, output=0 and (c) Trigger=0, output=1... 132

Figure 9-6 Microfluidic latch.. 133

Figure 9-7 (a) Set=1, Reset=0, Q_{i-1}=0/1, Q_i=1 and Q_i'=0, (b) Set=0, Reset=0, Q_{i-1}=1, Q_i=1 and Q_i'=0.. 135

Figure 9-7 (c) Set=0, Reset=1, Q_{i-1}=0/1, Q_i=0 and Q_i'=1 (d) Set=0, Reset=0, Q_{i-1}=0, Q_i=0 and Q_i'=1.. 136

Figure 11-1 Fabrication flow chart... 142

Figure 11-2 Possible experimental set-up.. 143

Figure 11-3 A schematic of static pressure measurement using pressure sensor.... 144

Figure 11-4 A schematic of mass flow measurement using hot-wire anemometer.. 144

Figure A-1 Supply velocity profile at constant supply pressure and constant supply velocity.. 149

LIST OF TABLES

No	Description	Pg
Table 3-1	Truth table of a NOR	20
Table 5-1	Truth table of a NOR	33
Table 5-2	Truth table of a half-adder	34
Table 5-3	Truth table of a latch	34
Table 7-1	A comparison of tan θ^* and tan θ for different lengths at Re=600	73
Table 8-1	Quantities P_{omax}, P_{cmax}, Q_{max} and supply velocity, V_s for the base geometry, 10×base geometry and 0.1×base geometry	105
Table 8-2	Scaling of common physical quantities with geometry at constant Reynolds number	106
Table 8-3	Summary of the supply velocity (V_s), supply pressure (P_s), switching time (τ) and power consumption vs. geometry at constant Reynolds number	111
Table 10-1	Summary of the upper and the lower bounds imposed on the choice of the critical dimension due to the available area, supply pressure, speed and bit transfer rate	140

CHAPTER 1 OVERVIEW

1.1 INTRODUCTION

Fluidic computing technology was explored 40 years ago for military applications, and it is now useful to revisit these ideas for biomedical technology, with the help of modern computational fluid dynamics and advanced device fabrication techniques.

The idea of microfluidic logic devices and circuits is to process useful information through a fluid medium by making use of simple mechanical elements or alternatively rely on fluid mechanic effects within the fluid itself, so that moving parts are eliminated. Our devices rely on fluid mechanic effects to accomplish digital logic. In this project a laminar microfluidic NOR, and more complex devices based on the NOR such as a clock and a static memory element are investigated and modeled. It is envisioned to make an integrated assembly of these microfluidic computing elements into a microfluidic computing system for lab-on-a-chip applications.

A computer is a universal information-processing machine. A computer is made from individual logic gates that perform elementary operations. The basic component of a digital logic gate is a controllable switch. A switch can be in the form of a relay, a vacuum tube or a transistor. The application of relay logic to large systems is limited because relay logic is slow as it involves mechanical actuation. Also, low failure rates of the components are essential for a system to work properly. But relay logic is not reliable as it involves moving parts and is thus associated with wear and tear. The transistor is a completely electronic device which replaced relay logic and vacuum tubes due to its small size, low power, high reliability and fast operation. The invention of the transistor and advances in microfabrication techniques resulted in the development of complex integrated circuits in the electrical domain.

It is useful and interesting to search for alternative devices which can serve as basic components for computing systems in different physical domains. For example there is a need to develop a microfluidic computer for lab-on-a-chip applications. The necessity to have a microfluidic computer for lab-on-a-chip systems served as a motivation for this project. Having said that, our microfluidic computing system is not envisioned to replace silicon technology in other applications because the microfluidic logic circuits would be several orders of magnitude slower than silicon chips amongst other reasons. The purpose of this project is to design microfluidic logic devices and circuits to develop a fluidic platform for lab-on-a-chip systems.

The increasing complexity of lab-on-a-chip systems will make it extremely difficult to send the information to external peripheral devices for processing. Thus it will become absolutely essential to have an on-chip microfluidic processor to enable on-chip decision making capability for lab-on-a-chip systems. Easier and cost-efficient integration is possible if information is processed in the microfluidic domain for lab-on-a-chip systems. This idea is depicted in Figure 1-1.

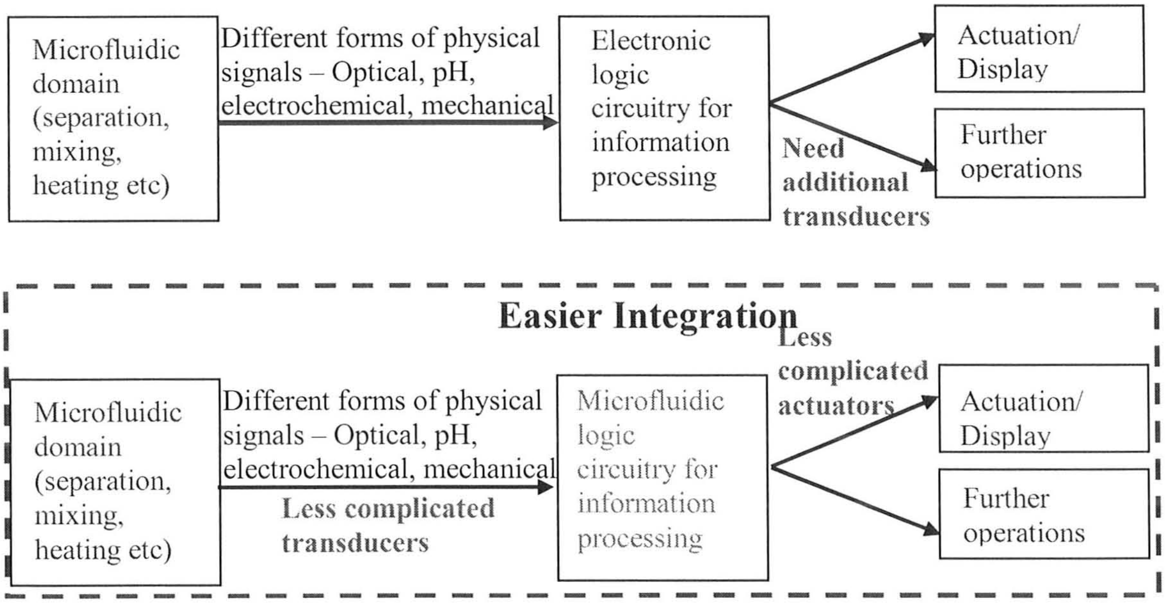

Figure 1-1: Advantages of information processing in the microfluidic domain over information processing in the electrical domain

For example a microfluidic clock can be used to drive a peristaltic pump without changing domains or requiring amplification. Microfabrication can increase the economic feasibility of integrated microfluidic circuits by lowering the cost per chip. Microfabrication enables in-situ interconnections between the devices, thereby reducing the interconnect delays and enabling faster communication among the various devices.

In the 1960s, various fluidic devices such as amplifiers, logic gates and oscillators were realized [1-8]. The basic operating principles of the fluidic devices reported in the literature are: momentum interaction devices, wall-attachment or coanda effect devices, turbulence amplifiers and vortex devices. But the critical dimension of these devices was in the range of 0.5mm-1mm. They were operated at very high Reynolds number. As a result, the switching speed was low and the power consumption was high.

Recently, there has been some interest in accomplishing *microfluidic* logic [10-15]. But the devices that have been realized to date either make use of special fluids such as viscoelastic fluids or use electrical signals to achieve microfluidic logic. The use of electrical signals to achieve microfluidic logic defeats the purpose of avoiding external peripheral devices for processing. Some of the designed logic gates were not concatenable due to the mismatch between input and output signals. None of them can be used to make a multipurpose microprocessor.

Faster switching speed and the need to form complex integrated microfluidic circuits to process information in the fluidic domain are the driving forces for smaller logic devices. Miniaturization also favors the low Reynolds number regime [16]. Most of the device principles that were used for fluidic devices do not scale usefully for microfluidic devices. This is because as the devices are made smaller the viscous forces reduce by the square of the dimensions but the inertial forces reduce by the cube of the dimensions.

Our devices are based on pressure-controlled jet deflection effects. The working fluid is water and the Reynolds number is ~600. It should be noted that though the modeled devices were simulated with the working fluid as water and Re~600 in general, the results apply to any fluids and the laminar jet flow regime (Re~300-600: Refer to Section 7.5).

Our designed NOR satisfies all the five requirements (Refer to Chapter 5) needed to make a computing system. The transfer curves are non-linear, fan-out is greater than 12, the input and output signals are in the same physical domain and the information flow is in the forward direction only. The NOR is a universal gate and thus all logic functions can be realized by a combination of NORs.

Three important components of computing: a half adder, a memory/latch and a clock were also simulated. A half-adder is an essential component of the Arithmetic Logic Unit (ALU) of a computer. A clock helps to synchronize the processes in a computing system. Information can be stored using memory elements.

Future work will concentrate on fabricating the simulated devices and testing them experimentally. This will be followed by understanding and demonstrating the various important interfaces that are required to integrate the microfluidic logic devices and circuits with other components for lab-on-a-chip applications, as depicted in Figure 1-1.

1.2 OUTLINE

The following chapters are organized into several main topics. Chapter 2 is an introduction to the operating principles of various fluidic devices realized in the late 1960s. Chapter 3 introduces a laminar NOR studied in 1967. Chapter 4 includes a discussion of the microfluidic devices that have been tested and/or simulated in recent years. Chapter 5 gives an introduction to Boolean logic and digital circuits. Chapter 6 introduces the ANSYS-CFX simulator to the reader. The results for our simulated devices along with a discussion of important observations and possible explanations for those observations are presented in chapter 7. Chapter 8 addresses the scaling issues and physical insights about the non-linearity of transfer curves and the switching time. Our simulated half-adder, clock and latch/memory element are presented in Chapter 9. Chapter 10 wraps up the work done in this thesis with some concluding remarks. Finally, Chapter 11 focuses on future work.

CHAPTER 2 FLUIDIC LOGIC

Greeks and Romans developed sophisticated water power systems. The purpose of these devices was to harness fluid power in an economical and efficient manner [1]. Fluid logic captured the imagination of the scientific and engineering community in the 1930s when Henri Coanda was studying the flow of free jets of fluids [2]. However, due to the lack of availability of modern simulation tools it was difficult to solve the Navier Stokes equation. Therefore, progress was relatively slow. It was only in late 1960s that various fluidic devices such as amplifiers, logic gates and oscillators were reported.

The fluidic devices reported in the literature were operated in the turbulent regime. The basic principles of operation of the reported devices are: momentum interaction devices, wall-attachment or coanda effect devices, turbulence amplifiers and vortex devices [1-7]. An intensive search of the literature revealed that only a single study was performed on the feasibility of a *laminar* pressure-controlled jet deflection NOR element which will be discussed in detail in Chapter 3.

A brief description of the above mentioned basic principles is as follows:

2.1 MOMENTUM INTERACTION DEVICES

When two jets interact with one another the forces exerted on the resulting jet depends on the momentum of both the jets. And in the case where no interactions with the surrounding boundaries are involved their vector sum determines the magnitude and direction of the resultant jet. When two jets interact with one another the magnitude and the direction of the resultant jet can be calculated from Newton's second law of motion over the control volume (as shown in Figure 2-1) as follows [1]:

$$F = \frac{dp}{dt} = \frac{d(mu)}{dt} = u\frac{dm}{dt} + m\frac{du}{dt} \tag{2-1}$$

where F: force

p: momentum

m: mass

u: average velocity

For a jet we can assume:

$$\frac{du}{dt} = 0 \tag{2-2}$$

Thus, if we consider a fluid jet of density ρ, cross-section area A and average velocity u, the mass rate of fluid flow from the jet is $A\rho u$ and the corresponding rate of change of momentum is given by $A\rho u^2$. Figure 2-1 shows 'supply' jet and 'control' jet of area A_{supply} and $A_{control}$, average velocity u_{supply} and $u_{control}$ respectively and density of ρ.

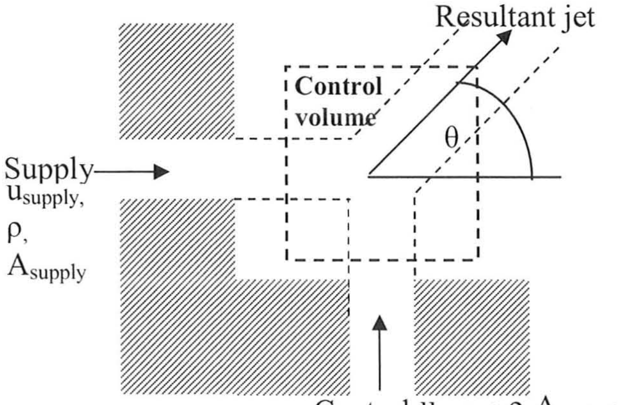

Figure 2-1: Momentum interaction of two jets

Hence the rate of change of momentum of nozzles 'supply' and 'control' can be calculated as:

$$\frac{dp_{supply}}{dt} = F_{supply} = \rho A_{supply} u_{supply}^2 \tag{2-3}$$

$$\frac{dp_{control}}{dt} = F_{control} = \rho A_{control} u_{control}^2 \tag{2-4}$$

Thus, from the vector addition, the magnitude and the direction of the resultant force is given by:

$$F_r = \sqrt{F_{supply}^2 + F_{control}^2} \tag{2-5}$$

And

$$\tan\theta = \frac{F_{control}}{F_{supply}} \tag{2-6a}$$

$$\tan\theta = \frac{A_{control} u_{control}^2}{A_{supply} u_{supply}^2} \tag{2-6b}$$

Both active and passive devices were realized using momentum interaction principle.

- Active momentum interaction devices: In active momentum interaction device, logical combinations are generated due to the interaction between the power jet and control signals. In order to realize a pure momentum interaction device (i.e. without any wall attachment effect), the walls in the interaction region are eliminated. For example in an EQUIVALENCE gate, an output signal is obtained when both or neither of the two control signals are applied. When either control signal is applied, the momentum interaction between the supply jet and control signal forces the supply jet into one of the vents. The logical expression of an equivalence gate is (A·B+A’·B’) where the notations "·" and "’" will be introduced in Chapter 5. The device schematic is shown in Figure 2-2 [1].

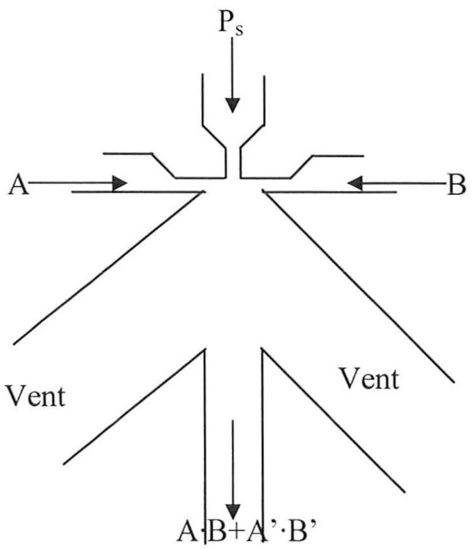

Figure 2-2: Momentum interaction EQUIVALENCE gate

- Passive momentum interaction devices: A logical combination is obtained due to the interaction between control signals. For example in an AND gate, when either or both of the control signals are low, the output is low. But when both the control signals are high the momentum interaction of control jets forces the resultant jet into the output receiver [3]. The logical expression of an AND gate is A·B and the device schematic is shown in Figure 2-3.

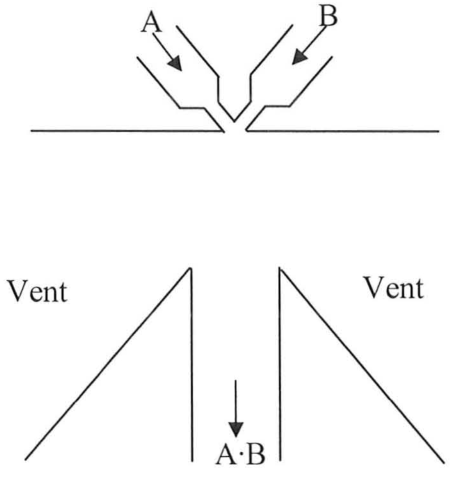

Figure 2-3: Momentum interaction AND gate

2.2 WALL-ATTACHMENT OR COANDA EFFECT DEVICES

As a laminar jet emerges from a supply nozzle the high velocity fluid molecules of the jet interact with lower velocity ambient molecules. The viscous shearing forces result in the entrainment of the ambient molecules. This interaction causes the jet to spread laterally [1] as shown in Figure 2-4. The momentum of the jet is shared with an increasing number of molecules from the ambient regions on either side of the jet.

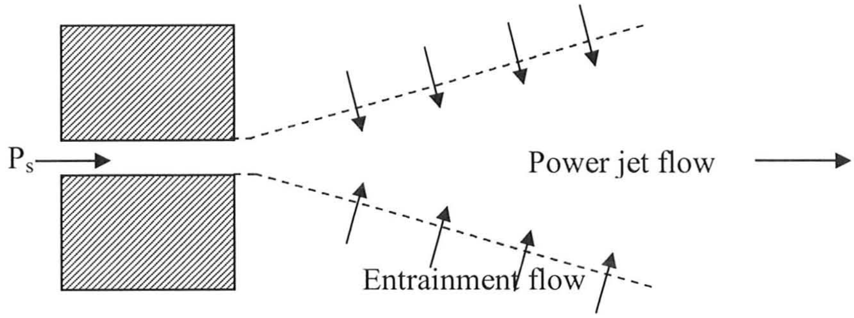

Figure 2-4: A laminar jet entraining fluid particles on all sides

Thus the velocity of the jet decreases as it moves downstream. This process is called jet entrainment. Depending upon a number of design features (for example the distance of the side walls) and operating conditions (for example supply pressure should be in the designated range), the jet may do one of the following [1]:

1. Spread and attach to both side walls.
2. Deflect from the centerline and attach to one or other of the walls.
3. Flow out of the device without coming into contact with either side.

If the position of the side wall is such that the counter flow required to replace molecules entrained by the jet is insufficient on one side of the jet, the fluid will be removed faster than what it can be replaced. At constant temperature, pressure depends on the number of molecules in a given volume. The pressure on the side of the wall will reduce due to a decrease in the number of molecules. The pressure on the other side of the jet, where the counter flow is sufficient to offset the entrainment, will not change. A transverse pressure gradient is thus established which results in the jet deflecting towards the lower pressure region i.e. towards the wall. The deflection of the jet towards the wall will self-reinforce the process of deflection; thereby ultimately resulting in the attachment of the jet to the wall as shown in Figure 2-5. This point is called the jet attachment point.

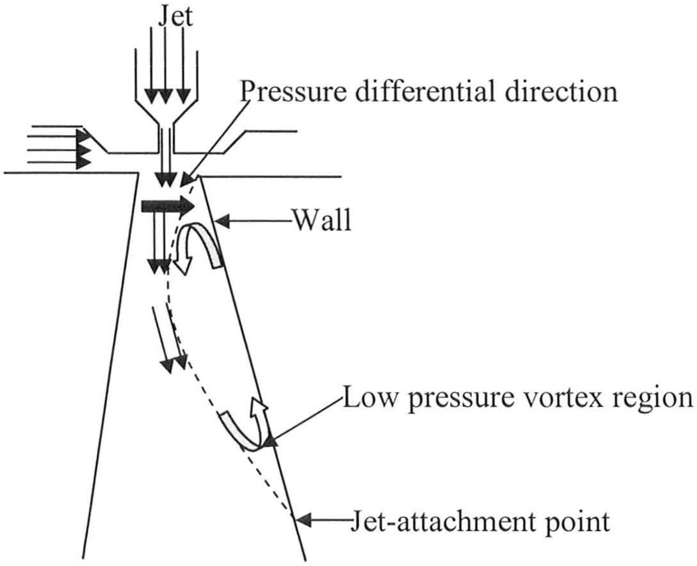

Figure 2-5: Jet deflecting from the centerline and attaching to one of the walls due to wall-attachment or Coanda effect

Vortices are usually observed in the low pressure region as shown in Figure 2-5. The existence of the pressure differential between the outer edge of the jet and the low pressure region next to the wall maintains the jet attachment. If there are no changes, this equilibrium condition will allow the jet to flow along the wall continually. In order to change this condition it is necessary to increase the pressure within the low pressure region (i.e. in the region close to the wall) until it exceeds the pressure on the outer edge of the power jet. This is accomplished by injecting additional fluid through the control port and into the low pressure region. If the rate of fluid injected into the low pressure region exceeds the rate at which fluid is removed by entrainment, the pressure on the inner edge of the jet will increase. If this pressure becomes greater than the pressure of the outer edge, the pressure differential is reversed and the jet will be forced to detach, cross to the other side, and attach to the other wall.

The various design considerations that were studied in late 1960s, for the wall attachment effect were the effect of wall length (L), wall angle (α), setback (D), effect of vents and the effect of splitter shape and position [1,2, 4]. These geometric parameters are shown in Figure 2-6.

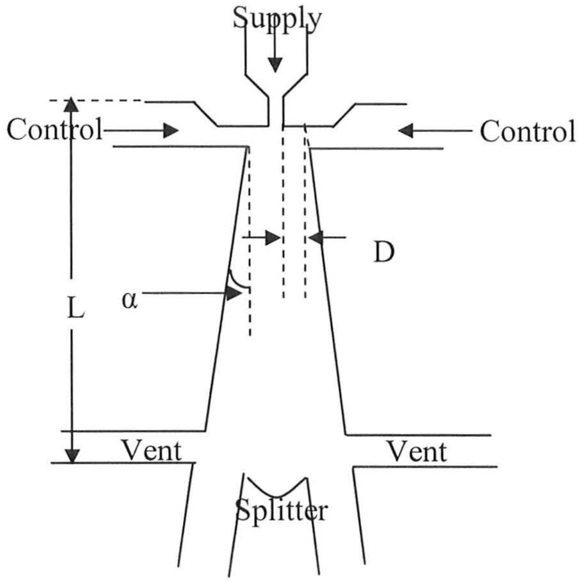

Figure 2-6: Geometric parameters studied in late 1960s for wall-attachment effect

2.3 TURBULENCE AMPLIFIERS

The difference in pressure recoveries for a laminar and turbulent jet was used to achieve NOR operation. If a laminar jet is close to the normal transition regime, any small external disturbances will cause the jet to break up into turbulence. Thus the pressure recovery at the receiver will be reduced [1, 5, 6]. Figure 2-7 (a) and (b) shows the ON and OFF states of a turbulence NOR respectively.

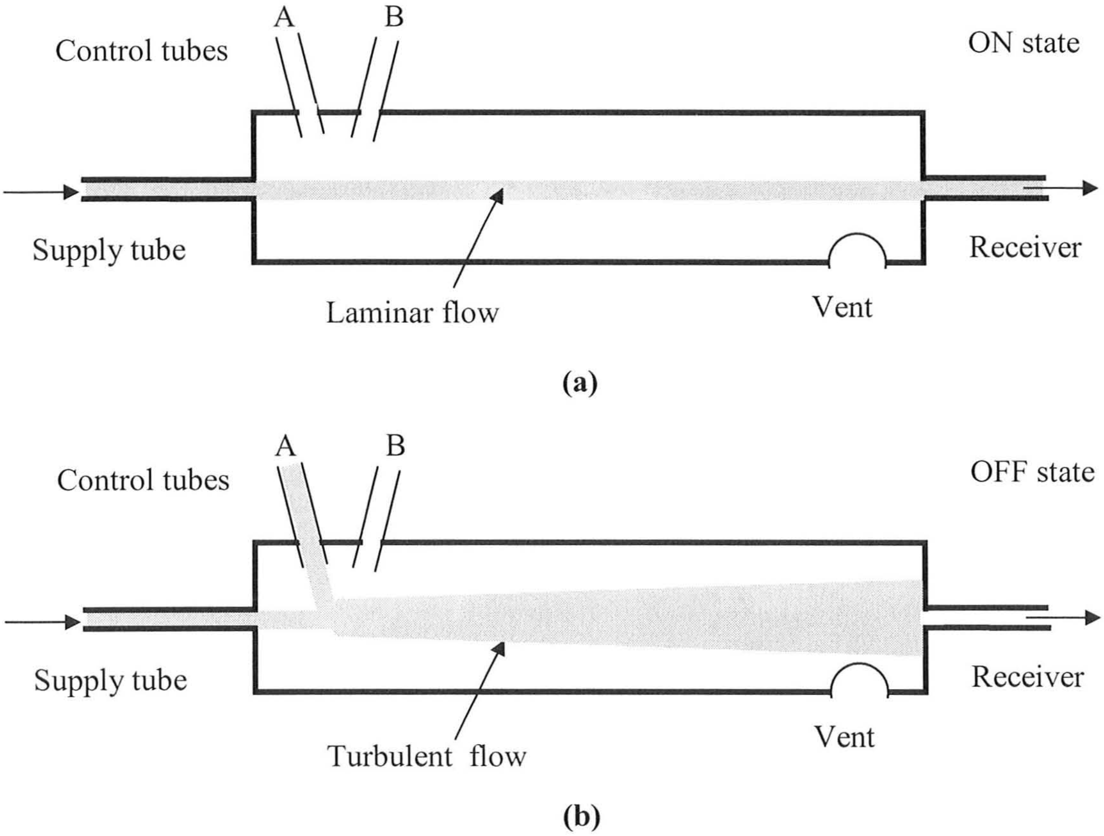

Figure 2-7: Turbulence NOR (a) ON state (b) OFF state

In the ON state, the jet from the supply nozzle enters a large chamber and is collected at the receiver some distance away at the other end of the chamber. In the OFF state, the flow in either or both of the control ports act as a source of disturbance; thereby making the jet turbulent. Therefore the pressure recovery is reduced at the receiver.

A further theoretical point to note is that the jet spreads as $\frac{2}{3}$ power of the distance from the nozzle and the centerline velocity decreases as $\frac{1}{3}$ power of the distance, so the local values of Reynolds number is proportional to the $\frac{1}{3}$ power of the distance [2]. The onset of instability depends on the local values of Reynolds number. In other words the jet is stable initially at smaller lengths near the nozzle exit and become unstable at a point well downstream from the nozzle exit. Thus the length of the chamber is an important design consideration for the efficient working of a turbulence amplifier. The maximum length of the chamber is determined by the condition that the jet should not become turbulent as it moves downstream in the ON state of the device. The minimum length of the chamber on the other hand, is determined by the condition that the jet should become turbulent even with the small disturbances in the OFF state of the device.

2.4 VORTEX DEVICES

Vortex devices were mainly used as diodes. A simple diode realized using this principle is shown in Figure 2-8 [2, 7].

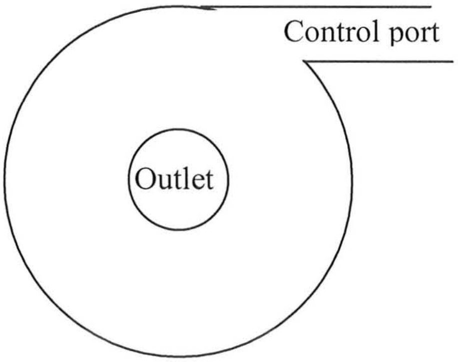

Figure 2-8: A vortex diode

The control flow that enters the diode tangentially undergoes a spiral motion as shown in Figure 2-9, and leaves through an axial outlet. Huge pressure drops are observed due to spiral motion. This direction of flow is defined as the backward flow. However, the flow entering through the outlet and leaving from the control port (i.e. forward direction) would not undergo a spiral motion. Hence low pressure drop is observed. "Diodicity" is defined as the ratio of pressure drop in the backward direction to the pressure drop in the forward direction.

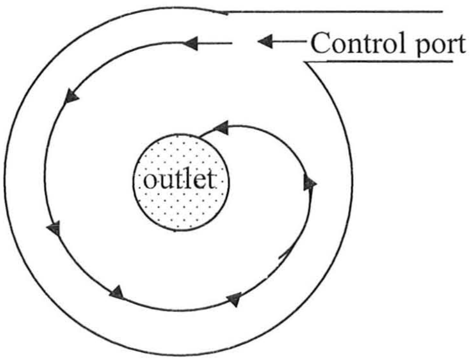

Figure 2-9: Swirl motion of a vortex diode in the backward flow direction

CHAPTER 3 LAMINAR NOR (WALKER AND TRASK, 1967)

Most of the fluidic devices reported in late 1960s and early 1970s were operated in the turbulent regime (Refer to Chapter 2). The power consumption was high due to the turbulent regime of operation. But there was a need to design digital elements that could operate at lower power. Thus the feasibility of a laminar NOR unit was studied analytically and experimentally by Walker and Trask [8]. This work is not well-known, having been published in a book and receiving no citations over the last 39 years. The work done by Walker and Trask [8] was published in late 1960s – years in which the electronics industry was picking up momentum. The fluidic computing lost out in the competition with the electronics computing industry due to its slow speed of operation. Therefore the work done by Walker and Trask [8] did not receive any citations except in a book; and was lost with the passage of time. Perhaps finding the work done by Walker and Trask [8] (which was lost due to the lack of citations) is a discovery in itself!

The NOR designed by Walker and Trask [8] is shown in Figure 3-1.

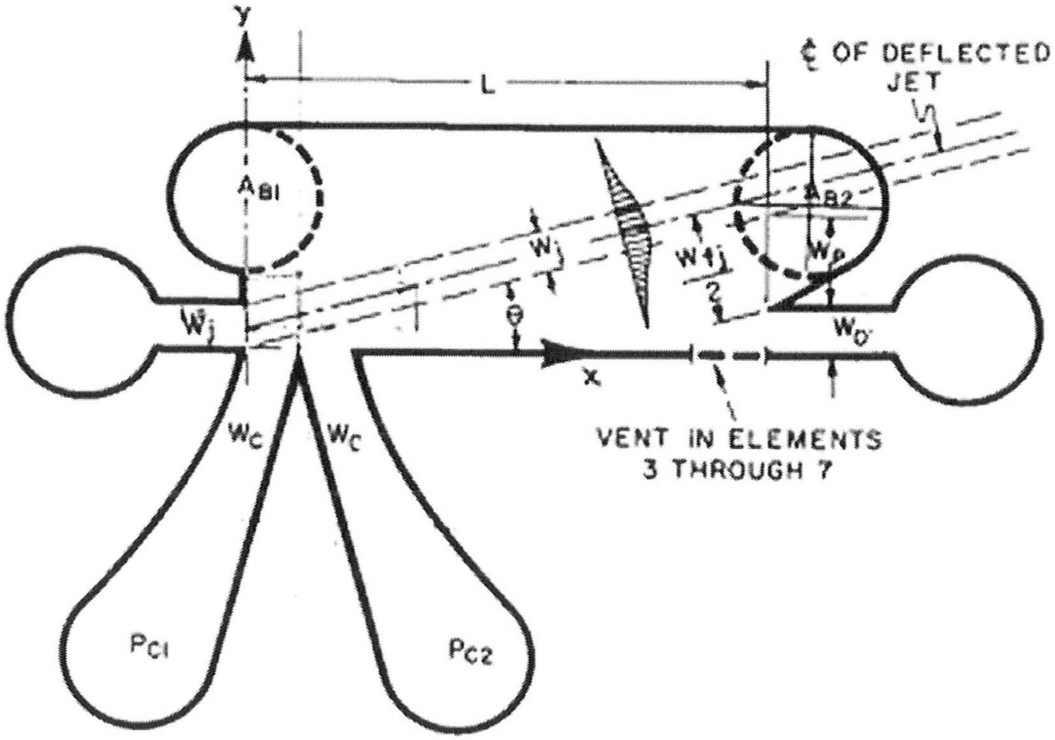

Figure 3-1: Basic NOR geometry considered in an investigation in 1967 [8]

The critical dimension of the device was 0.5 mm, height = 0.413 mm and the length~7.5mm. The working fluid was air. The input pressure was less than 10 cm of H_2O which is equivalent to ≈ 1KPa.

In Section 2.1 while discussing the momentum-interaction effect devices, we assumed that there is a considerable set-back between the control nozzles and the supply nozzle. If however, the set-back between the control nozzles and the supply nozzle is not considerable then the flow issuing from the control nozzle and the supply jet begin to interact with each other. This results in a considerable pressure build-up in the interaction region. Thus Newton's Second law of motion is applied over the control volume (shown in Figure 3-2) to calculate the angle of deflection as follows [3]:

Consider a supply jet and flow through the control ports of area A_{supply} and $A_{control}$, average pressure of P_{supply} and $P_{control}$ and average velocity of u_{supply} and $u_{control}$ respectively as shown in Figure 3-2.

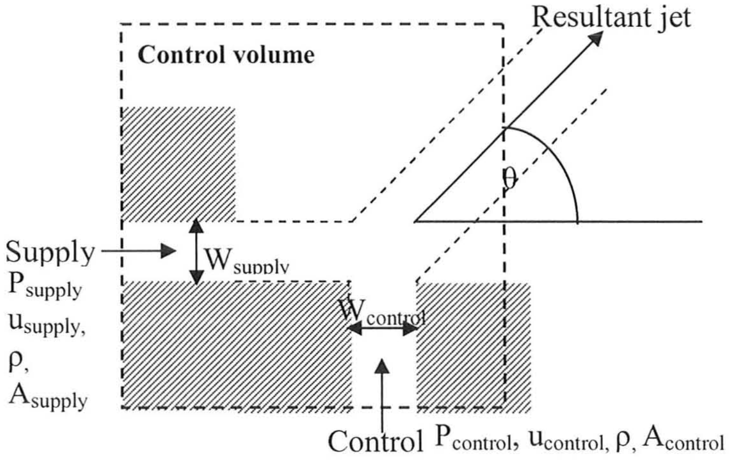

Figure 3-2: Momentum and pressure interaction of a jet and flow

Applying Newton's second law of motion over the control volume shown in Figure 3-2 the angle of deflection is given as [1]:

$$\tan\theta = \frac{(P_{control} + \rho u_{control}^2)A_{control}}{(P_{supply} + \rho u_{supply}^2)A_{supply}} \tag{3-1}$$

Also,

$$A_{control} = W_{control} \times h_{control} \tag{3-2}$$

where $W_{control}$: Control port width

$h_{control}$: Control port height

And

$$A_{supply} = W_{supply} \times h_{supply} \tag{3-3}$$

where W_{supply}: Supply port width

h_{supply}: Supply port height

For a device of uniform height:

$$h_{\mathrm{supply}} = h_{\mathrm{control}} \tag{3-4}$$

Substituting Equation 3-2, Equation 3-3 and Equation 3-4 into Equation 3-1, we obtained:

$$\tan\theta = \frac{(P_{\mathrm{control}} + \rho u_{\mathrm{control}}^{2})W_{\mathrm{control}}}{(P_{\mathrm{supply}} + \rho u_{\mathrm{supply}}^{2})W_{\mathrm{supply}}} \tag{3-5}$$

In Equation 3-5 we assumed the absence of a wall in the vicinity of the interaction region. Additional forces however, have to be included if a wall is present in the vicinity of the interaction region. Thus to include the effect of a slant wall in the device reported by Walker and Trask [8], Equation 3-5 is modified as follows:

$$\tan\theta = \frac{(P_{\mathrm{control}} + \rho u_{\mathrm{control}}^{2})W_{\mathrm{control}} + F_{\mathrm{wall}}/h}{(P_{\mathrm{supply}} + \rho u_{\mathrm{supply}}^{2})W_{\mathrm{supply}}} \tag{3-6}$$

where F_{wall}: force due to the presence of a slant wall

For W_{control} comparable to W_{supply} and for small set-back between the supply nozzle and control nozzles:

$$\rho u_{\mathrm{control}}^{2} << P_{\mathrm{control}} \tag{3-7}$$

Thus Equation 3-6 can be simplified as:

$$\tan\theta = \frac{P_{\mathrm{control}} W_{\mathrm{control}} + F_{\mathrm{wall}}/h}{(P_{\mathrm{supply}} + \rho u_{\mathrm{supply}}^{2})W_{\mathrm{supply}}} \tag{3-8}$$

Since the set-back between the supply nozzle and control nozzles is low in the device reported by Walker and Trask [8], the deflection in the devices is accomplished mainly due to the control pressure. In other words the basic principle of the device reported by Walker and Trask [8] is pressure-controlled jet deflection.

We would also like to mention that for Walker and Trask's [8] device the supply jet flow into a relatively large chamber with a uniform pressure distribution of 0KPa; therefore the supply jet pressure rapidly equalizes with the chamber pressure and the supply jet behavior is determined solely by its momentum. Thus for the device reported by Walker and Trask [8], Equation 3-8 can be simplified as:

$$\tan\theta = \frac{P_{\text{control}} W_{\text{control}} + F_{\text{wall}} / h}{\rho u_{\text{supply}}^{2} W_{\text{supply}}} \tag{3-9}$$

The small set-back between the control ports and the supply nozzle provides an additional advantage. The supply jet blocks the control ports effectively which increases the impedance of the control ports. The increased control port impedance helps to increase the fan-out. Walker and Trask [8] reported a maximum experimental fan-out of 3. The power consumption of the device was reported as 2mW. The power consumption of the device was approximately 2% of the state-of-the-art wall attachment devices at that time.

We have simulated the four possible states of a NOR device using our improved design. The simulated results of the four possible states of NOR are included here to help the reader understand the operation of the device reported in the literature. The truth table of a NOR gate is shown in Table 3-1.

A	B	NOR
0	0	1
0	1	0
1	0	0
1	1	0

Table 3-1: Truth table of a NOR

When the pressure in both the input ports is low the supply jet flows straight from the supply to the outlet and the device is considered as ON. When the pressure in either or both of the input ports is high the supply jet is deflected into the circular vent and the device is considered as OFF. The four states of a NOR are shown in Figure 3-3 (a), (b), (c) and (d).

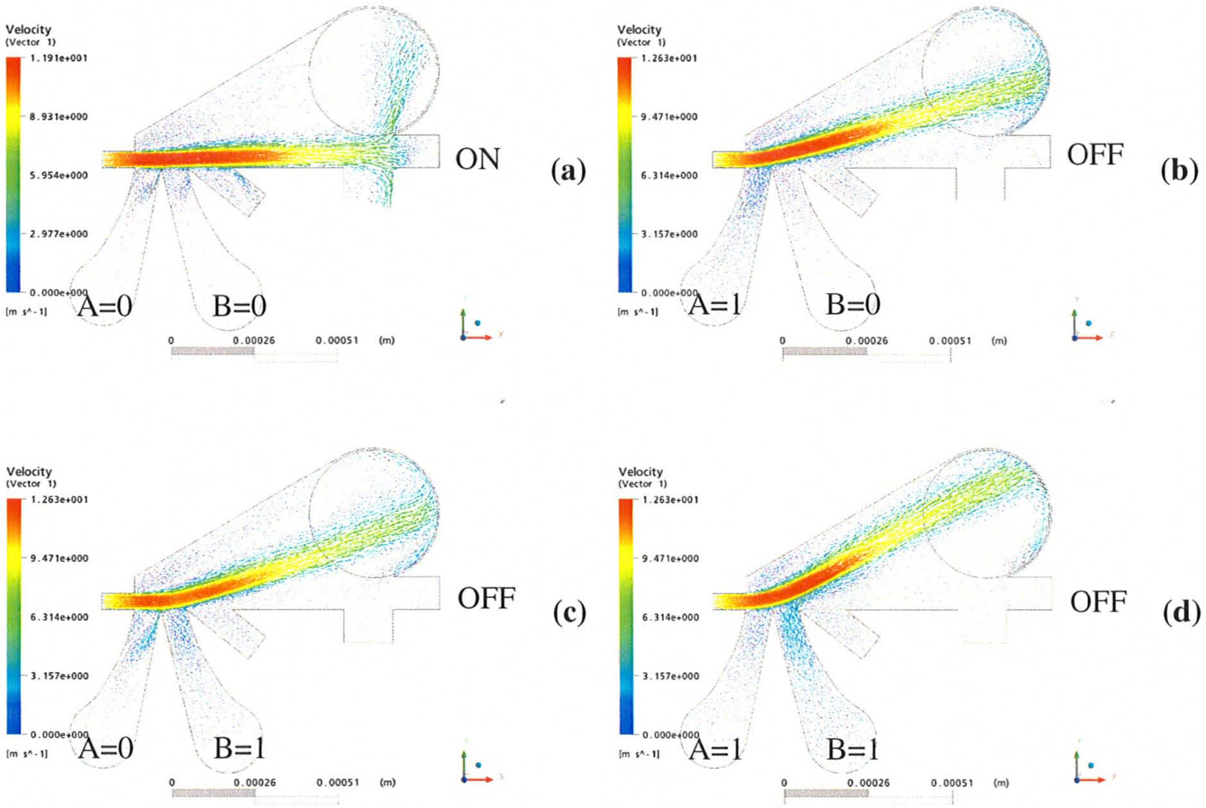

Figure 3-3 (a) A=0, B=0, ON-state, (b) A=1, B=0, OFF-state, (c) A=0, B=1, OFF-state and (d) A=1, B=1, OFF-state

In the device reported by Walker and Trask [8] the supply jet flows straight into the outlet. Not many physical insights were provided as to why such a design was chosen. The authors introduced a vent close to the outlet in their experimental models to increase the output pressure recovery, but the vent was not included in their theoretical models. No explanation was provided to explain why a vent close to the outlet helps to increase the output pressure recovery.

Walker and Trask [8] acknowledged that: "One unfortunate aspect of the basic geometry is the control mismatching. The second control, located closer to the receiver, causes a reduction in the maximum fan-out by a factor ranging from 10 to 30 per cent." We have modeled a geometrically scaled (Refer to Section 8.1 for geometry scaling) and Reynolds number scaled (Refer to Section 7.5 for Reynolds number scaling) version of their device using ANSYS – a modern computation fluid dynamics software package. The transfer curve, the output curve and the load lines (Refer to Chapter 7 for the symbols and the analysis of the obtained data) for the first control port and second control port are shown in Figure 3-4 (a) and (b).

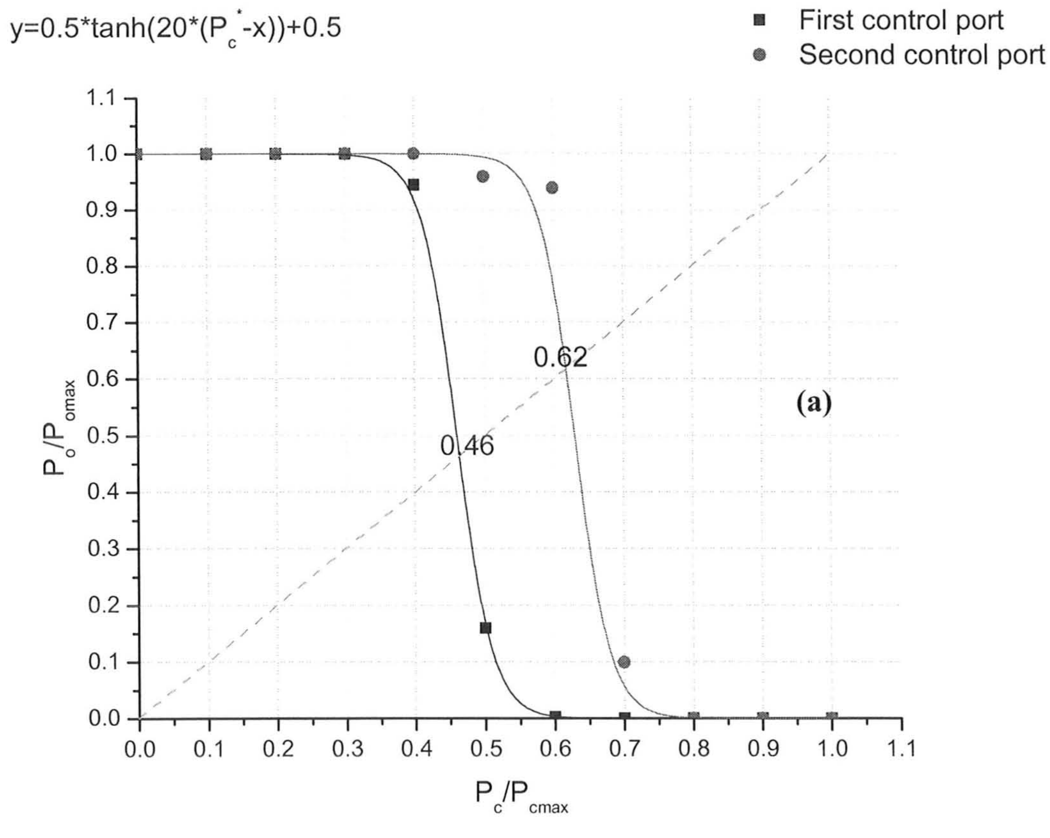

Figure 3-4 (a): Transfer curves for first control port and second control port ($W=50\mu m$, length=15W, $W_o=1.5W$ and Re~600)

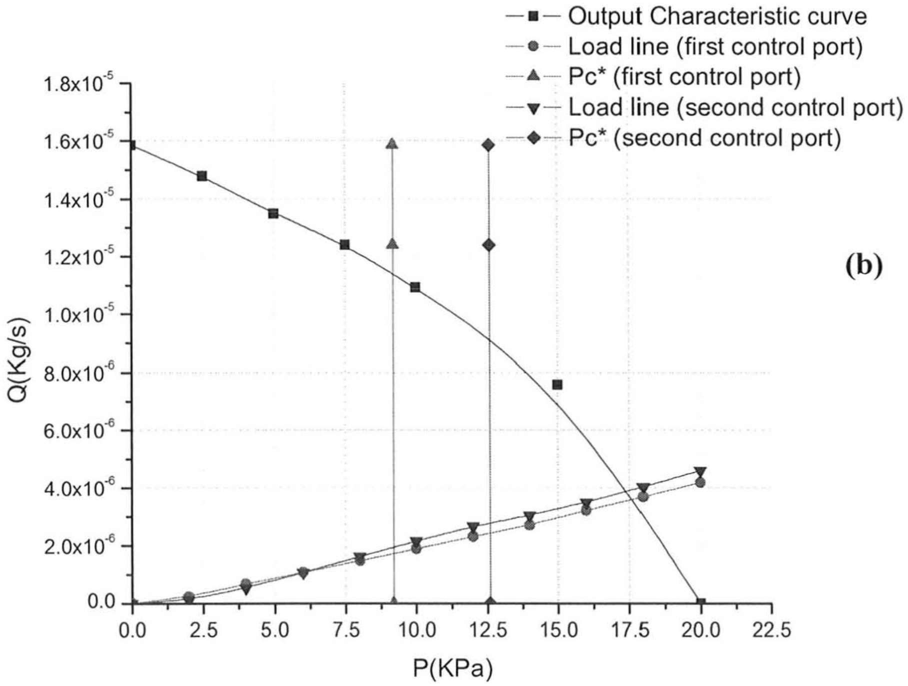

Figure 3-4 (b): Output characteristic curve, load line and the minimum pressure required to switch the device from ON to OFF for first control port and second control port (W=50µm, length=15W, W$_o$=1.5W and Re~600)

Our modeling showed that "control mismatching" not only leads to a reduction in the fan-out for the second control port, but it also leads to a mismatch in the minimum pressure required to switch the device from ON to OFF and vice-versa. A deeper analysis of the structure showed that the supply jet is deflected by a greater amount if let us say a pressure of 10KPa (P_c/P_{cmax}=0.5) is applied to the first control port than if the same pressure is applied to the second control port. This is shown in Figure 3-5 (a) and (b).

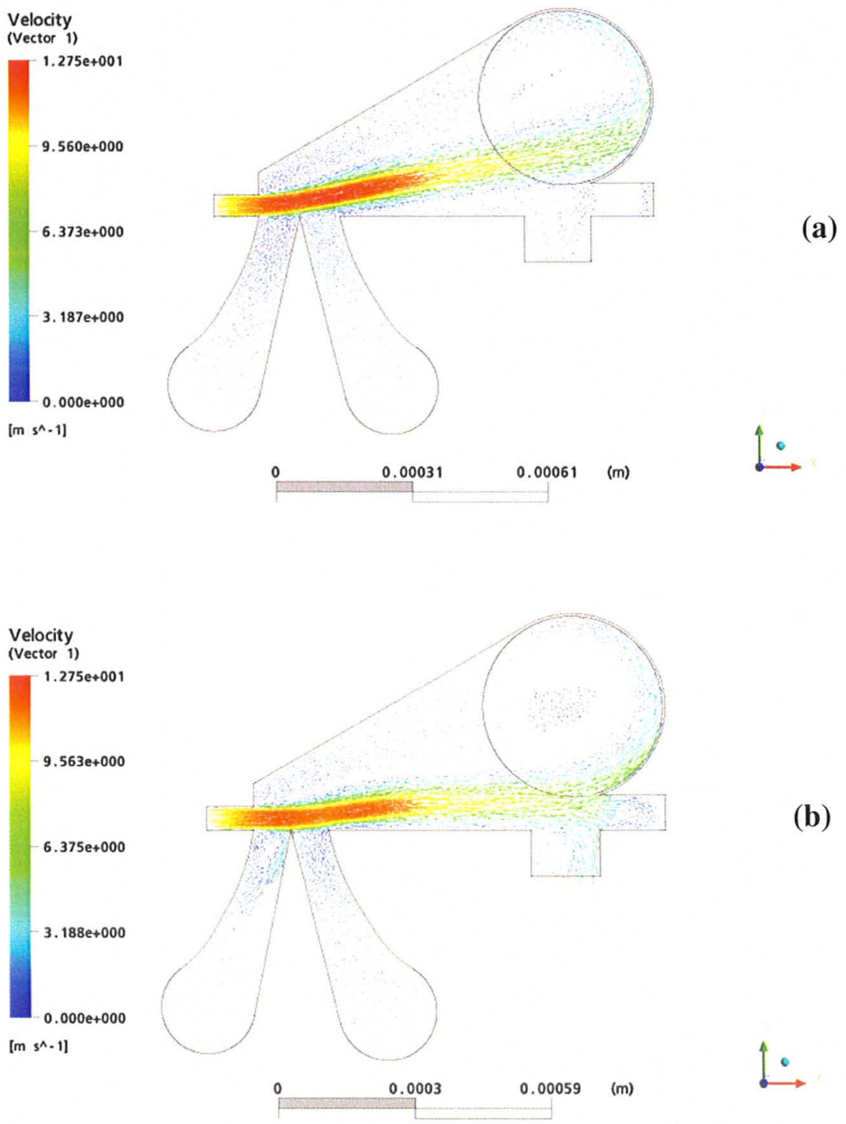

Figure 3-5: Velocity profile when 10KPa is applied to (a) first control port and (b)second control port (height=50μm and xy plane at z=25μm)

The difference in the amount of jet deflection with respect to the first and second control port on applying the same control pressure, is reflected in the transfer curve as a mismatch in the minimum pressure required to switch the device from ON to OFF. We would like to use an analogy with electronic circuits to explain why the variation in the pressure required to change the state of the device from ON to OFF is undesirable. The variation in minimum pressure required to switch the device from ON to OFF is equivalent to the variation in the threshold voltage of the components in digital integrated electronic circuits. The variation in threshold voltage is highly undesirable in electronic circuits. This is because at an applied voltage, devices with a lower threshold voltage will be turned ON while the devices with a higher threshold voltage will continue to be in their OFF state. This can result in improper functioning of the circuits. The variation in the threshold voltage can even result in instability of SRAMs [27]. If a system has to perform within acceptable standards, higher non-linearity is required to demagnify the variations in the threshold voltage of the devices. Since non-linearity of the transfer curves of the driving device decreases with an increase in the number of driven elements (Refer to Section 7.3), the higher non-linearity requirement limits the number of gates that a device can drive satisfactorily. Thus the variations in threshold voltage are highly undesirable for building reliable systems. Extending the analogy to microfluidic computing systems, a significant mismatch in the pressure required to change the state of the device will result in unreliable and unpredictable system performance.

No efforts were spent by Walker and Trask [8] to understand the device performance in the context of the five basic requirements needed to make a computing system. Walker and Trask [8] achieved an excellent structural design of the NOR element. But neither the physical basis of non-linearity nor its importance in the transfer curves was understood. The criterion used to define the ON and OFF states of the device was weak. And there was a flow of information in the backward direction. To execute a correct truth table the information should flow only in the forward direction. The input and output should be isolated.

We also found some mistakes in their theoretical models. The impedance of the control ports was calculated incorrectly. The flow rate through the control ports was related with the control pressure as follows:

$$Q_c = C_c \tau \sqrt{\frac{2P_c}{\rho}} \tag{3-10}$$

But from our simulations we found that the relationship between the flow through the control ports and the control pressure is not trivial and depends on the supply jet velocity (shown in Figure 7-27). This mistake was carried forward in all the calculations which we believe resulted in incorrect theoretical fan-out values.

There were several omissions in the paper by Walker and Trask [8]. For example their NOR design was not fully optimized. The outlet width appeared to be one of the variables that were varied for maximum fan-out. But it was not clear why the higher outlet widths were not tried. It appeared that a systematic design of experiments was not formulated. Consequently the best combination of parameters was missed. The time dynamics of the device was not studied. Stable static performance of the device does not guarantee a stable dynamic behavior. Some of the important questions associated with Reynolds number scaling, geometry scaling, power vs. geometry and time vs. geometry were missing. Only a half-adder was tested experimentally by cascading several NORs.

To summarize, Walker and Trask [8] achieved an excellent overall structural design of the NOR element. They also achieved high control port impedance by using a straight bottom wall. But there were several deficiencies, weaknesses and omissions in the study. The work done in my Master's project is built heavily on the work done in 1967 by Walker and Trask [8]. In Chapter 7 the mistakes made in the paper by Walker and Trask [8] are corrected. In this thesis, the design is validated and the results are optimized using CFD. The omissions are addressed in Chapter 8. Greater insights into the physical principles of the device are also provided in Chapter 8. New devices are presented in Chapter 9.

CHAPTER 4 MICROFLUIDIC LOGIC

All the fluidic devices mentioned in Chapter 2 were huge and were operated in the turbulent regime. As a result the switching speed was low and the power consumption was high. Devices in the laminar regime consume lower power for the same dimensions. Faster switching speed and the need to form complex integrated microfluidic circuits to process information in the fluid domain, are the driving forces for smaller logic devices. Low power consumption and rapid switching time are highly desirable features in logic circuits composed of large numbers of fluid elements. In the following sub-sections we will present some of the work done in recent years.

4.1 Logic using special fluids:

Microfluidic diodes, OR and NAND based on conductive solutions were reported [9]. A schematic of the diode is shown in Figure 4-1. When a forward bias voltage of 1.5 was applied between electrodes 1 and 2, a current of 100nA was observed. If however, a reverse biased voltage is applied between 1 and 2, a current<2nA was observed. Thus significant current only flows in the forward-bias.

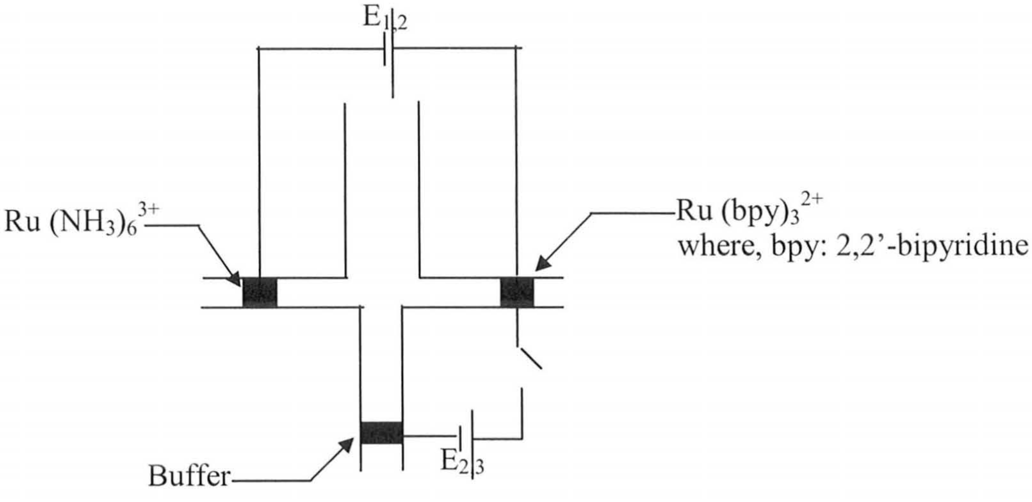

Figure 4-1: Microfluidic electrochemical diode

The above device requires special fluids for its operation. It is preferable to design microfluidic logic devices which use commonly available fluids such as water.

4.2 Logic using non-linearities in the system functional response:

Non-linearities in the system functional response instead of its fluid properties were used to demonstrate microfluidic OR, AND, XOR, NAND, NOR and NOT [10]. For very low Reynolds number, the pressure drop in channels is linearly related to the flow i.e $\Delta P=Q\times R$ where ΔP is the pressure drop, Q is the flow rate and R is the flow resistance. The pressure drop across the channels was maintained constant using capillary generated flows. The resistance of the channel was then varied by adjusting the length and area of cross-section to direct the overall system flow rate into desired channels. The gates were mechanically actuated, and the output signal is the color of the fluid. The major drawback of such an approach is: Switching inputs from one state to another requires the manual pinching of the channel whereas the output signal is the fluid of different colors. In other words, the output signal and input signals are in different physical domains. Therefore the output of one gate cannot be directly used to actuate the next gate.

4.3 Turbulent regime flip-flop and AND gate:

Pye et. al. has reported on the use of the wall attachment principle to realize a bistable flip-flop [11] as shown in Figure 4-2. Due to the fairly high Reynolds number used for device operation small turbulence was observed between the flow and the wall surface. This turbulence resulted in the formation of a low pressure vortex region near the wall; thereby accomplishing the jet attachment to the wall. The same group of authors has also reported on jet interaction effects to realize an AND gate [12] as shown in Figure 4-3. The width of the nozzle and the height of the device were reported to be the two most critical parameters affecting the performance of the device. The nozzle width was fixed to 30μm for both the wall attachment and jet interaction devices. The device heights of 250μm and 500μm were considered. CFD simulations were performed to investigate the device performance in terms of required operating pressure, switching times between the operational states and minimum device height. The bistable flip-flop and the AND gate designed by the authors are shown in Figure 4-2 and Figure 4-3 respectively.

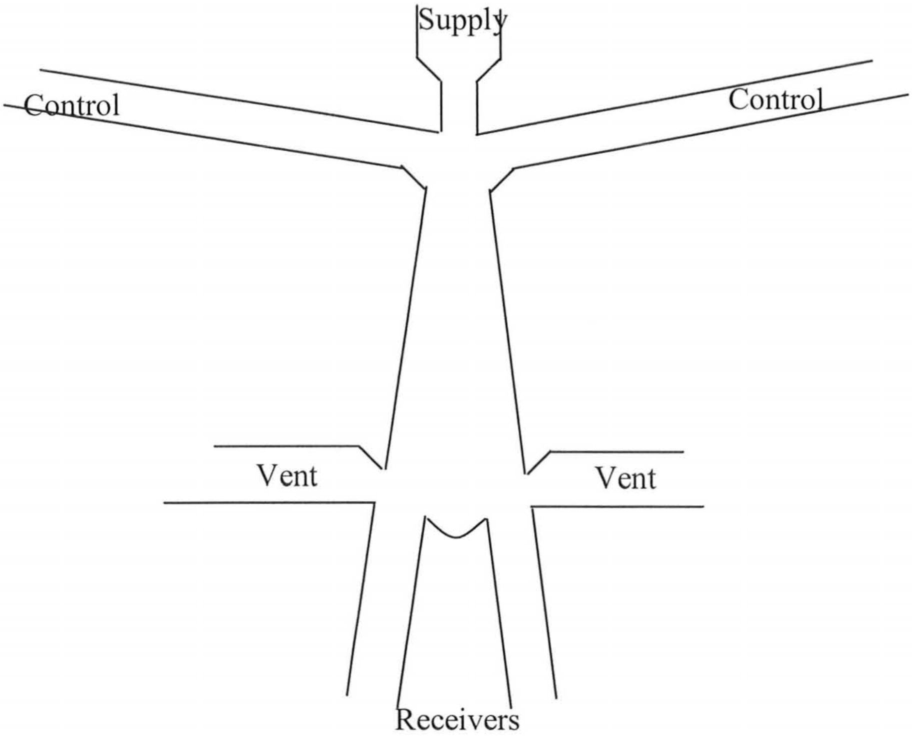

Figure 4-2: Bistable flip-flop

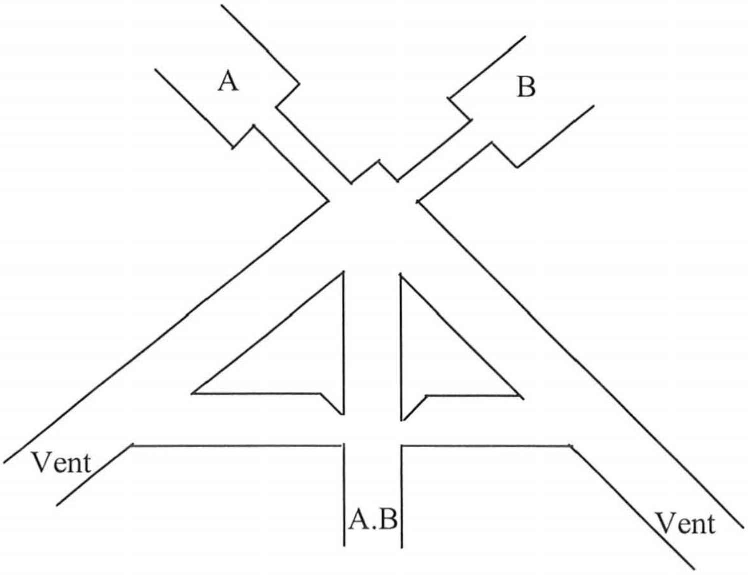

Figure 4-3: AND gate

The minimum operating pressure of the wall attachment flip-flop was found to be ~15KPa.

For the jet interaction AND gate, the authors reported that the supply pressure reduced the strength of the supply jet and thus the jet tends to disperse as it enters the interaction region. Thus an operating pressure of 30KPa was required. At an operating pressure of 30KPa, the switching time to change the states from 11 to 10 or from 10 to 11 was reported to be 1ms. The major disadvantage of the above realized AND gate was low power amplification. Due to low power amplification the fan-out was limited to 1. Thus amplifiers have to be added at every stage to make a logic circuit. This would not only add the complexity but would also result in high power consumption. Also, an AND is not sufficient for a computing system.

4.4 A microfluidic amplifier:

A silicon-micromachined fluidic amplifier device was simulated and tested experimentally [13, 14]. If the same pressures are applied at the control ports, the supply jet splits equally in each output port. But if any one of the control ports is at a higher pressure than the other control port, the supply jet will be deflected towards the lower pressure control port. This result in a pressure differential between the output ports. If the geometry is designed properly, the output pressure differential is higher than the control pressure differential. The authors of this paper achieved a power amplification of ~3.15 experimentally and 3.0 numerically at a 100KPa supply pressure for an amplifier with a 30μm channel width and a 40μm channel depth. A deep silicon RIE process using Cl_2 and BCl_3 was used for the vertical etching of the amplifier design. A schematic of the designed amplifier is shown in Figure 4-4.

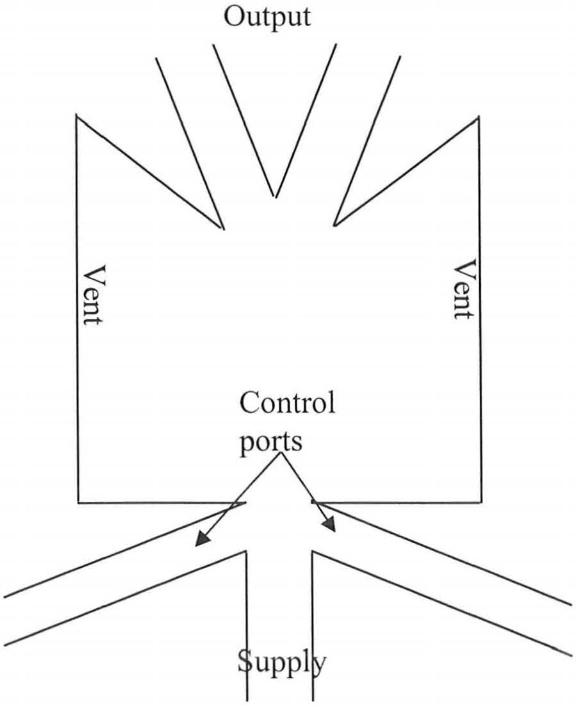

Figure 4-4: Schematic of microfluidic amplifier

4.5 A microfluidic oscillator:

A group of authors have analyzed a microfluidic oscillator operating with liquids (water, alcohol, and acetone) or gases (nitrogen, argon, and carbon dioxide), using numerical simulations [14]. A schematic of the designed microfluidic oscillator is shown in Figure 4-5. They used coanda effect to achieve the desired operations. A turbulent supply jet was allowed to interact with the flows in the control ports to accomplish wall-attachment or coanda effect. The output was fedback to the control ports to accomplish oscillations. The authors used two-dimensional analysis because of the high aspect ratio of the device. Their basic oscillator was 5775μm long and 3175μm wide, and has a control nozzle width of characteristic dimension of 50μm. The length of the feedback channels and the width were 2515μm and 150μm respectively. The maximum frequency achieved with gases was ~60KHz and with liquids was ~0.32KHz.

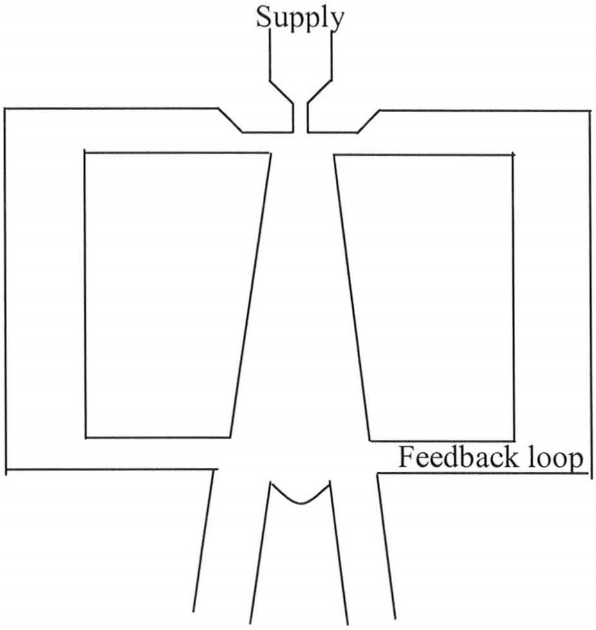

Figure 4-5: Schematic of microfluidic oscillator

To summarize, the use of special fluids such as electrochemical fluids limits the applicability of microfluidic logic. The incompatibility of the input and output signals [10] implies that the output of a gate cannot serve as an input for the next stage gate. In other words, the gates cannot be cascaded to make a system. An AND gate, an amplifier or an oscillator are not generic gates i.e. all logic functions cannot be expressed as a combination of these gates. Therefore, the development of these gates is an accomplishment at a device level but are not sufficient to make a microfluidic computing system.

CHAPTER 5 INTRODUCTION TO BOOLEAN LOGIC AND DIGITAL CIRCUITS

In an electronic digital circuit the design abstraction levels are: device (transistor), circuit, gate, module and system.

A logic gate is defined as an electronic circuit in which the logic level of the output signal is a function of the logic state of one or several input signals [17]. The input and output signals of a logic gate can take only two values: ON (high, 1) or OFF (low, 0). A general block diagram of a logic gate circuit is shown in Figure 5-1.

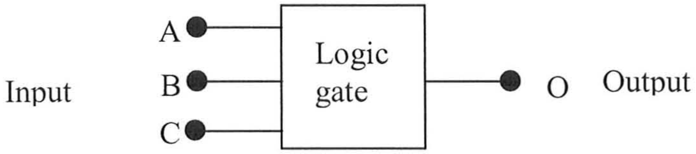

Figure 5-1: General block diagram of a logic gate circuit

The relationship between input and output logic levels of a gate circuit is illustrated as truth tables. For example the truth tables of a NOR, a half adder and a latch are shown in Table 5-1, Table 5-2 and Table 5-3 respectively.

A	B	NOR
0	0	1
0	1	0
1	0	0
1	1	0

Table 5-1: Truth table of a NOR

A	B	SUM	CARRY
0	0	0	0
0	1	1	0
1	0	1	0
1	1	0	1

Table 5-2: Truth table of a half adder

SET	RESET	Q_{i-1}	Q_i	Q_i’
0	0	0	0	1
0	0	1	1	0
0	1	0	0	1
0	1	1	0	1
1	0	0	1	0
1	0	1	1	0
1	1	0	X	X
1	1	1	X	X

Table 5-3: Truth table of a latch

The notations used in Boolean logic are:

$\cdot \equiv$ AND

$+ \equiv$ OR

’ $\equiv$ Negation

Boolean algebra and Boolean operators are used to express the relationship between input and output logic signals. The relationship is simplified using Karnaugh maps [18]. For example the Boolean expressions for the relationships between the input and output logic signals for a half adder and a latch are as follows:

Half adder: Sum: $A'\cdot B+A\cdot B'$

Carry: $A\cdot B$

Latch: $Q_i=SET\cdot RESET'+SET'\cdot RESET'\cdot Q_{i-1}$

$Q_i'=SET'\cdot RESET+SET'\cdot RESET'\cdot Q_{i-1}'$

Basic laws and theorems of Boolean logic [19]:

1· Distributive law: $A+(B\cdot C)=(A+B)\cdot(A+C)$

$A\cdot(B+C)=A\cdot B+A\cdot C$

2· De Morgan's theorem: $(A+B+C)'=A'\cdot B'\cdot C'$

$(A\cdot B\cdot C)'=A'+B'+C'$

3. Other useful theorems: a) $A+0=A$

b) $A\cdot 0=0$

c) $A+1=1$

d) $A\cdot 1=A$

e) $A+A=A$

f) $A\cdot A=A$

g) $A+A'=1$

h) $A\cdot A'=0$

i) $A''=A$

4. Commutative law: $A+B=B+A$

   $A\cdot B=B\cdot A$

5. Associative law: $(A+B)+C=A+(B+C)=(A+C)+B$

   $(A\cdot B)\cdot C=A\cdot(B\cdot C)=(A\cdot C)\cdot B$

To express the functions in terms of NOR gates, the above mentioned laws and theorems are used. For example an AND operation can be expressed in terms of NORs as follows:

$A\cdot B = (A\cdot B)''$ ------------------ (using Theorem 3i)

$(A\cdot B)'' = (A'+B')'$ ------------------ (using De Morgan's law)

$(A'+B')'= ((0+A)'+ (0+B)')'$ ------------------ (using theorem 3a)

Pictorially, this is shown in Figure 5-2.

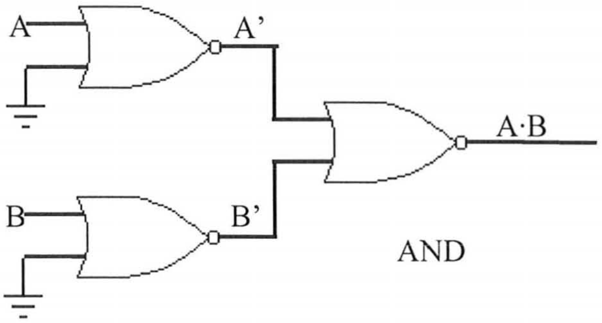

Figure 5-2: An AND using a combination of NORs

Logic gates make use of electronic switches to achieve ON/OFF states. An electronic switch can be in the form of a relay, a vacuum tube or a transistor. The transistor is a completely electronic three terminal device which satisfies all the 5 requirements needed to make a computing system and replaced the relay logic and vacuum tubes due to its small size, low power, high reliability and fast operation.

There are 5 basic requirements for logic devices to make digital circuits [19]. These are:

- **Non-linear characteristics:** Non-linearity is desired to maintain a sufficient signal-to-noise ratio even when several gates are cascaded in series. Digital electronic devices are superior to analogue devices. This is because the output of a device is restored to a standard value (high/low) after each step [21-22]. In a computer a large amount of communication among many devices is required. Thus the output of a device is connected to the input of subsequent device (s). As the output signal travels from one gate to another it gets attenuated. The loss of information due to the accumulation of losses is avoided by restoring the output of a device to a standard value (high/low) after each step [23]. Also, there is always some uncertainty in the performance of identical devices because of the variability of signals and the variability of the device characteristics themselves. Higher non-linearity is required if larger uncertainty is expected in the device behavior.

- **Power amplification:** Power amplification is necessary to have a high fan-out. Fan-out is the number of similar gates that can be driven in parallel by the driving gate. We need signal amplification (such as voltage amplification) as well as driving current to charge and discharge the line capacitance and input capacitance of the subsequent gates.
- **Concatenability:** Concatenability means that the input and output signals should be compatible i.e. they should be based in the same physical domain and impedance matched. If the input and output signals are in different physical domains, we cannot make integrated circuits without the use of transducers between the input and output; thereby increasing the complexity of the circuits to an unimaginable level.
- **Feedback prevention:** To execute a correct truth table the information should flow only in the forward direction. The input and output should be isolated. A transistor is a 3 terminal device in which the input and output are well-isolated by the gate capacitance.
- **Complete set of Boolean operators:** The basic gates like NAND gates and NOR gates are the universal gates. All the other sequential and combinational logic functions can be expressed as a combination of NAND/NOR using Boolean algebra. For example Figure 5-3 (a), (b) and (c) show a half adder, a clock, and a latch that could be realized by cascading NOR gates.

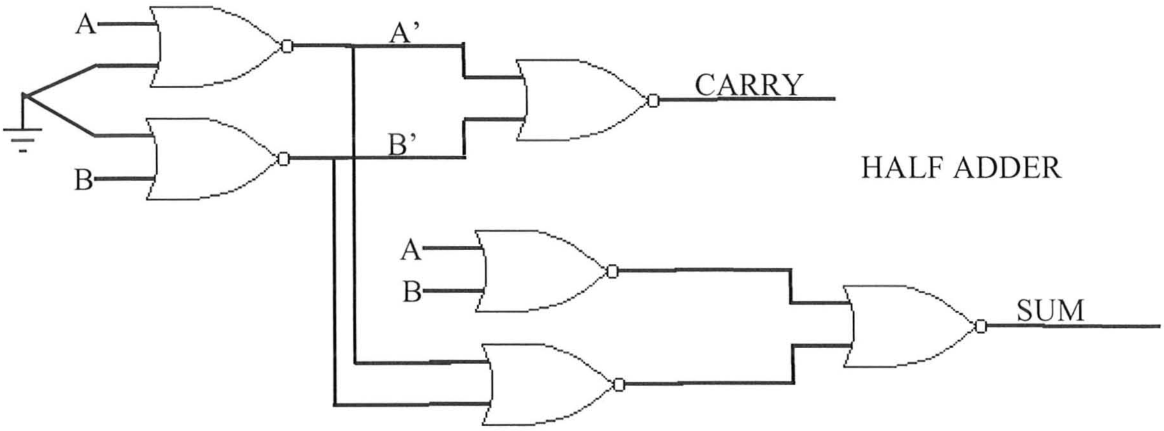

(a)

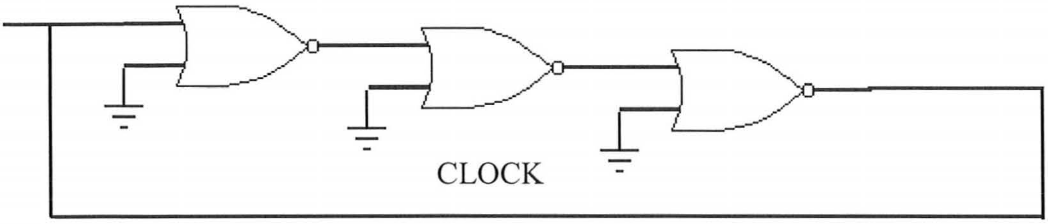

(b)

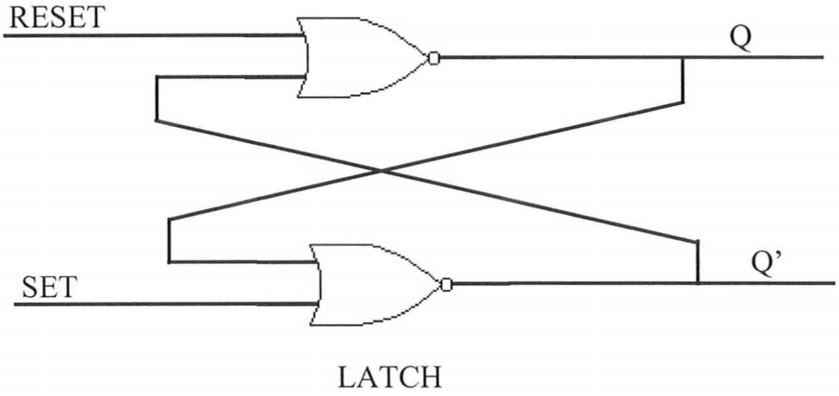

(c)

Figure 5-3 (a) Half adder (b) clock and (c) latch realized by cascading NOR gates

CMOS technology has an additional virtue that very low power can be achieved by designing inverters from both n-type and p-type transistors. While this is highly desirable at a system level to reduce power consumption, it is not strictly necessary to make a functioning computing system.

Variations in control pressures are expected in larger systems. Thus to design a system with higher tolerance, a flattened region which could demagnify the effect of small variations in control pressure on the output pressure, is desired. Special kind of transfer function with flattened regions like shown in Figure 5-4 is preferred as it is less susceptible to variations [35].

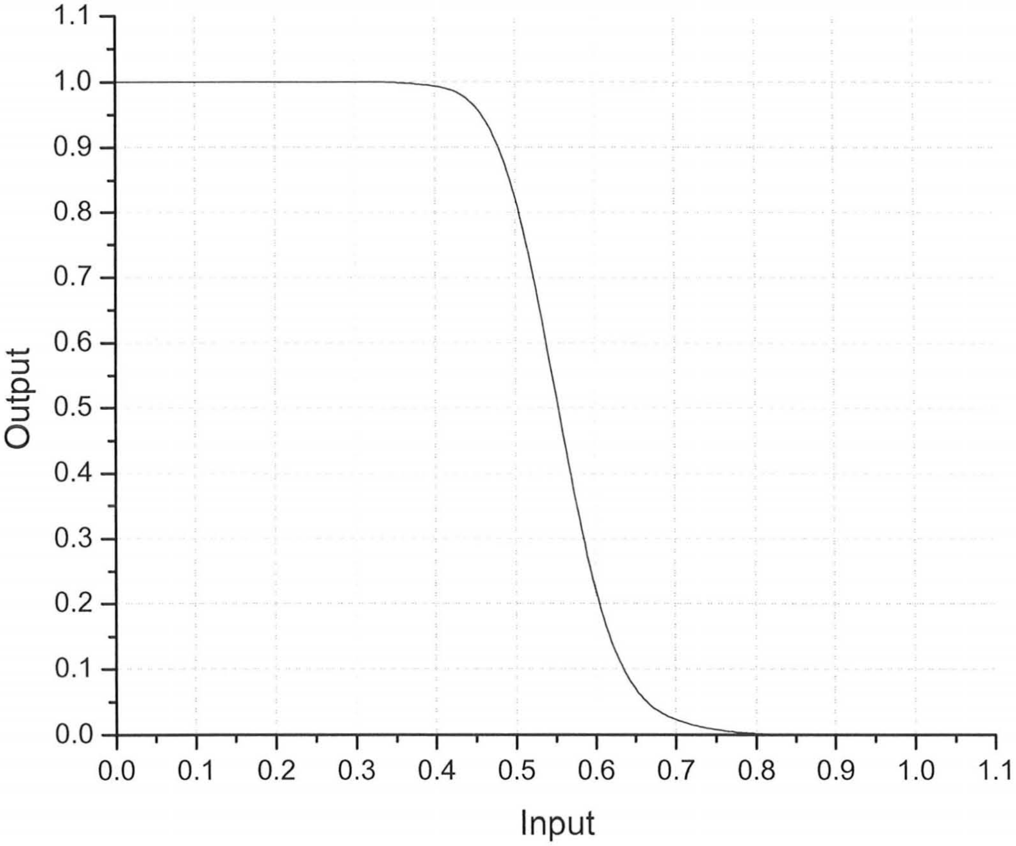

Figure 5-4: A transfer curve which has a lower susceptibility to variations

CHAPTER 6 COMPUTATIONAL FLUID DYNAMICS

Computational fluid dynamics is the analysis of fluid dynamics numerically. ANSYS-CFX, CFD-ACE and fluent are some of the commercial software packages available for computational fluid dynamics analysis. ANSYS-CFX was used for this project. All the results were obtained using three-dimensional analysis.

$$\rho\frac{\partial U}{\partial t}+\rho(U\bullet\nabla)U=-\nabla P+\rho g+\mu\nabla^2 U+(\frac{\mu}{3})\nabla(\nabla\bullet U) \quad (6\text{-}1)$$

The Navier Stokes equation (Equation 6-1) is a partial differential equation (PDE) which is very hard to solve analytically. Except for a few simple cases, an exact solution cannot be obtained in closed form. The ANSYS simulator solves the PDE numerically for a given set of boundary conditions and initial conditions. ANSYS-CFX uses a finite-element/finite-volume approach to discretize the Navier Stokes equations. In a finite-element/finite-volume approach, the solution domain is divided into a number of cells known as control volumes. The conservation equations (mass, momentum and energy) are numerically integrated over each of these computational cells/control volumes.

The following equations are used by ANSYS-CFX [24]:

$$\rho\frac{Du_i}{Dt}=F_i+\frac{\partial\sigma_{ij}}{\partial x_j}, \quad (6\text{-}2)$$

where ρ is the density, u_i is the velocity component along i, and F_i is the external force component along i unit volume. $\frac{D}{Dt}$ is defined as:

$$\frac{D}{Dt}=\frac{\partial}{\partial t}+u_j\frac{\partial}{\partial x_j}, \quad (6\text{-}3)$$

Mass conservation equation:

$$\frac{D\rho}{Dt} + \rho \frac{\partial u_i}{\partial x_i} = 0 \qquad (6\text{-}4)$$

For Newtonian liquids (i.e. for our NOR devices where the working fluid is water), the stress tensor is linearly related to the deformation tensor.

$$\rho \frac{Du_i}{Dt} = F_i - \frac{\partial p}{\partial x_i} + \mu \frac{\partial^2 u_i}{\partial x_j^2} \qquad (6\text{-}5)$$

A good mesh is an important aspect of computational fluid dynamics. A tetrahedral mesh was used for our model. It is necessary to have a finer mesh in the regions where vortices are involved. At the same it is wise to use a coarse mesh in the remaining regions to utilize the available computation resources efficiently. A picture showing the regions where finer mesh was used for our NOR gate is show in Figure 6-1.

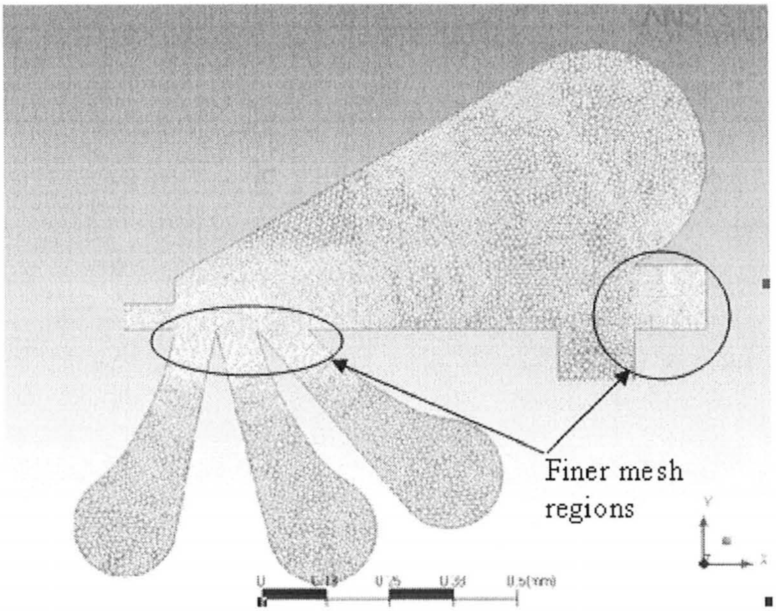

Figure 6-1: A picture showing finer mesh regions in our model

The fluid domain in our models was water of density ~1000 Kg/m^3 and viscosity = 10^{-3} Kg/m.s. The supply was set to an 'inlet' boundary condition of constant velocity or constant pressure as explained in Section 7.4. The control ports and vents were set to 'opening' boundary condition because we expect both the flow-in and flow-out of the domain through the control ports and vents.

The simulator stops iterating either if the maximum number of iteration is reached or if the convergence criterion is satisfied. The number of iterations and the convergence criterion should be properly chosen to achieve the required accuracy in the shortest time possible.

The laminar flow model was used to model our devices. The critical Reynolds number is different for different geometries. For example for a pipe the transitional regime is defined by the range 1000<Re<2300. We chose a Reynolds number of 600 for our simulations. For our geometry the critical Reynolds number is ~600 [8]. Therefore we chose the laminar model to simulate our devices.

The time dependence of the flow characteristics can be specified as either steady state or transient. Steady state simulations are defined as those whose characteristics do not change with time and whose steady conditions are assumed to have been reached after a relatively long time interval. They therefore require no real time information to describe them. Steady state simulations were used for the design and optimization of the basic NOR gate because no real time information was required in doing so. Transient simulations were used to analyze our clock and latch.

The simulator not only helped in testing the various initial designs in a comparatively short time but also economically. If we would have to fabricate the devices of different dimensions and geometries, we would have to spend a lot more resources to buy the wafers, photo resist and to make the masks. CFX-post allows the user to plot color plots which increased our understanding of the jet mechanics, pressure-controlled jet deflection effects, momentum interaction effects and wall-attachment effects.

CHAPTER 7 RESULTS AND DISCUSSIONS

The project started with the thought that a NOR gate based on pressure-controlled jet deflection can be achieved even in the laminar flow regime. It was soon realized that jet formation is required for our NOR to work properly. A jet is defined as a flow which has enough inertia to maintain the flow directionality (Refer to Section 7.5). This flow directionality is essential for the jet to flow straight from the supply to the outlet when pressure in both the control ports is low. Jet formation is usually observed in the turbulent regime. At low Reynolds number the viscous forces dominate the inertial forces. The viscous forces disperse the flow to neutralize the pressure differential. But there is a range of Reynolds number in the laminar regime at which a good jet is observed. A poor jet is observed at Re~300. It has been reported in the literature that a laminar jet is in the transition regime for Reynolds number>600 for our device geometry [8]. Thus a Reynolds number between 300 and 600 leads to a viable laminar jet.

The ON and OFF states of a device are introduced here to help the reader understand the rest of this thesis. The procedures that we used to plot the transfer curves, the output characteristic curve, the load lines and the fan-out in this thesis are also introduced.

The transfer curve is defined as a relationship between the input and output signals of a device. Figure 7-1 shows an arbitrary transfer curve. The output values below P_c^* are considered as low (OFF). The output values above P_c^* are considered as high (ON). This is because any value above P_c^* will regress to the maximum after infinite iterations. For example as shown in Figure 7-2 a value of 0.586 regresses to 0.877 in just 2 iterations. Similarly any value below P_c^* will regress to 0 after infinite iterations. The rate of regression depends on the non-linearity of the transfer curve. It should be noted that we did not considered noise margin in this thesis.

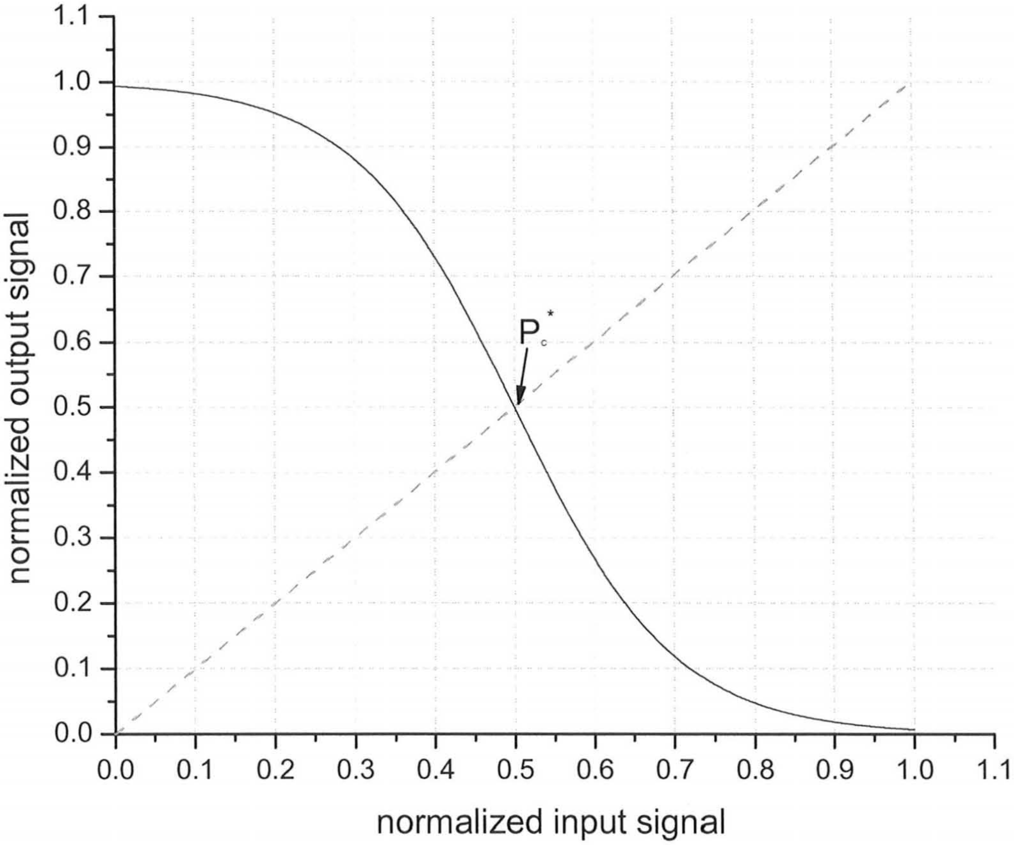

Figure 7-1: An arbitrary transfer curve $\left(y = 0.5\tanh(5(0.5 - x) + 1)\right)$

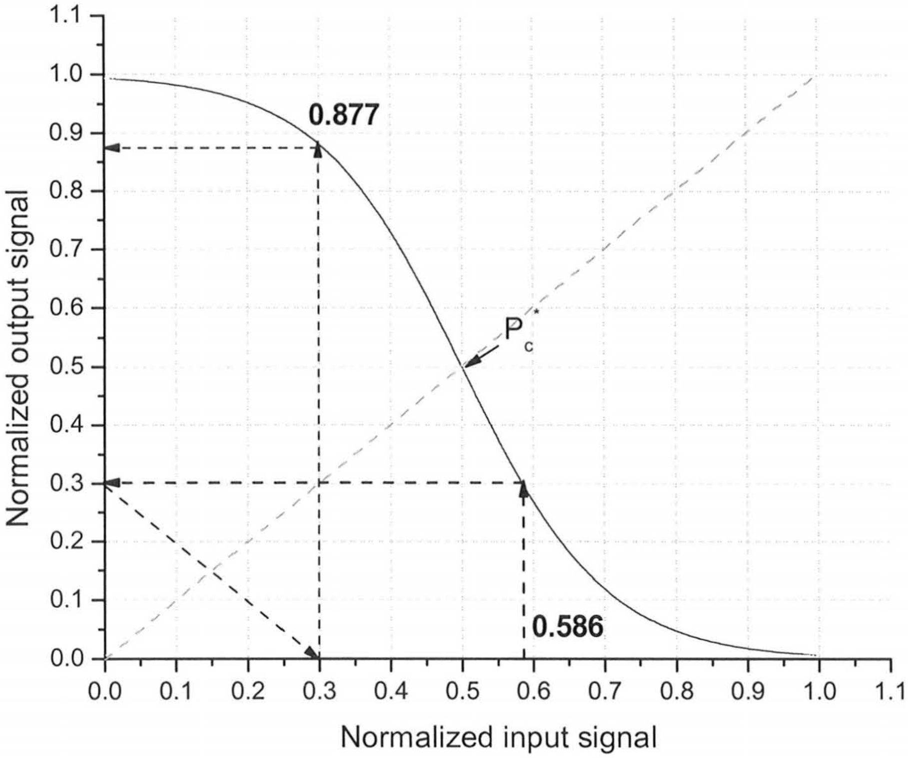

Figure 7-2: A value above P_c^* regress to maximum

To plot the transfer curves, the control pressure was varied and the corresponding output pressure under the blocked conditions was simulated. The data was normalized with respect to the maximum pressure recovered under the blocked load conditions. One such transfer curve is shown in Figure 7-3 (a). The physical basis of the transfer curves of our devices is quite complex. Therefore we do not expect the transfer curves to fit to any simple function. However, the shape is quite close to the hyperbolic tan function. Thus we have fitted our transfer curves to hyperbolic tan function. We have used piecewise lines for the cases where hyperbolic tan function is not a good fit for our transfer curves.

The output characteristic curve was plotted by varying the output pressure and simulating the corresponding output flow rates as shown in Figure 7-3 (b). The input impedance of the device is called the load line because the input impedance is equal to the load seen by the driving element when it is connected to a similar device in series. The load lines were plotted by simulating the control flow rate corresponding to the applied control pressure as shown in Figure 7-3 (c).

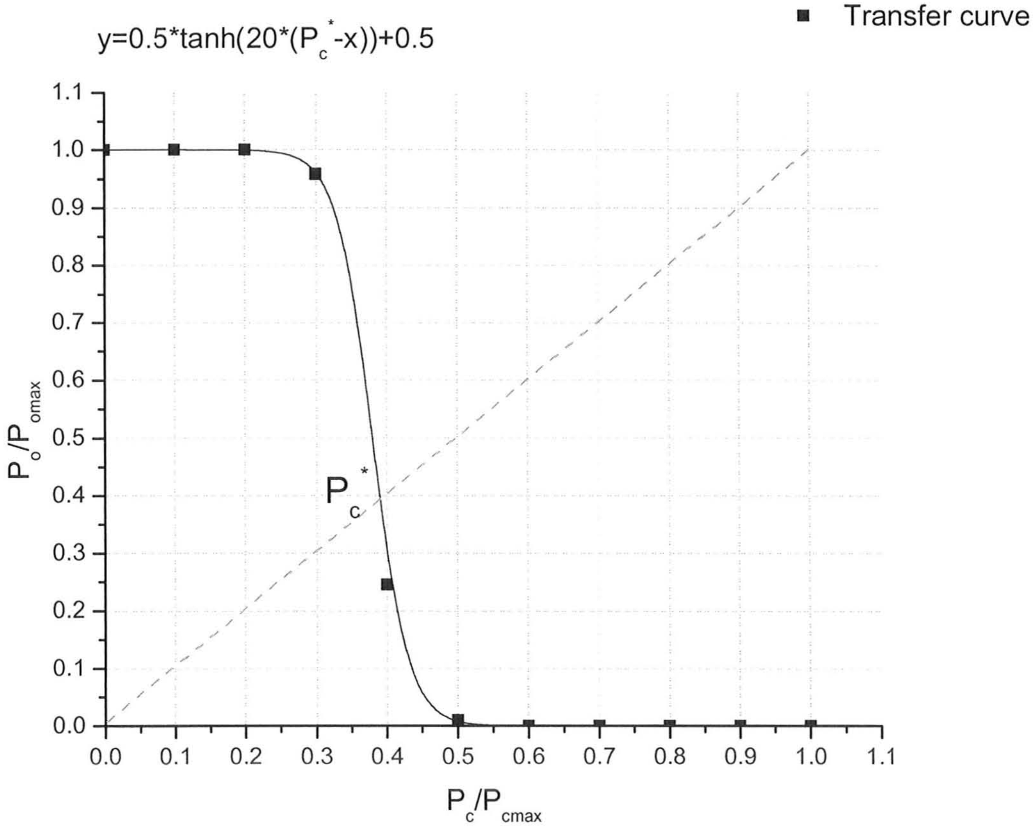

Figure 7-3 (a): Transfer Characteristic curve (L=15w, W_c=90μm, W_o=2w and Re=600, P_{omax}=P_{cmax}=20KPa)

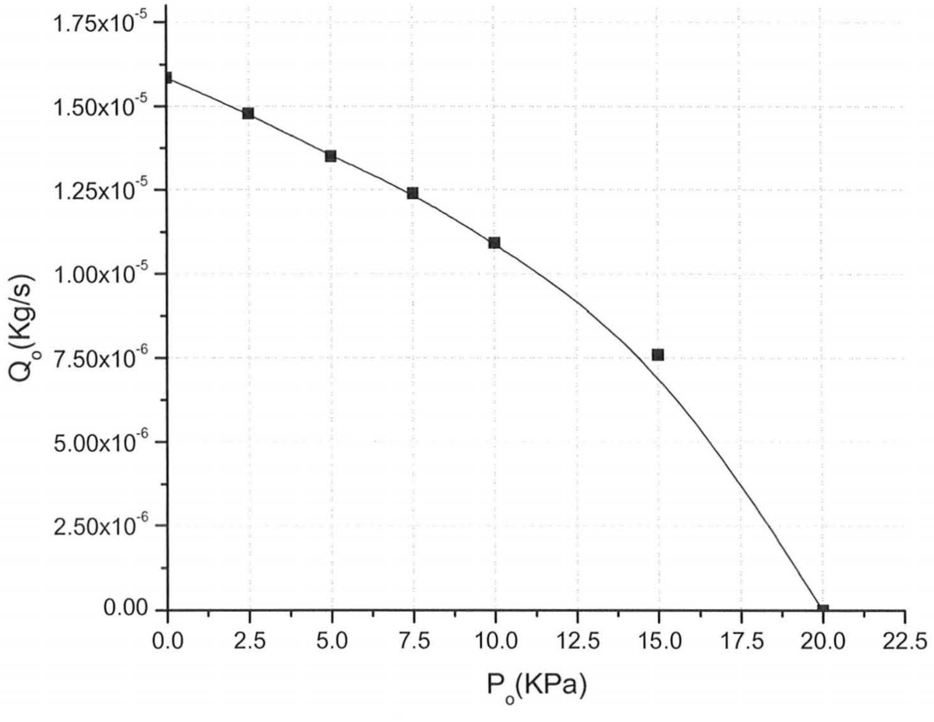

Figure 7-3 (b): Output Characteristic curve (L=15w, W_c=90μm, W_o=2w and Re=600)

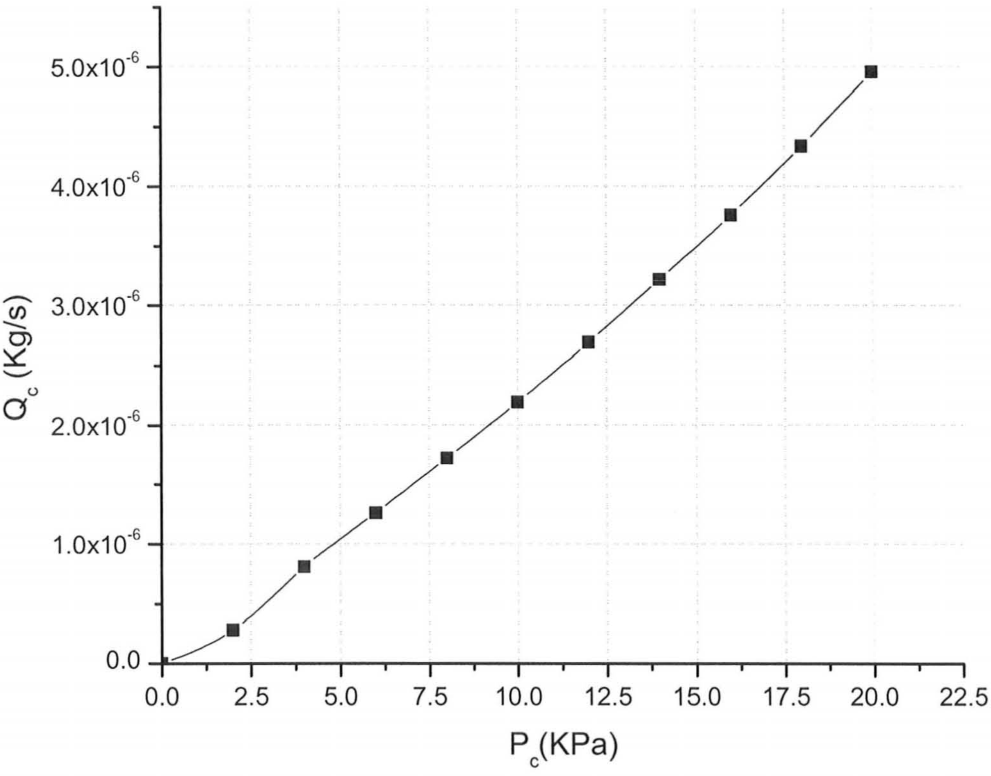

Figure 7-3 (c): Load line (L=15w, W_c=90μm, W_o=2w and Re=600)

The output of a NOR gate should satisfy two criteria to be able to drive the subsequent gates. Firstly, the output pressure in the ON case of the driving gate should be enough to cause a deflection in the driven gates. Secondly, the flow in the outlet should be balanced by the flow in the control ports. Thus the following procedure was used to calculate the fan-out of a device. P_c^* (obtained from the transfer curve), the output characteristic curve and the load line were superimposed as shown in Figure 7-4. The fan-out was calculated as the ratio of the flow rate corresponding to the point of intersection of the P_c^* line with the output curve to the flow rate corresponding to the point of intersection of the load line with the P_c^*.

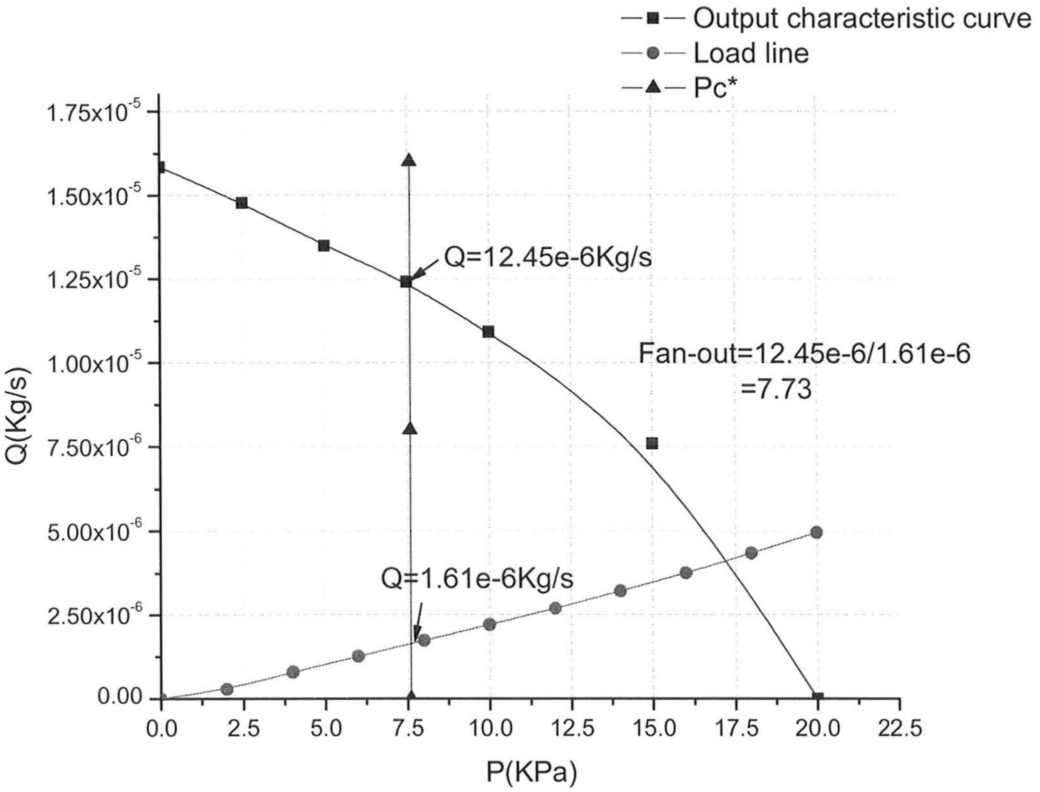

Figure 7-4: A plot showing the superimposed P_c^* (obtained from the transfer curve), output characteristic curve and the load line (L=15w, W_c=90μm, W_o=2w and Re=600)

This approach naturally follows from that used for comparable electronic devices [39].

7.1 VENT NEAR OUTLET

As mentioned in Chapter 3 no physical insights were provided in the paper by Walker and Trask [8] about the vent near the outlet. In this section the physical basis of the vent near the outlet is explained. The first NOR that was modeled is shown in Figure 7-5.

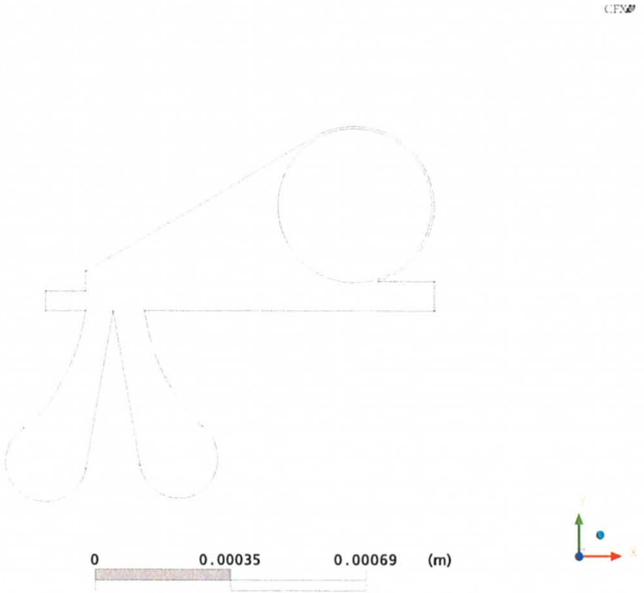

Figure 7-5: First modeled NOR (Width of supply nozzle=50μm, height=50μm and length=750μm)

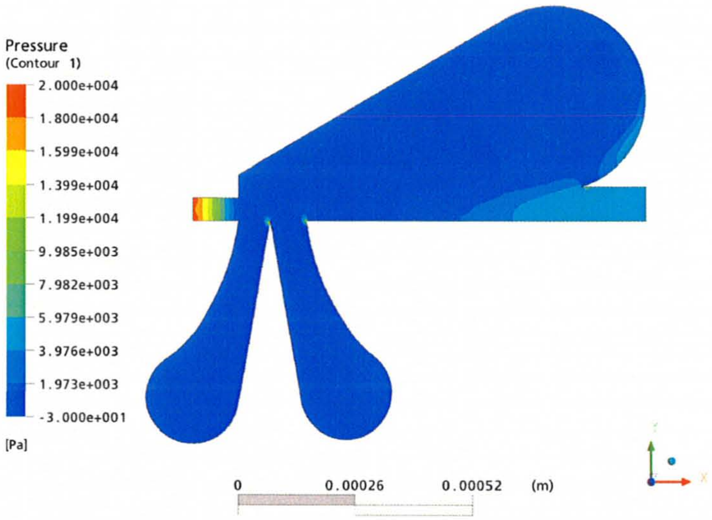

Figure 7-6: Low output pressure recovery (Re~600 and xy plane at z=25μm)

As shown in Figure 7-6, the input static pressure is 20KPa and the output pressure recovery is ~5.5KPa for blocked load. The pressure recovery is low because of the following reason: The impedance of the circular vent is much lower than the impedance of the outlet. Thus to minimize losses, the supply jet prefers to flow into the circular vent than the outlet.

The pressure recovered at the output acts as an input signal for the next stage gates. In other words, the output pressure of a device is used to drive the subsequent gates. Higher output pressure recovery is necessary to have higher fan-outs.

It was concluded that some sort of vent symmetry is required to allow the jet to flow into the outlet when the pressure in both the control ports is low. A symmetrical vent was thus added and the new design is shown in Figure 7-7.

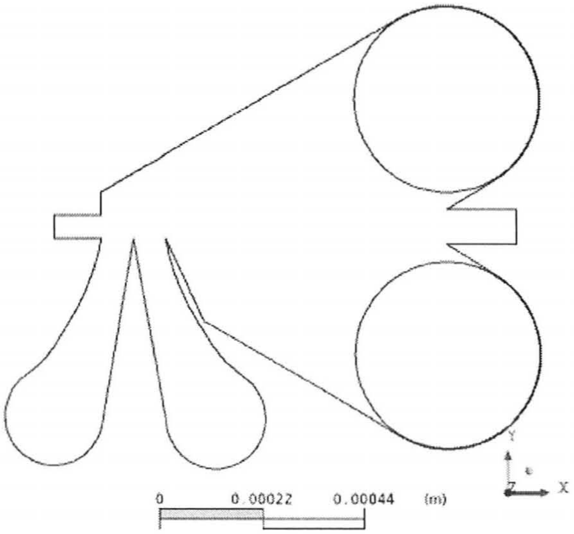

Figure 7-7: Design with symmetrical vents (Width of supply nozzle=50µm, height=50µm and length=750µm)

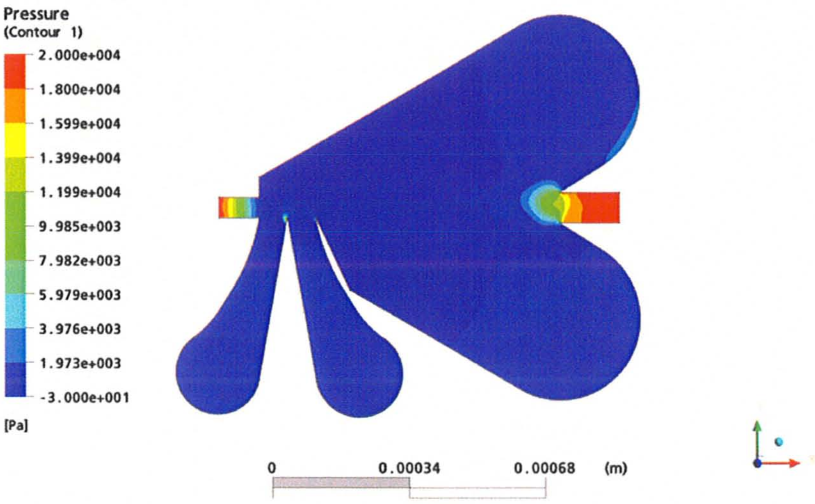

Figure 7-8: Increased output pressure for a symmetrical design (Re ~600 and xy plane at z=25μm)

The top and bottom vents are symmetrical. There is no reason for the supply jet to flow into one vent over the other vent. Thus due to the presence of a vent symmetrical to the top circular vent the supply jet has to flow straight through before it splits into two circular vents. As a result as shown in Figure 7-8, the output pressure recovery was increased to ~20KPa.

Figure 7-9 shows the transfer curves for the design shown in Figure 7-7 with control port widths of 70μm and 100μm.

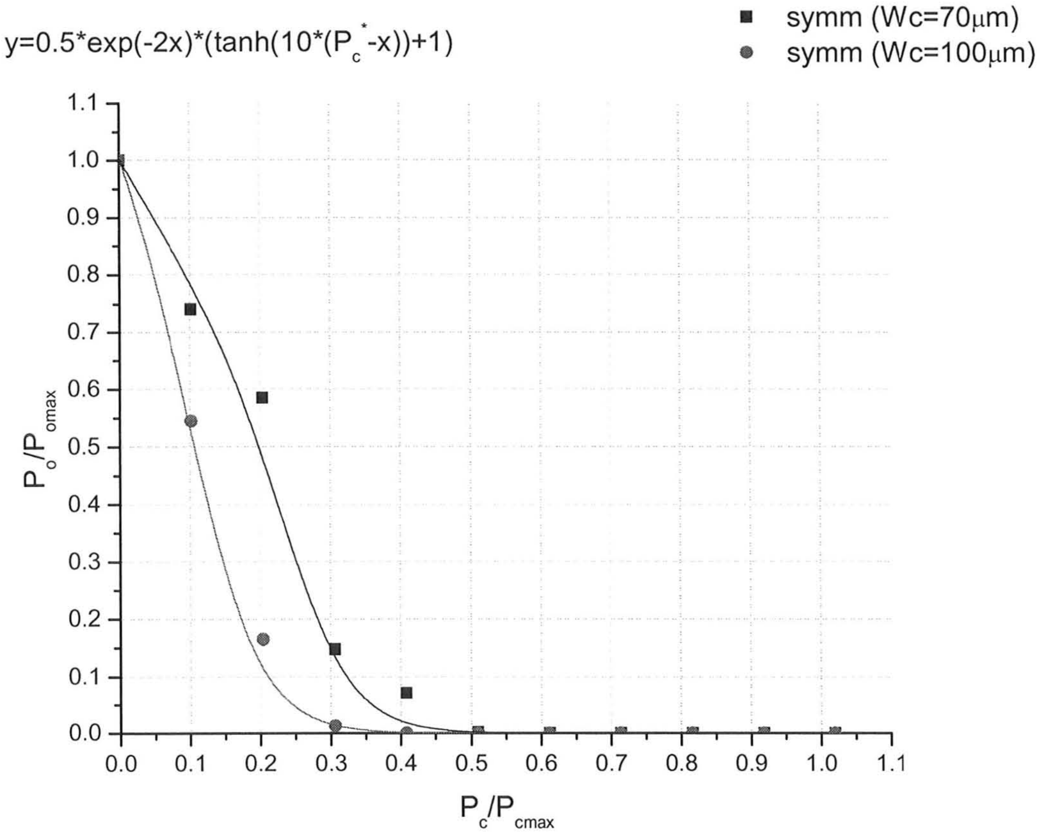

Figure 7-9: Transfer curves of a device with symmetrical vents (L=15w, W_o=1.5w, W_c= 70μm and 100μm, Re~600 and P_{omax}=P_{cmax}=20KPa)

The output pressure was expected to drop on applying the control pressure because the supply jet is deflected on applying control pressure. It was however, observed that even small control pressures could result in huge jet deflections for this design. Thus the output pressure drops rapidly to zero with an increase in control pressure. This is not a good transfer curve as explained in Chapter 5.

If a design with a straight bottom wall with a vent close to the outlet was considered as shown in Figure 7-10 (and as considered by Walker and Trask [8]), then good pressure recovery and better non-linearity in the transfer curves was obtained. A comparison of the transfer curves of the design shown in Figure 7-7 and Figure 7-10 is shown in Figure 7-11. The basis of the non-linearity in transfer curves is discussed in Section 8.5.

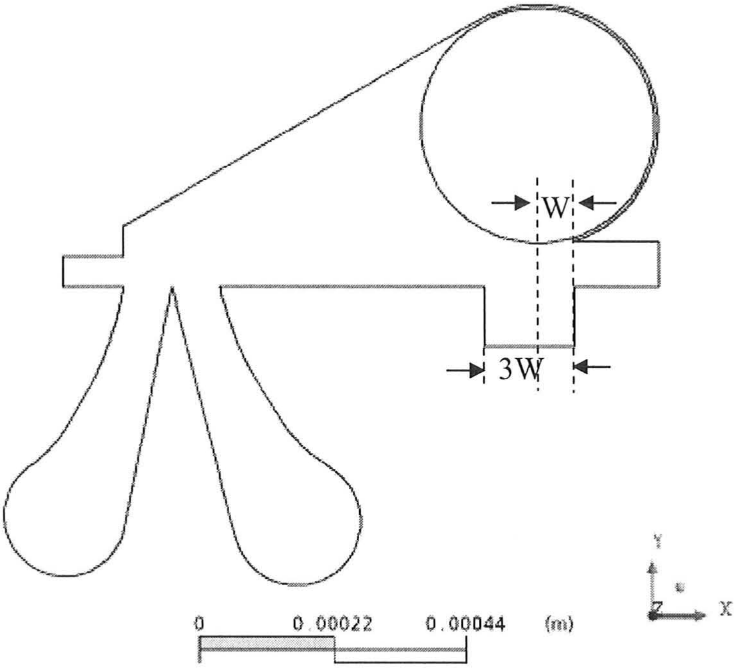

Figure 7-10: Design with a straight bottom wall and a vent close to the outlet (size and position of the bottom vent are also marked)

The size of the bottom vent and its position with respect to the circular vent play an important role in the pressure recovery. If the vent is too small, the output pressure recovery is low and the design is equivalent to that shown in Figure 7-5. And if it is too big, it reduces the output mass flow rate. The optimum size of the vent for a fixed size of the circular vent was found to be 3W where W is the width of the supply nozzle. The optimum position of the edge of the bottom vent with respect to the centre of the circular vent was found to be displaced by W. These design parameters are also marked in Figure 7-10.

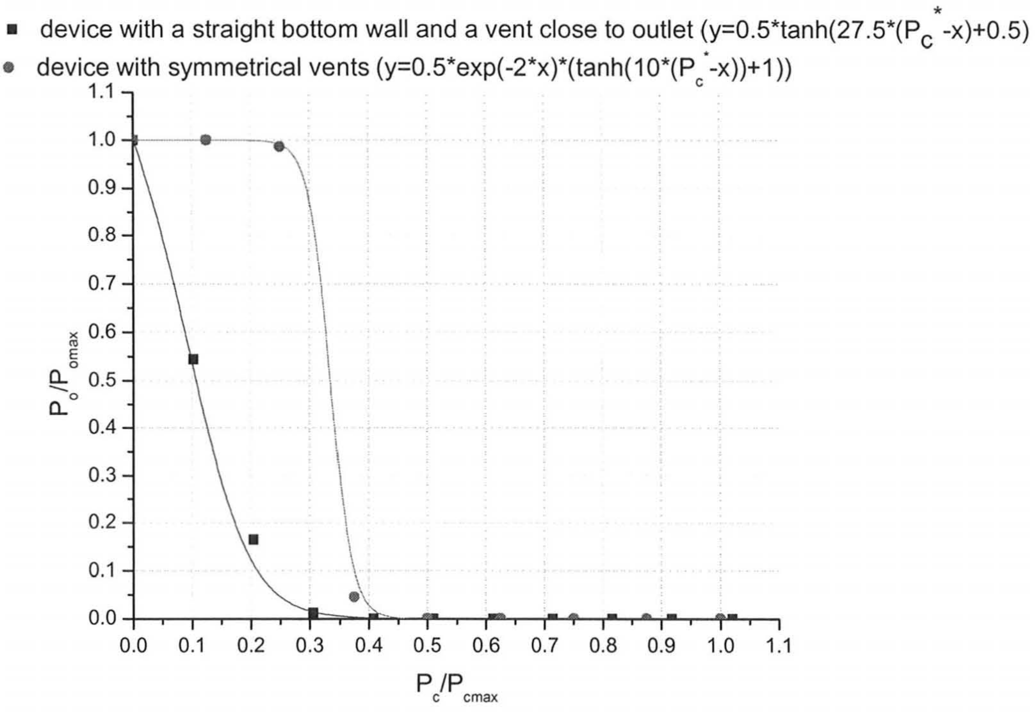

Figure 7-11: Transfer curves of a design with symmetrical vents and a design with a straight bottom wall and a vent close to the outlet (L=15w, W_o=1.5w, W_c=100µm, Re~600 and P_{omax}=P_{cmax}=20KPa)

To summarize, Walker and Trask [8] did not explain why they chose to have a straight bottom wall with a vent near the outlet in their paper. In the above section we have explained the reason for the vent close to the outlet and advantages of a straight bottom wall compared to the design with symmetrical vents.

7.2 OPTIMIZATION

A modeling approach was formulated to achieve an optimized design. The fan-out was optimized with respect to the control ports width (W_c), the outlet width (W_o) and the length (L) at a constant Reynolds number of 600. An explanation of why the Reynolds number of 600 was chosen is given in Section 7.5. The design used for optimization is shown in Figure 7-12. The working fluid is water. The width of the supply nozzle is 50μm and the height is 50μm.

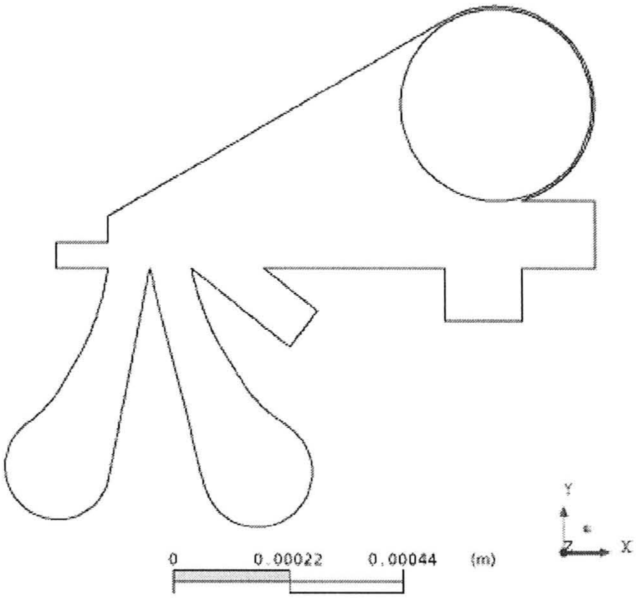

Figure 7-12: Design used for optimization

7.2.1 WIDTH OF CONTROL PORTS

For a fixed Reynolds number and geometry, as the width of the control port is varied the transfer function shifts as shown in Figure 7-13. As the width of the control port reduces, higher control pressures are required to switch the device from ON to OFF. This is because the angle of deflection of the resultant jet is a function of the control pressure and control port width as shown in Equation 3-9. Fan-out as a function of control port width is shown in Figure 7-14 (a).

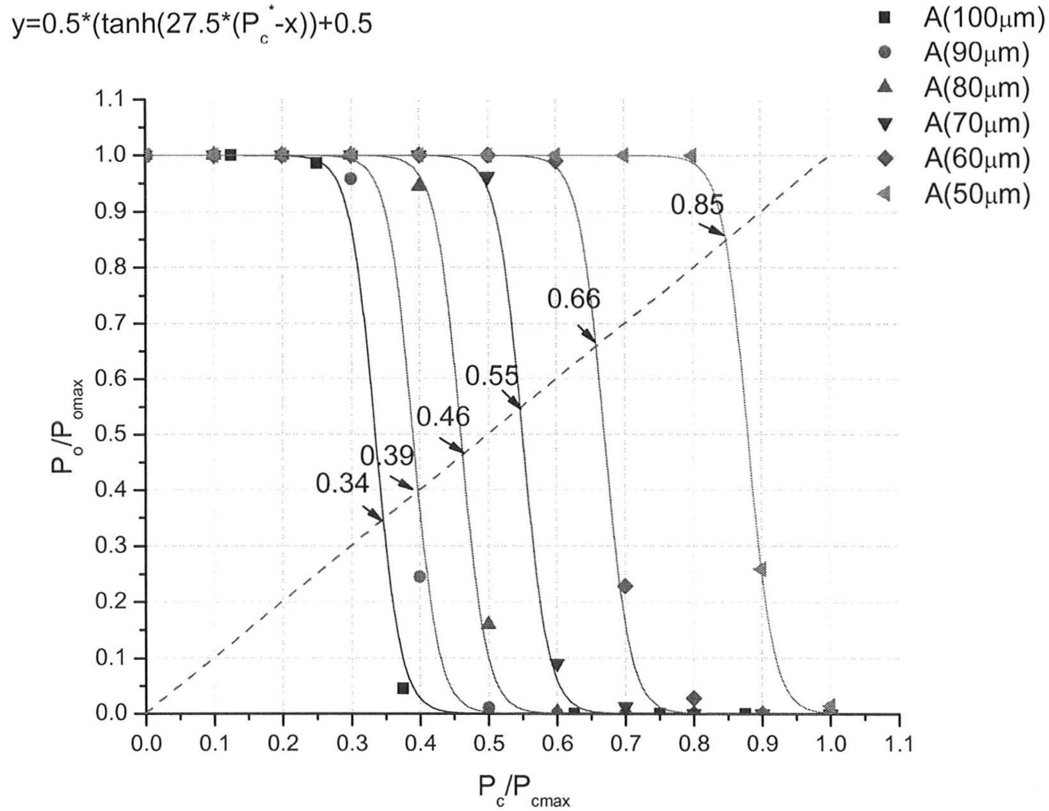

Figure 7-13: Transfer functions for different widths of the control port (Re~600, L=15w, W_o=1.5w and P_{omax}=P_{cmax}=20KPa)

As mentioned and shown in Figure 7-4 previously, fan-out is the ratio of flow rate corresponding to the intersection of the P_c^* line with the output characteristic curve vs. the flow rate corresponding to the load line with the P_c^* line. Figure 7-14 shows that fan-out increases with an increase in the control port width for a fixed Reynolds number and geometry. This is because at higher control port widths, the pressure required to deflect the jet from the ON to OFF position decreases which in turn increases the flow rate corresponding to the intersection between the P_c^* line and the output characteristic curve; hence increasing the fan-out. The above explanation is illustrated graphically in Figure 7-15.

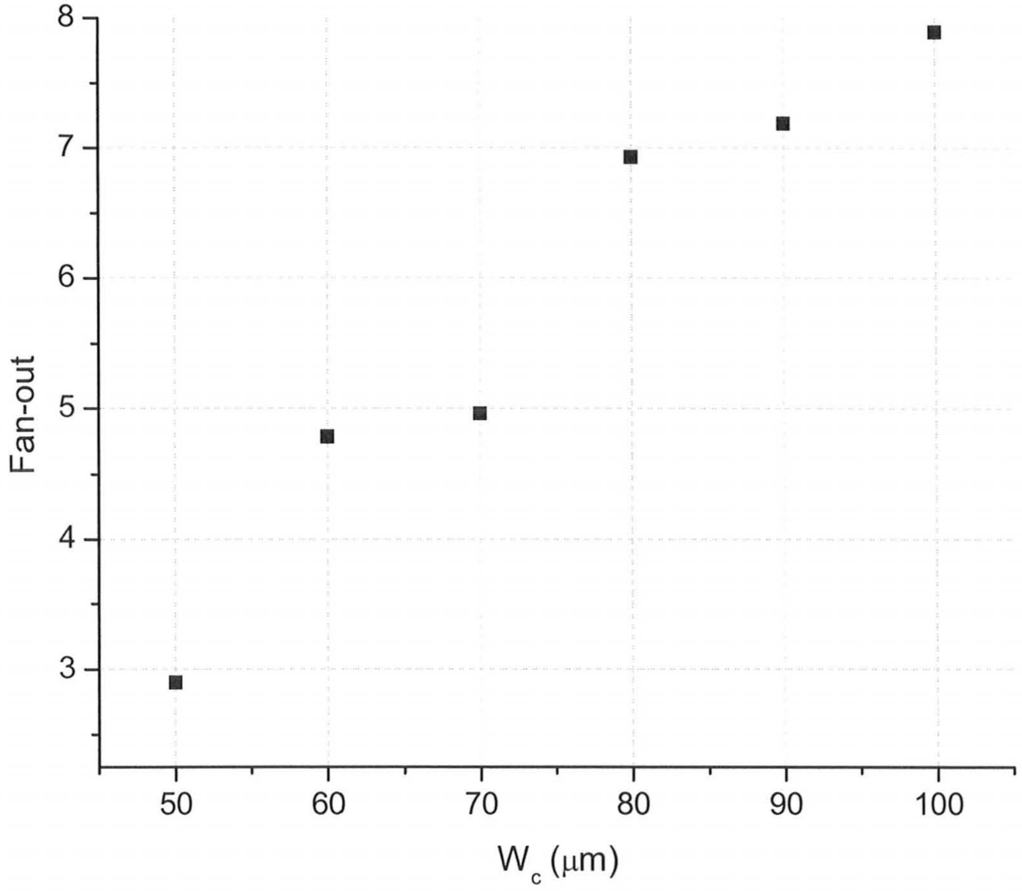

Figure 7-14: Fan-out as a function of control port width (Re~600, L=15w, W_o=1.5w)

Consider:

$$P_c^* = P_{omax}/2 \tag{7-1}$$

Equation 7-1 is chosen as a constraint in the further optimization of fan-out because it is a desirable operating point at a system level (as explained in Chapter 5). For future simulations W_c was chosen so as to satisfy Equation 7-1 for a fixed Reynolds number and geometry.

In the following sections the fan-out is optimized with respect to the outlet width (W_o) and the length (L) with the constraint of Equation 7-1.

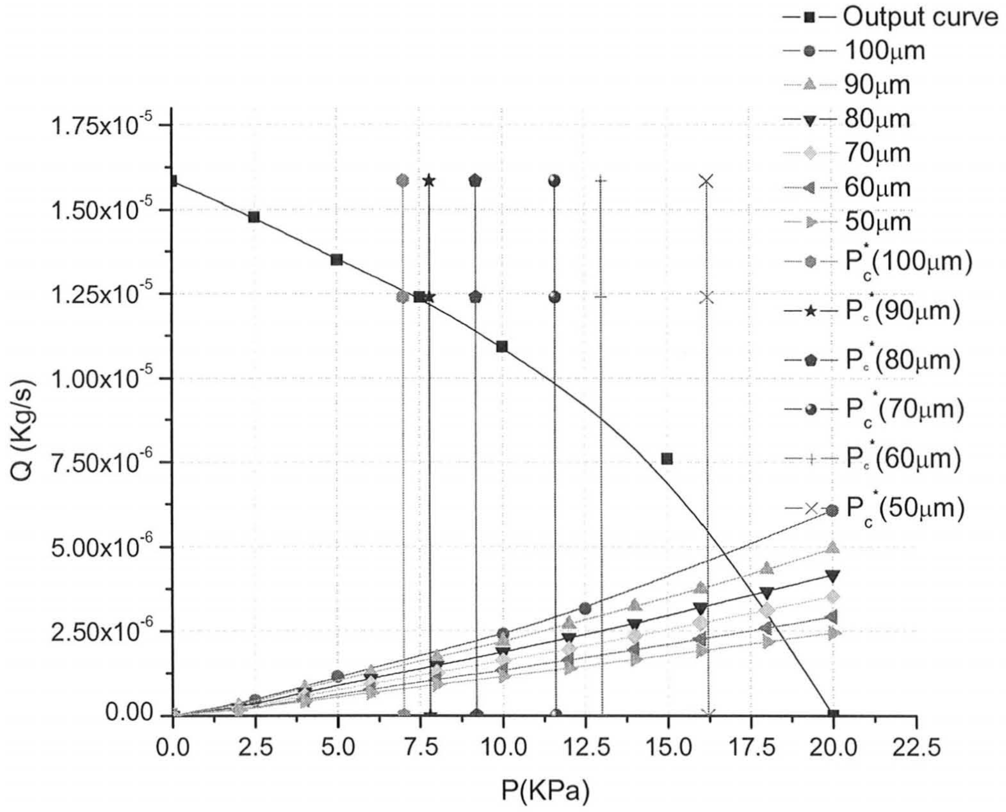

Figure 7-15: Explanation for a point of maximum fan-out with respect to control port width (Re~600, L=15w and W_o=1.5w)

7.2.2 OUTLET WIDTH

As we will show in Figure 7-21 the percentage of jet captured at the outlet is a function of the outlet width for a fixed length and Reynolds number. We will show that it is necessary to capture an appropriate percentage of the supply jet at the outlet. The percentage of the captured jet has an effect on the output characteristic of the device and also on the fan-out. Thus the output width is the second design parameter that is varied. The output width is varied for a fixed length and Re~600. As mentioned previously, it is desirable (from a system perspective) to find a control port width which satisfies Equation 7-1. Thus the control port width is varied for each output width to determine the control port width which satisfies Equation 7-1 for a fixed length and outlet width. The transfer functions satisfying Equation 7-1 for a fixed length and Reynolds number but different outlet widths is shown in Figure 7-16.

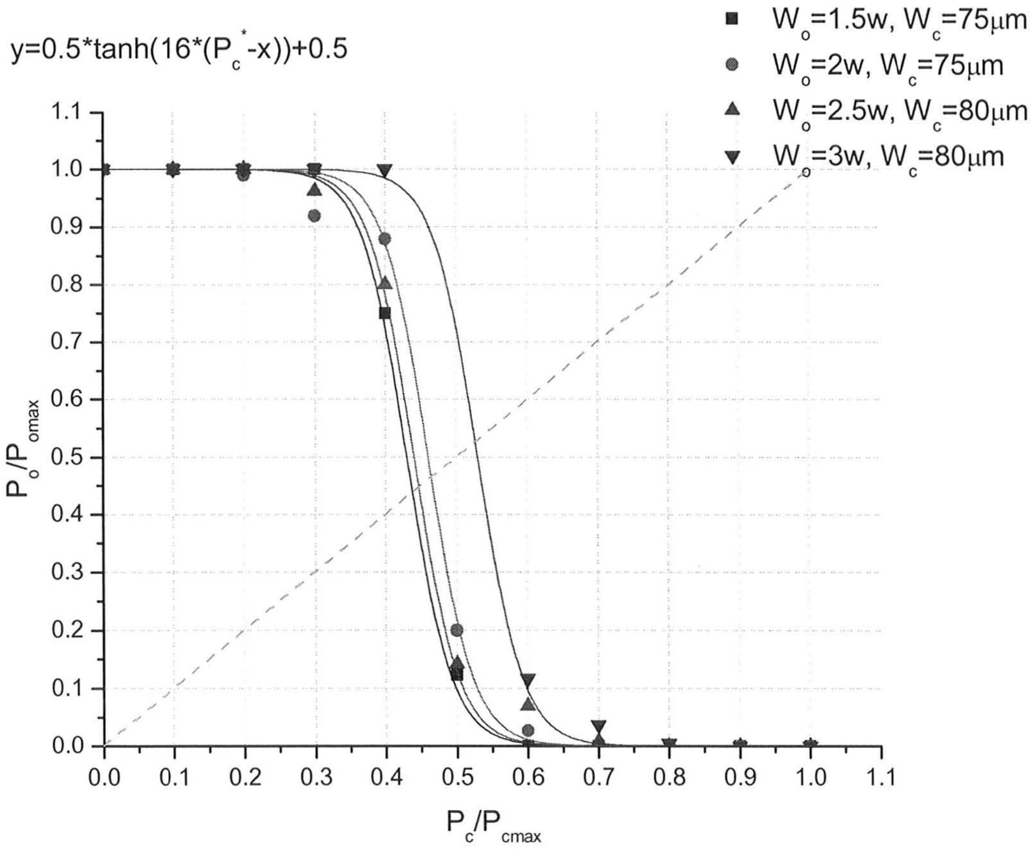

Figure 7-16: Transfer function for different outlet width (Re~600, L=15w, $P_{omax}=P_{cmax}$=20KPa and W_c corresponding to $P_c^*=P_{omax}/2$)

The maximum fan-out for different outlet widths for length=15w at Re=600 is plotted in Figure 7-17.

The fan-out increases until W_o=2.6W and then it begins to drop. As the width of the outlet increases for a fixed length and Reynolds number, higher percentages of the supply jet can be captured. In other words, an increase in the outlet width lowers the outlet impedance. Therefore, the flow rate corresponding to the point of intersection between the P_c^* line and the output characteristic curve increases. As a result the fan-out increases. A peak is however, observed as the outlet width is further increased because the actual angle ($\tan \theta^*$, Refer to Subsection 7.2.3) by which the jet has to be deflected to switch the device from ON to OFF increases with an increase in the outlet width. Thus the width of the control port has to be increased to switch the device from ON to OFF to satisfy Equation 7-1. The increased control port width leads to an increase in the flow rate corresponding to the point of intersection between the load line and P_c^* line, thereby reducing the fan-out. This is illustrated graphically in Figure 7-18 (a), (b), (c) and (d).

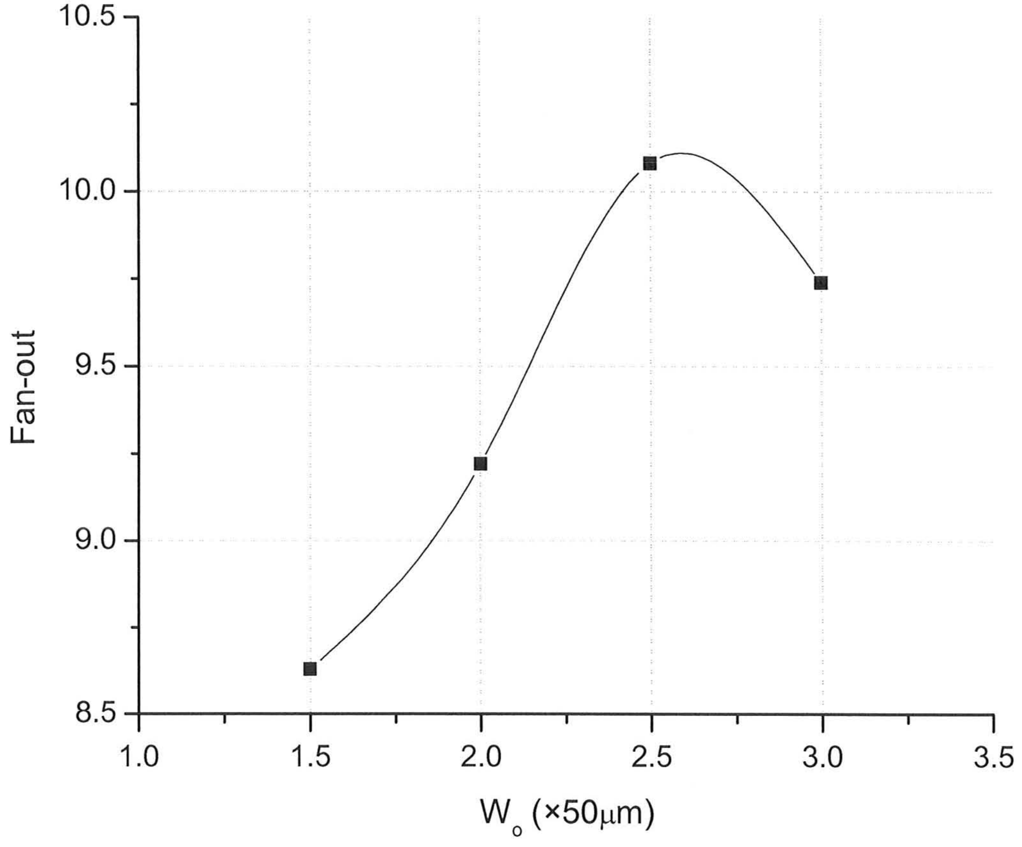

Figure 7-17: Fan-out vs. outlet width (Re~600, L=15w and W_c corresponding to $P_c^*=P_{omax}/2$)

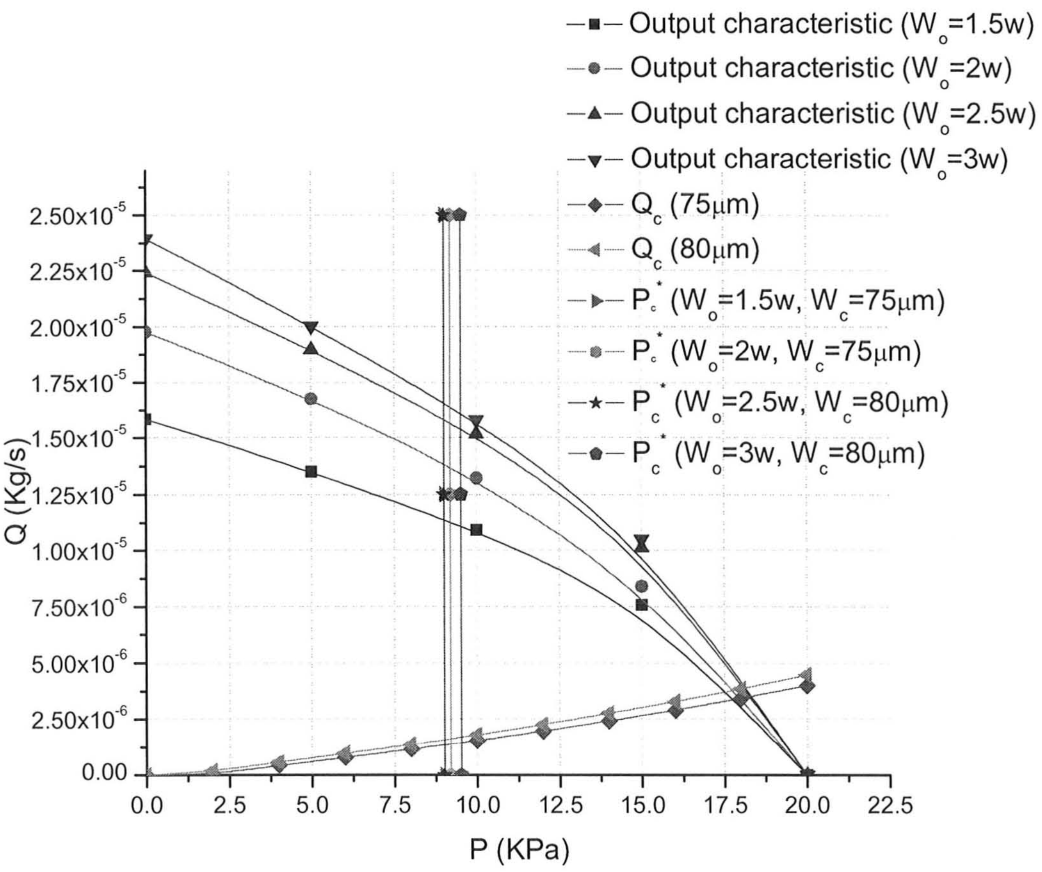

Figure 7-18 (a): Explanation for a point of maximum fan-out with respect to outlet width for L=15W (Re~600 and W_c corresponding to $P_c^* = P_{omax}/2$)

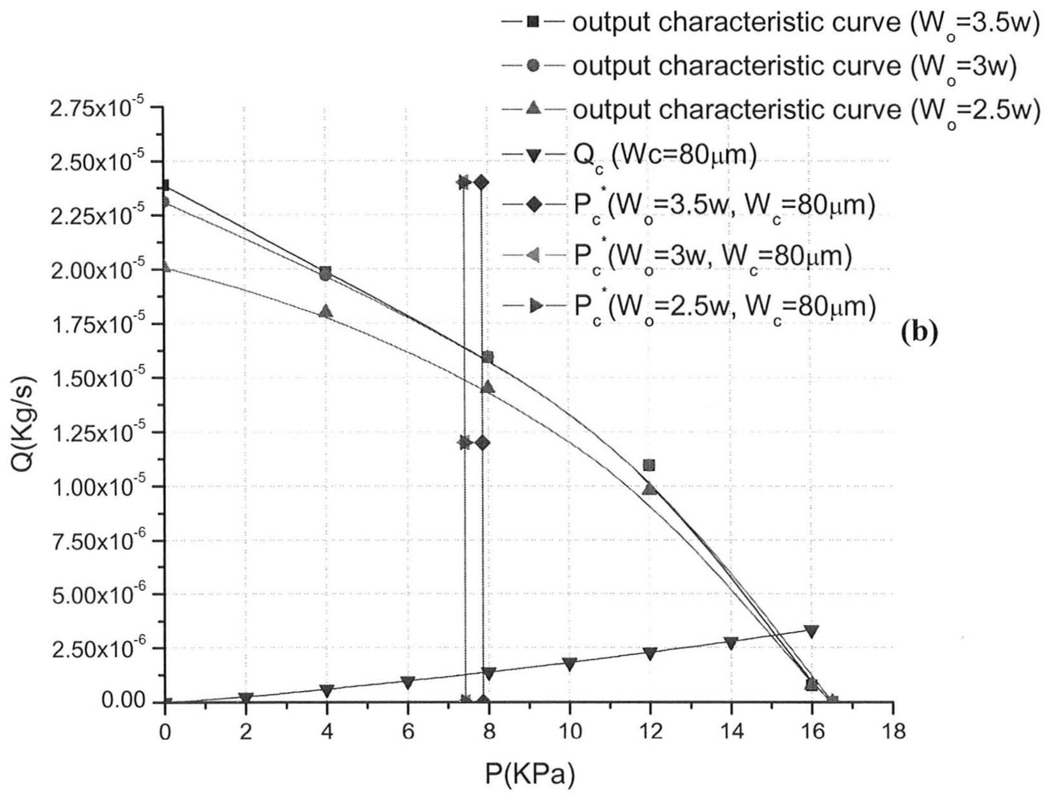

Figure 7-18: (b) Explanation for a point of maximum fan-out with respect to outlet width for L=18W (Re~600 and W_c corresponding to $P_c^*=P_{omax}/2$)

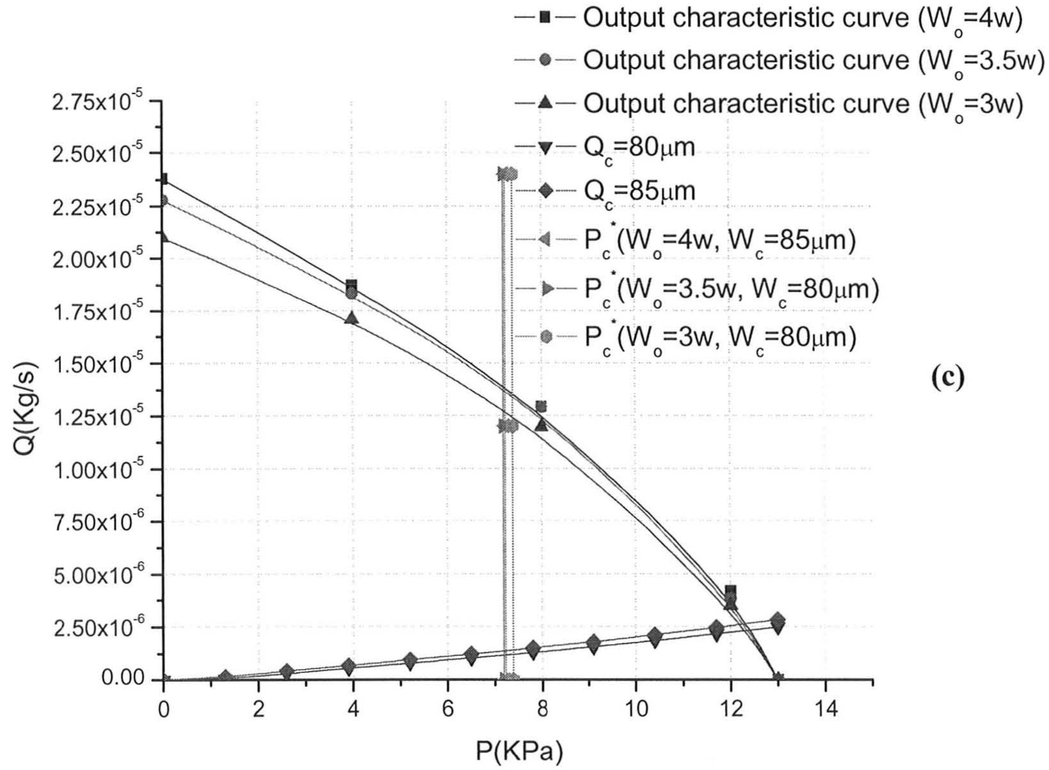

Figure 7-18: (c) Explanation for a point of maximum fan-out with respect to outlet width for L=21W (Re~600 and W$_c$ corresponding to P$_c^*$=P$_{omax}$/2)

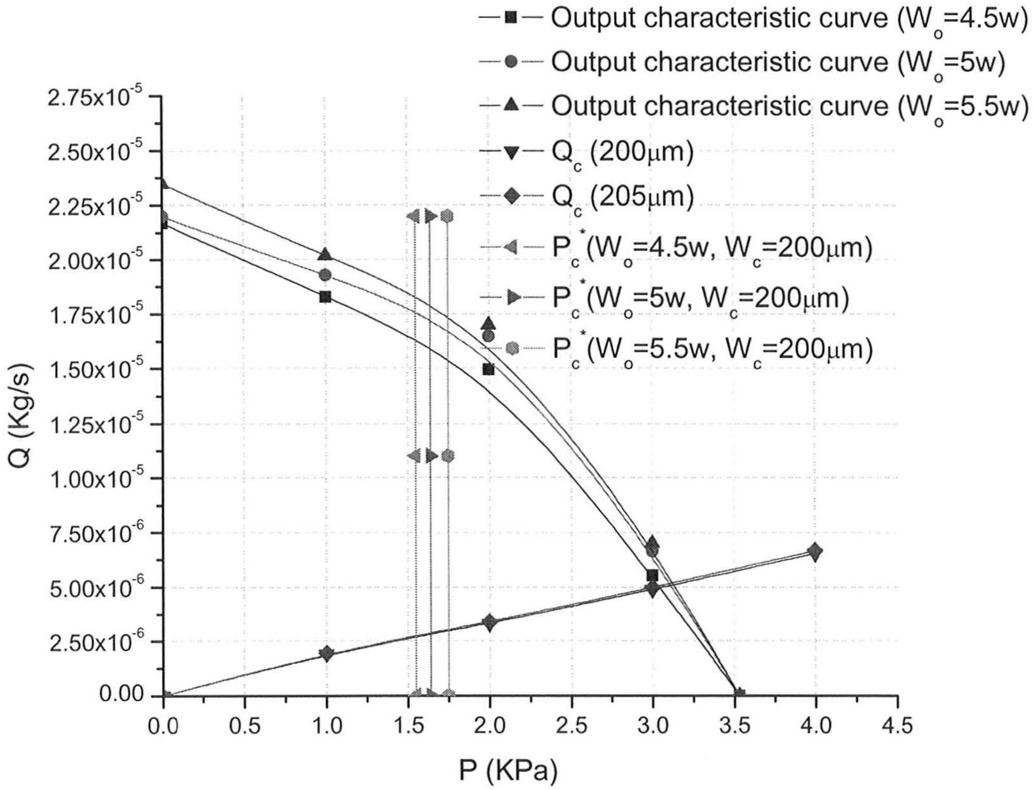

Figure 7-18 (d): Explanation for a point of maximum fan-out with respect to outlet width for L=24W (Re~600 and W$_c$ corresponding to P$_c^*$=P$_{omax}$/2)

7.2.3 LENGTH OF THE DEVICE

The third geometrical parameter that is varied is the length of the device. The control port width (to satisfy Equation 7-1) and the output width are varied for different lengths to plot maximum fan-out vs. output width for different lengths. The plot is shown in Figure 7-19.

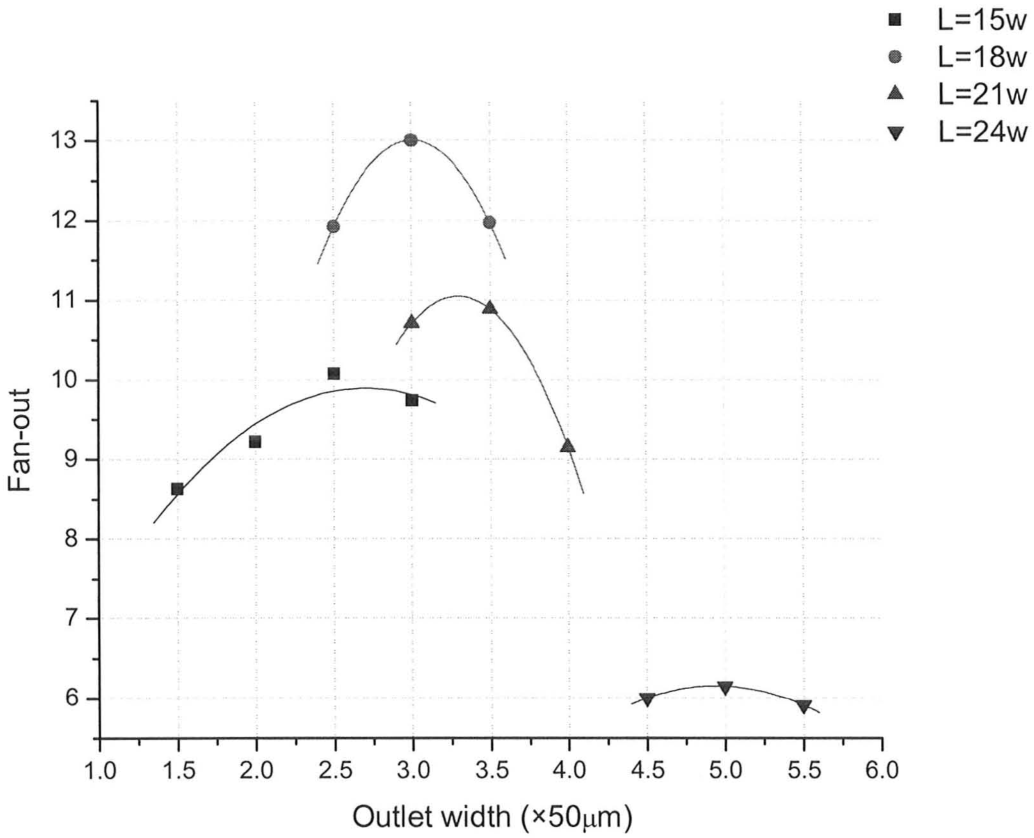

Figure 7-19: Fan-out vs. outlet width for different lengths (Re~600 and W_c satisfying Equation 7-1)

Each of the curves shown in Figure 7-19 were fitted to a parabola. The peak values of the fitted parabola are called W_o^*. The output width corresponding to maximum fan-out (W_o^*) vs. Length (L) is plotted in Figure 7-20.

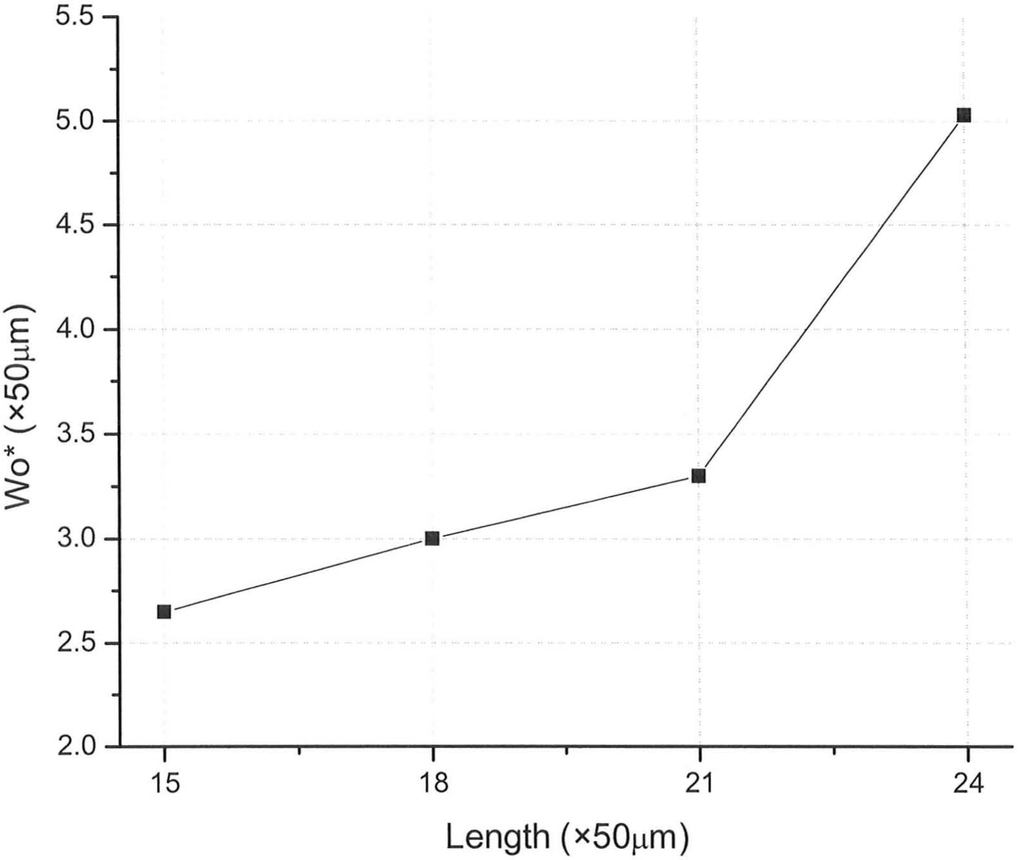

Figure 7-20: Plot of the output width corresponding to maximum fan-out (W_o^*) vs. Length (L)

The no-load mass flow rate through the outlet for varying outlet widths for different lengths and Reynolds number=600 is plotted in Figure 7-21. From Figure 7-21 the outlet widths required to capture 70%, 80% and 90% of the jet are extracted. These outlet widths and W_o^* are plotted in Figure 7-22. A comparison of the outlet widths required to capture different percentages of the supply jet with W_o^* shows that W_o^* is the outlet width which corresponds to capturing ~90% of the supply jet. Thus in the future if a device has to be optimized for its fan-out with respect to the outlet width for a chosen length, we just have to find the outlet width which corresponds to capturing 90% of the supply jet. In other words a new design rule has been established that greatly simplifies the simulation space.

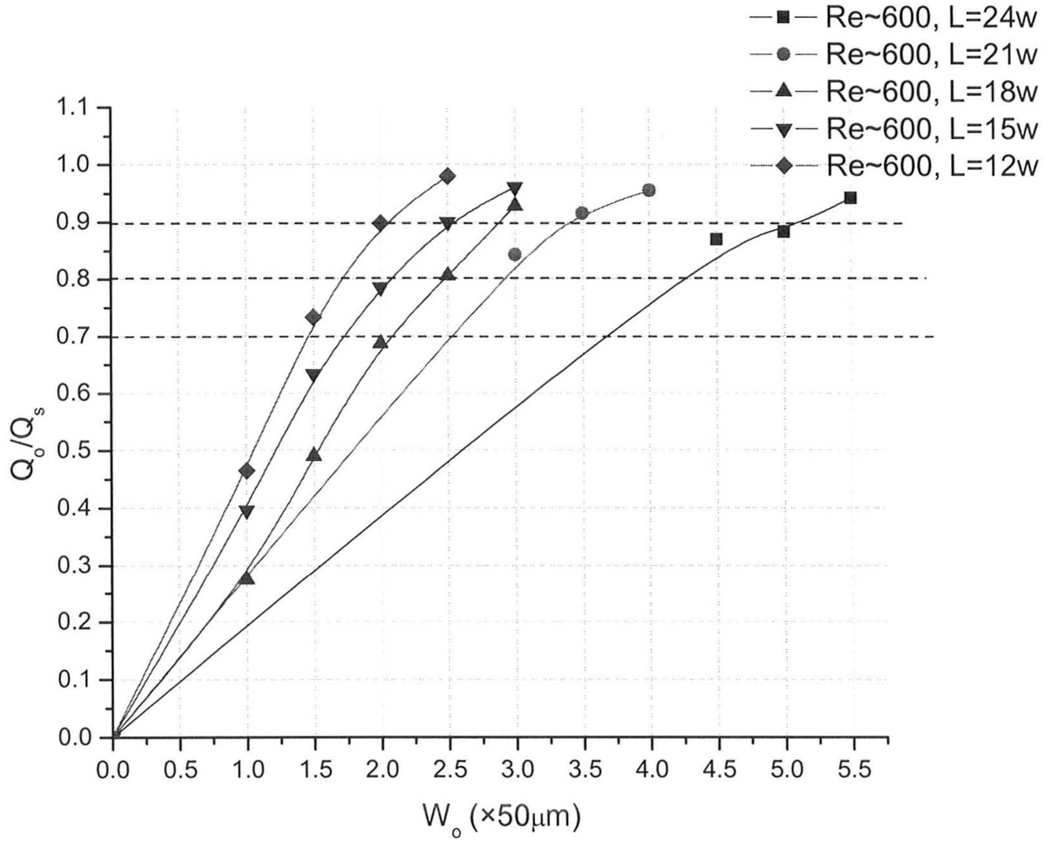

Figure 7-21: Plot of no-load mass flow rate through the outlet for varying outlet width for different lengths and Reynolds number~600

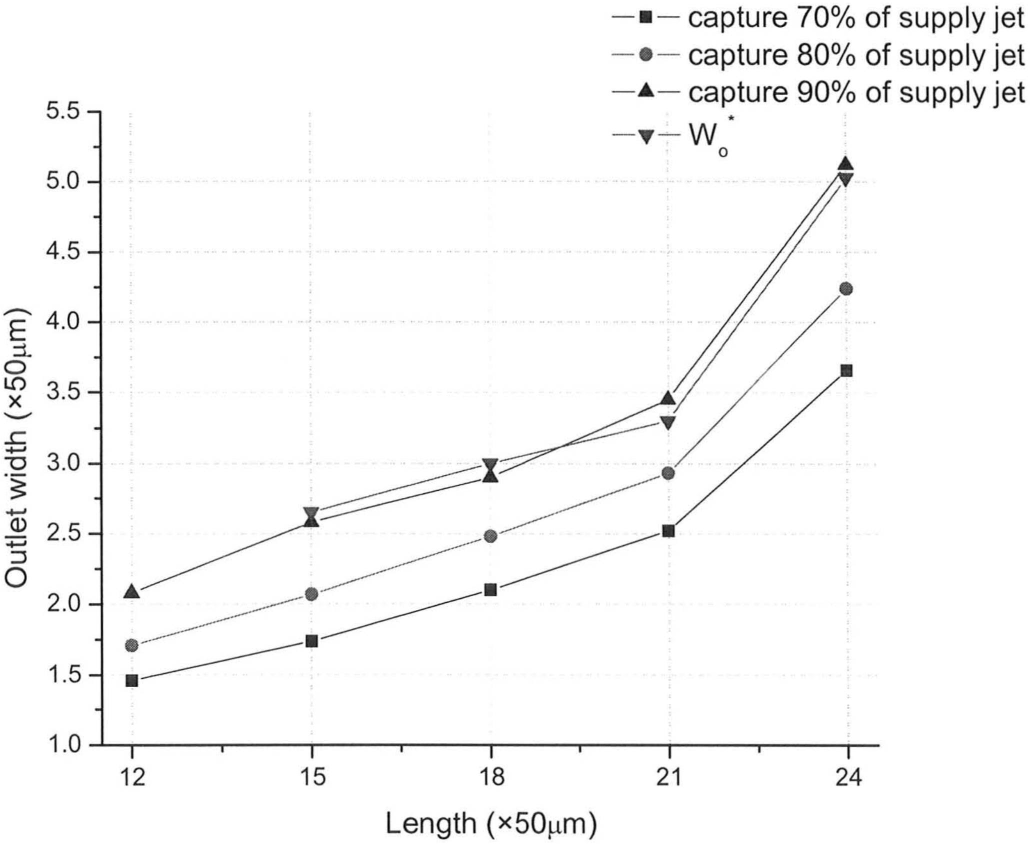

Figure 7-22: Outlet width to capture ~90% of the supply jet for different lengths and Reynolds number~600

The maximum fan-out vs. length is plotted in Figure 7-23. The maximum fan-out is observed at L=18.5w. The optimized device has a fan-out of ~12.7 (extracted from Figure 7-23).

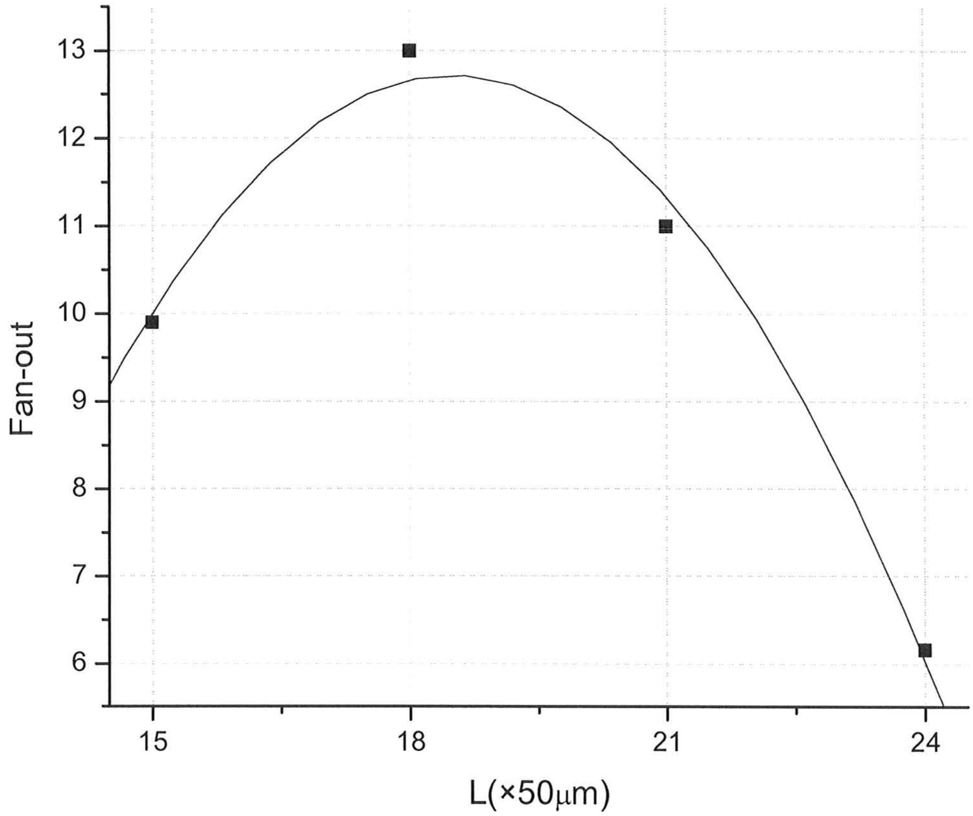

Figure 7-23: Maximum fan-out vs. length (Re~600)

The predicted angle of deflection (tan θ) to turn the device from ON to OFF can be calculated by using Equation 3-6 for a chosen geometry and Reynolds number. For example if P_c=8KPa (to satisfy Equation 7-1 as P_{omax}=16KPa for L=18w), P_{supply}=20KPa, u_{supply}=10m/s, W_c=80μm and W_{supply}=50μm for L=18w are substituted into Equation 3-6, tan θ=0.18. In this section of the thesis we have used Equation 3-6 instead of Equation 3-9 to calculate tan θ because $\rho u_{control}^2$ cannot be neglected for $W_{control}$=200μm. To calculate F_{wall}, we evaluated the magnitude of the pressure (in our simulations) near the slant wall and multiply it with the cross-sectional area over which it extends

The actual angle of deflection (tan θ^*) to turn the device from ON to OFF is given as:

$$\tan\theta^* = \frac{W_o^*}{L} \qquad (7\text{-}2)$$

Tan θ^* is shown in Figure 7-24.

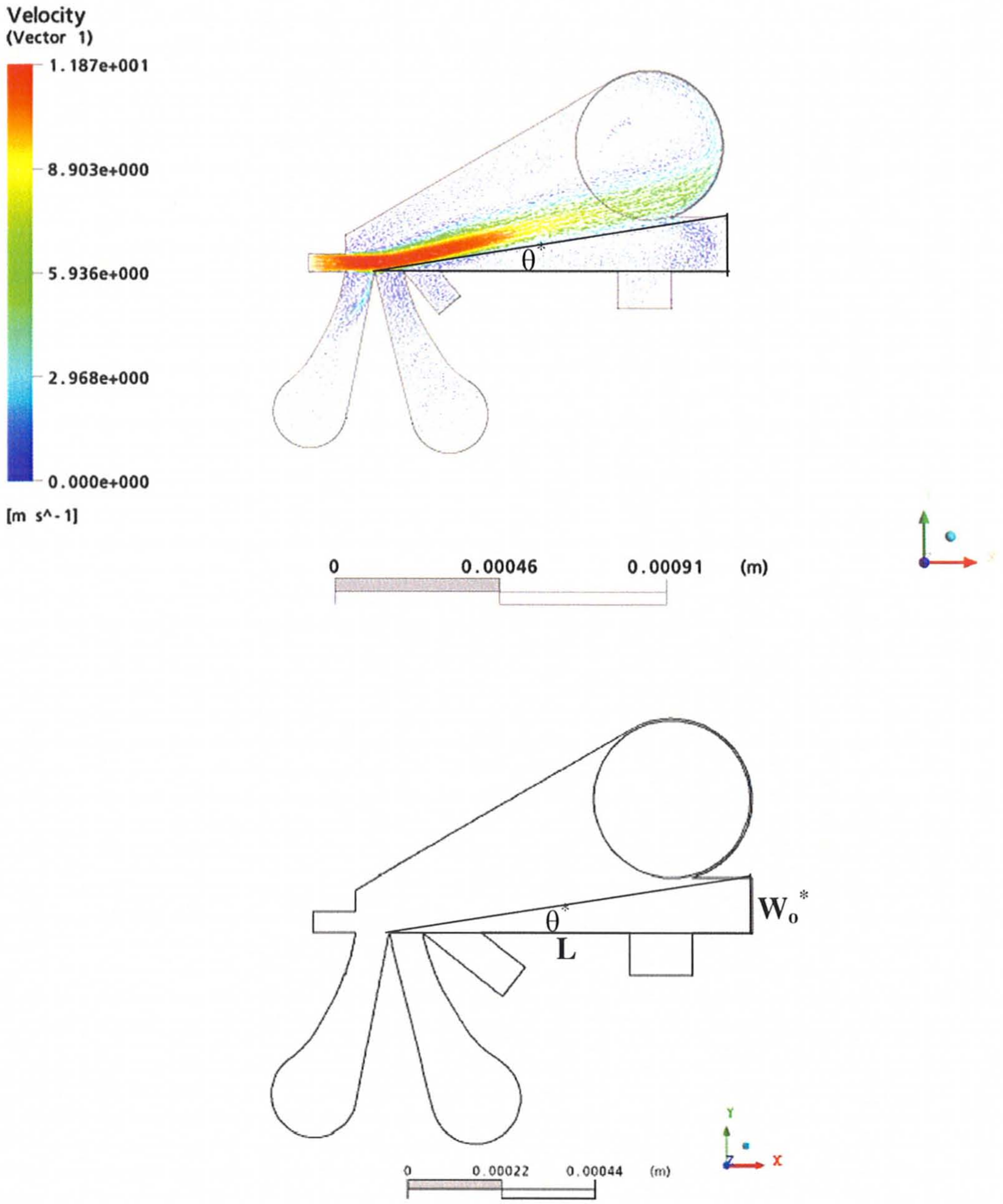

Figure 7-24: The angle (θ^*) by which the jet has to deflected to turn the device from ON to OFF and vice-versa

Length	W_o^*	$\tan\theta^* = \frac{W_o^*}{L}$	$\tan\theta = \frac{(P_c + \rho u_c^2)W_c + F_{wall}/h}{\rho u_{supply}^2 W_{supply}}$
15w	2.5w	0.167	0.1995
18w	3.13w	0.174	0.189
21w	3.63w	0.172	0.179
24w	5.09w	0.212	0.224

Table 7-1: A comparison of tan θ^* and tan θ for different lengths at Re=600

Table 7-1 shows a comparison of tan θ* and tan θ for different lengths at Reynolds number=600. From Table 7-1 we observed that there is a comparatively large difference between the actual angle of deflection (tan θ^*) and the predicted angle of deflection (tan θ) for L=15w. This is because as the length of the device is decreased the size of the circular vent is decreased by design. A decrease in the size of the circular vent implies that the impedance of the circular vent increases. An increased impedance of the circular vent implies a force in the direction opposite to the force due to the applied control pressure. As a result the actual angle of deflection (tan θ^*) is smaller than the predicted angle of deflection (tan θ). Tan θ* and tan θ are however quite close for L=18w to L=24w.

The maximum for fan-out vs. length can be explained as follows: The fan-out increases until L=18.5W and then it begins to drop. This is because as the length of the device is decreased the size of the circular vent is decreased. A decrease in the size of the circular vent implies that the impedance of the circular vent increases as apparent from the difference in the predicted angle of deflection (tan θ) and the actual angle of deflection (tan θ^*) in Table 7-1 for L=15w. As a result it becomes difficult to deflect the jet from the outlet to the circular vent i.e. to turn the device from ON to OFF. Therefore the fan-out decreases. Another possible explanation could be: As the length of the device is increased the control port widths and the vents take up a smaller fraction of the straight bottom wall. As explained in Section 8.5 the bottom wall is important to the device operation, and consequently an increase in the fraction of the available wall-effect results in a higher fan-out. The fan-out drops for longer lengths due to the greater tan θ^* for L=24w compared to L=15w, 18w and 21w. Tan θ^* for L=24w is greater because a jet of fixed Reynolds number begins to spread at a much faster rate as it is allowed to move further and further downstream. Therefore larger outlet width is required to capture ~90% of the supply jet at the outlet. An increased jet spreading in turn also drops the output pressure recovery. Thus to satisfy Equation 7-1 the width of the control port is increased. The control port width satisfying Equation 7-1 is called W_c^*. W_c^* vs. L is plotted in Figure 7-25. As can be seen from Figure 7-25, W_c^* does not vary for L=15 to L=21w because the output pressure recovery does not drop significantly for L=15w to L=21w as shown in Figure 7-26. But as shown in Figure 7-26 the output pressure recovery rapidly drops to 3.35KPa for L=24w due to increased spreading of the supply jet. As a result the control port width has to be increased drastically (as shown in Figure 7-25) to satisfy Equation 7-1. The increased control port width leads to a decrease in the control port impedance which in turn leads to an increase in the flow rate corresponding to the point of intersection between the load line and the output characteristic curve, thereby reducing the fan-out.

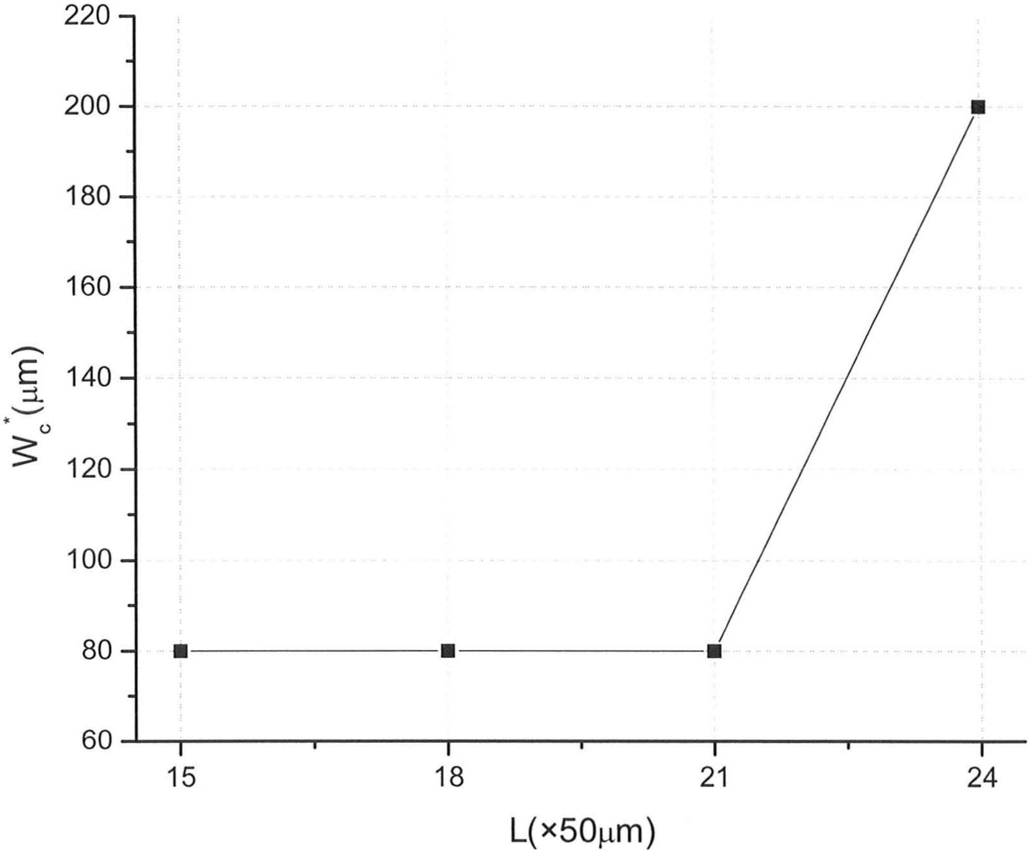

Figure 7-25: A plot of W_c^* for L=15w to L=24w

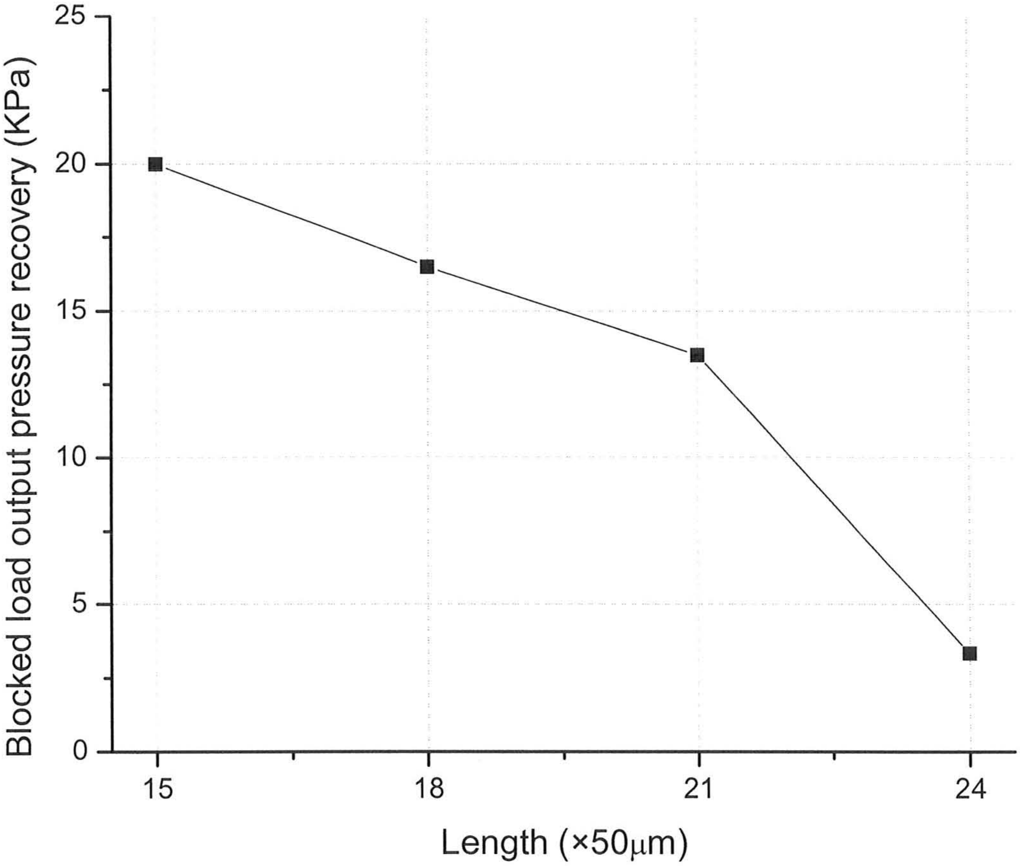

Figure 7-26: A plot of output pressure recovery for L=15w to L=24w

To summarize this section, an optimized design is achieved. We have optimized our device at Re~600. The dimensions of our optimized devices are as follows: Supply nozzle width=50μm, height=50μm, length=18.5w (extracted from Figure 7-23), W_c=80μm=1.6w (extracted from Figure 7-25) and W_o=3.03w (extracted from Figure 7-22) where w is the supply nozzle width. The optimized device has a fan-out of ~12.7 (extracted from Figure 7-23). The transfer functions of our device have a non-linear gain~4.

Our optimized device is different from the device reported by Walker and Trask [8] in Chapter 3. Their experimentally optimized device has a length of 15w, W_c=1.6w and W_o=1.48w. Nothing was mentioned about the non-linear gain of the transfer function. The Reynolds number used by Walker and Trask [8] to optimize their devices was not reported clearly in their paper. Walker and Trask [8] mentioned that for their device the Reynolds number of 300 corresponds to a supply pressure of 2cm of H_2O. And they varied the supply pressure from 3cm to 10cm of H_2O. Thus the Reynolds number was varied from 450 to 1500. But it was not clear what Reynolds number was used to obtain an experimental fan-out of 3-4. We used Re~600 to optimize our devices. The critical dimension of our optimized device is 50μm. The height is 50μm, length is 18.5w and W_o=3.03w. As will be emphasized in Section 7.5 the supply jet spreads as it moves downstream. Thus higher outlet widths are required to capture an appropriate percentage of the supply jets. There might be some differences in the Reynolds number used by Walker and Trask [8] to optimize their devices and the Reynolds number used by us to optimize our devices. In any case, Walker and Trask [8] did not try the higher outlet widths as they increase the length of their device. As a consequence the fan-out of their device begins to drop at a much smaller length.

In the following sections and chapters solutions to the problems mentioned in Chapter 3, deeper insights into the fundamental behavior of the device performance, time-dependent operation of the device, advanced devices and the suitability of our devices for lab-on-a-chip systems are provided.

7.3 TRANSFER CURVES OF A LOADED ELEMENT AND THE DRIVEN ELEMENTS

The transfer curves under blocked load conditions were previously plotted. However, as the element is loaded some of the pressure head has to be converted to the flow head to drive the next-stage gates. In other words, the output pressure recovery of the loaded element decreases. Thus it is important to check the transfer curves of the driven elements when the driving element is loaded. It is also worthwhile to observe the shift in P_c^* and the broadening of the transfer curves of the loaded element. Because of limited computation resources, it was impossible to load an element with 12 real devices. Therefore the element was loaded with dummy loads. The element was also loaded with 3 real devices to check the validity of assumptions made by using dummy loads.

The input impedance is the load seen by the driving element when it is connected to a similar device in series. Thus to calculate the transfer curves of an element under loaded conditions the input impedance of the device needs to be calculated. It is considered that the input impedance is more a function of the supply jet velocity than the geometry of the control port itself. Therefore Q_c vs. P_c without the supply jet, with a supply jet of Re=300 and with a supply jet of Re=600 are plotted in Figure 7-27. It is observed that the input impedance with a supply jet of Re=600 is highest and without a supply jet is lowest. It is also observed from Figure 7-27 that the input impedance is linear with the supply jet. On the other hand, the input impedance is parabolic without the supply jet. This proves the hypothesis that the input impedance is a stronger function of the supply jet velocity.

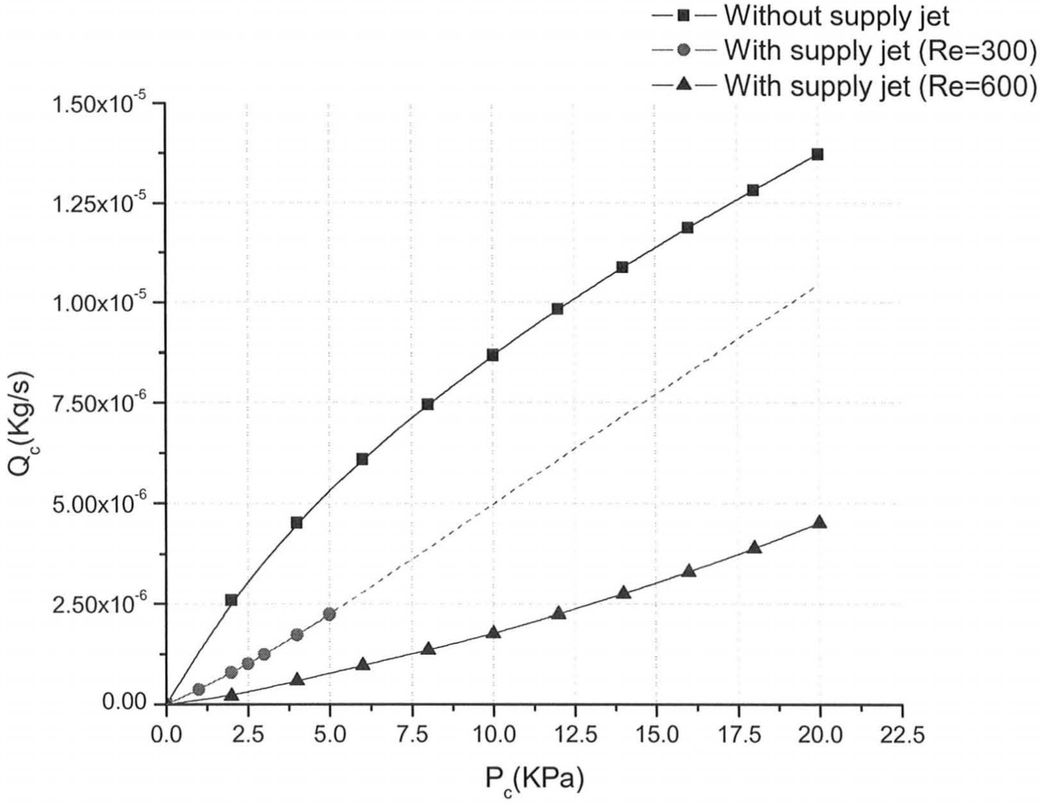

Figure 7-27: Plot of Q_c vs. P_c without the supply jet, with a supply jet of Re~300 and with a supply jet of Re~600 (L=18w, W_o=3.5w and W_c=80µm)

Thus the input impedance cannot be calculated by using the geometrical parameters of the control port. Input impedance (Z_{in}) is defined as:

$$Z_{in} = \frac{P_c}{Q_c} \tag{7-3}$$

where P_c: Input pressure drop and is shown in Figure 7-28.

Q_c: Flow through control port

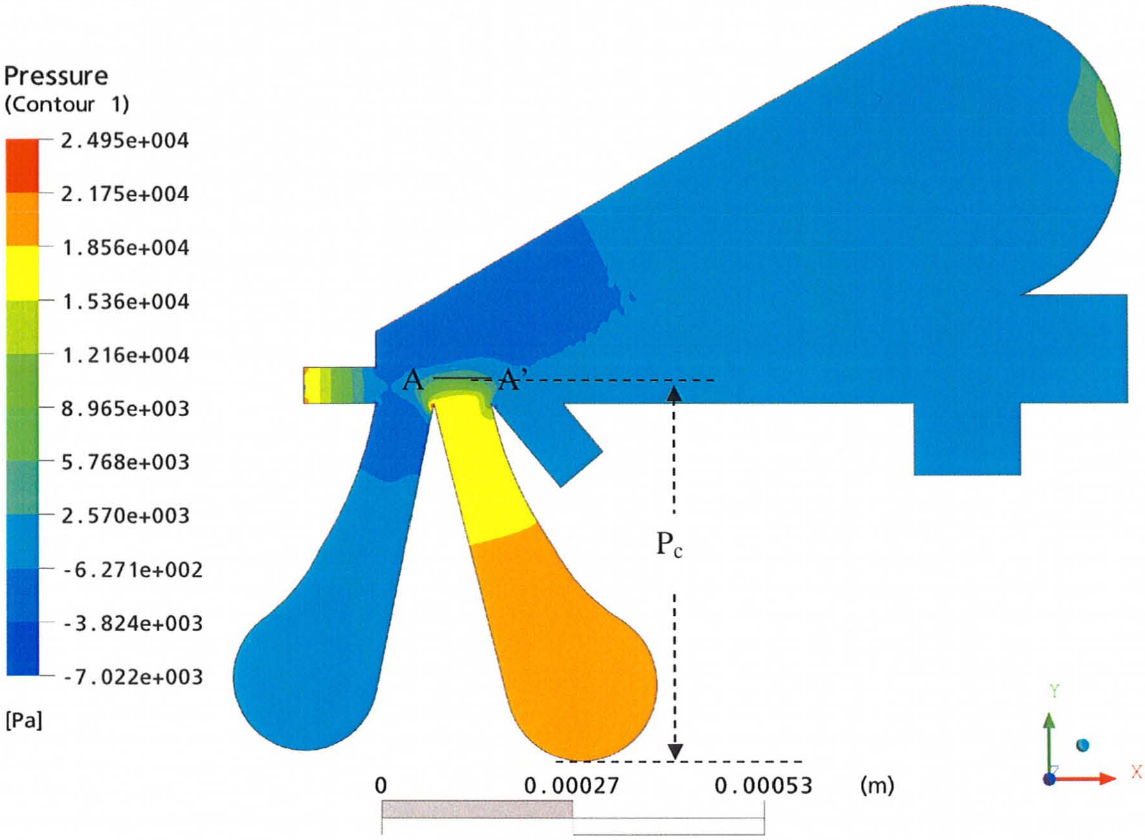

Figure 7-28: An inset showing P_c and plane AA' (L=18w, W_o=3.5w and W_c=80μm)

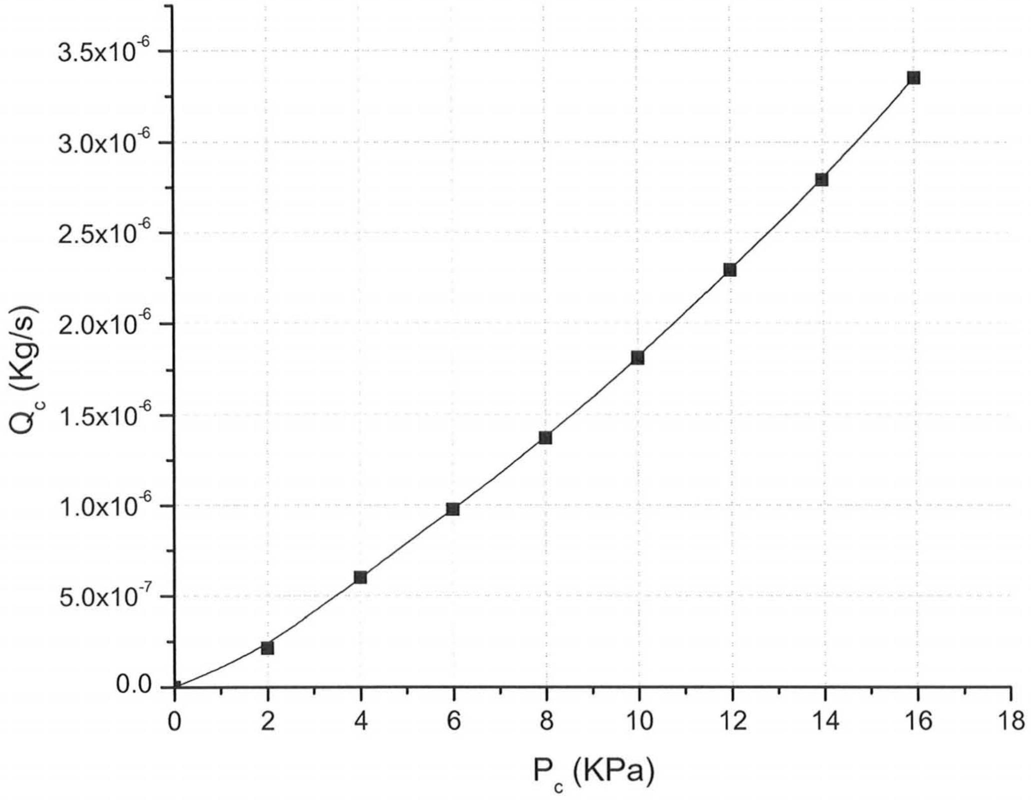

Figure 7-29 (a): Plot of Q_c vs. P_c to obtain the input impedance of the device with a supply jet of Re=600 (L=18w, W_o=3.5w and W_c=80μm)

Q_c vs. P_c was then plotted to obtain the control impedance of the device with a supply jet of Re=600 as shown in Figure 7-29 (a). The derivative of P_c vs. Q_c plot was calculated as shown in Figure 7-29 (b). An average of the values obtained by taking the derivative was calculated to obtain the control port impedance. We find that the average value is 5.02×10^{12} Pa·s/m^3.

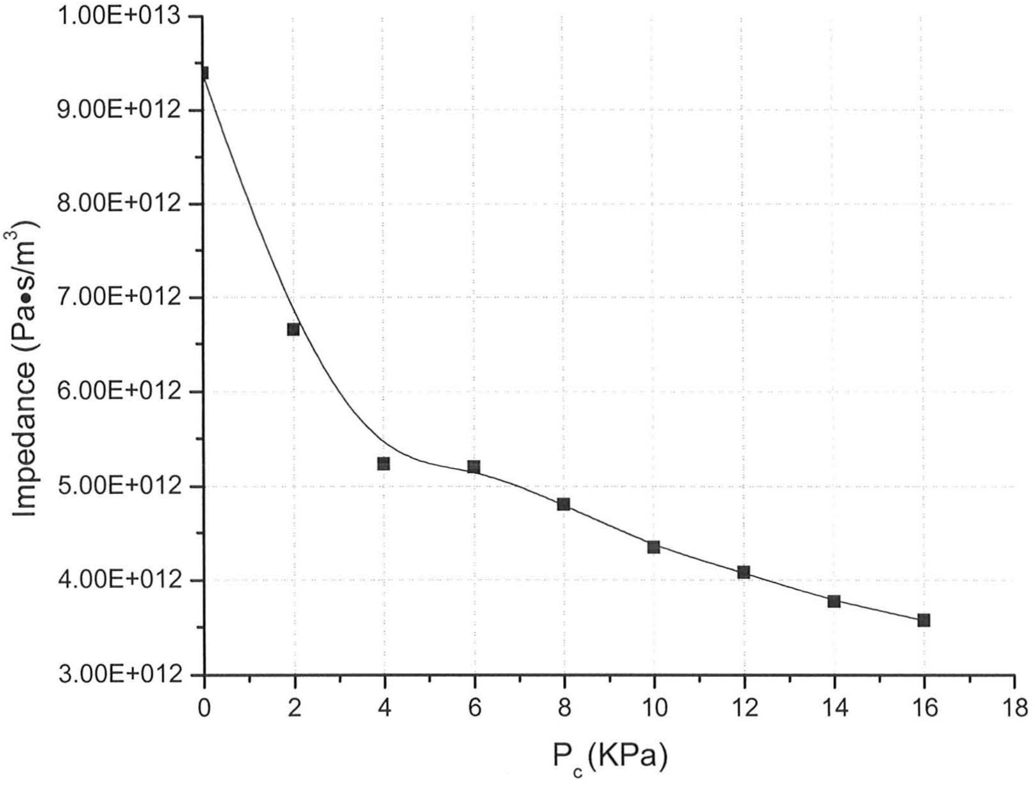

Figure 7-29 (b): Plot of control port impedance vs. P_c to obtain the control impedance of the device with a supply jet of Re=600 (L=18w, W_o=3.5w & W_c=80µm)

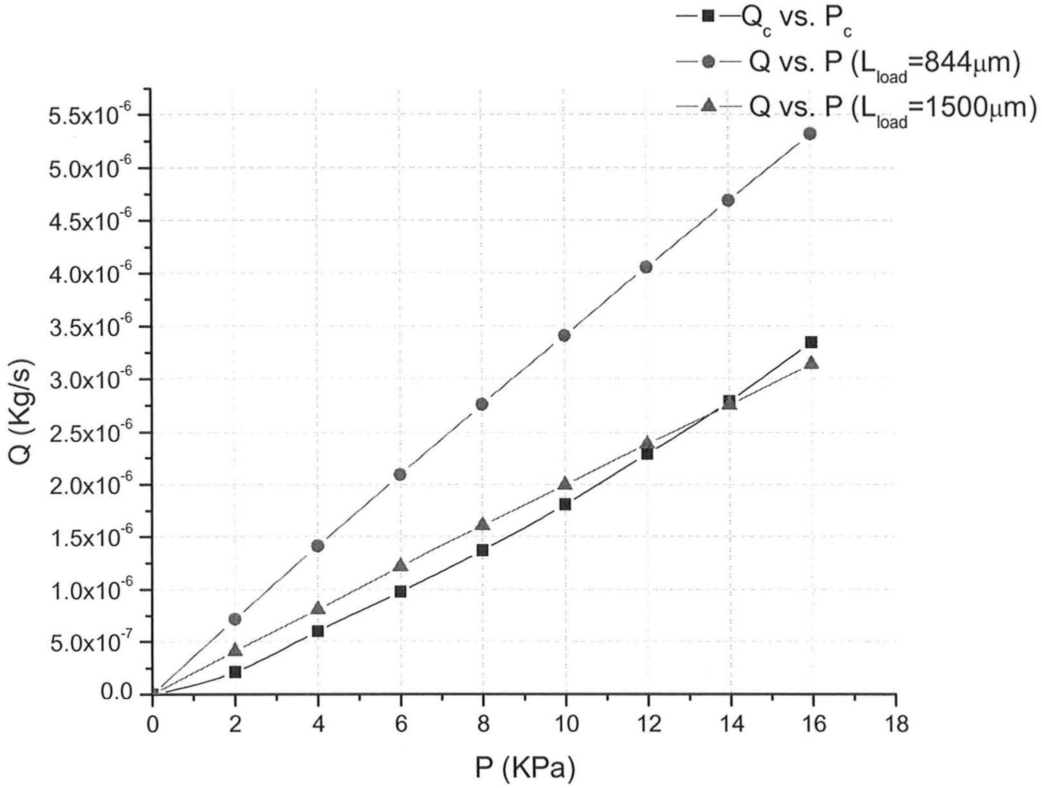

Figure 7-29 (c): Plot comparing the Q vs. P of a square cross-section (50μm×50μm) of different lengths and Qc vs. P_c (L=18w, W_o=3.5w & W_c=80μm and Re~600)

The estimated impedances were geometrically reflected at the outlet of the device as shown in Figure 7-30 (a) and (b). We fixed W_{load}=50μm. Also, the height of the device is 50μm. The impedance of a square cross-sectional geometry is given by using Equation 7-4.

$$Z = \frac{28.43 L_{load} \mu}{h^4} \qquad (7\text{-}4)$$

where Z: estimated control port impedance

μ: dynamic viscosity

h: height of the device (=50μm for our devices)

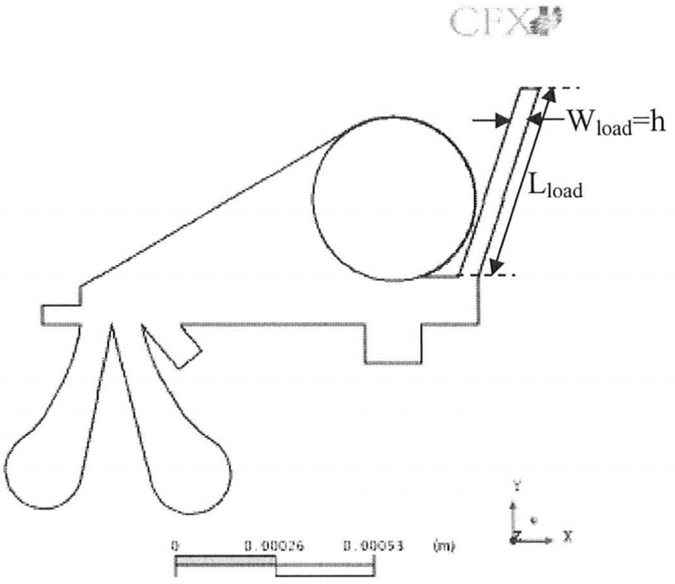

Figure 7-30: (a) Figure showing one dummy load reflected geometrically

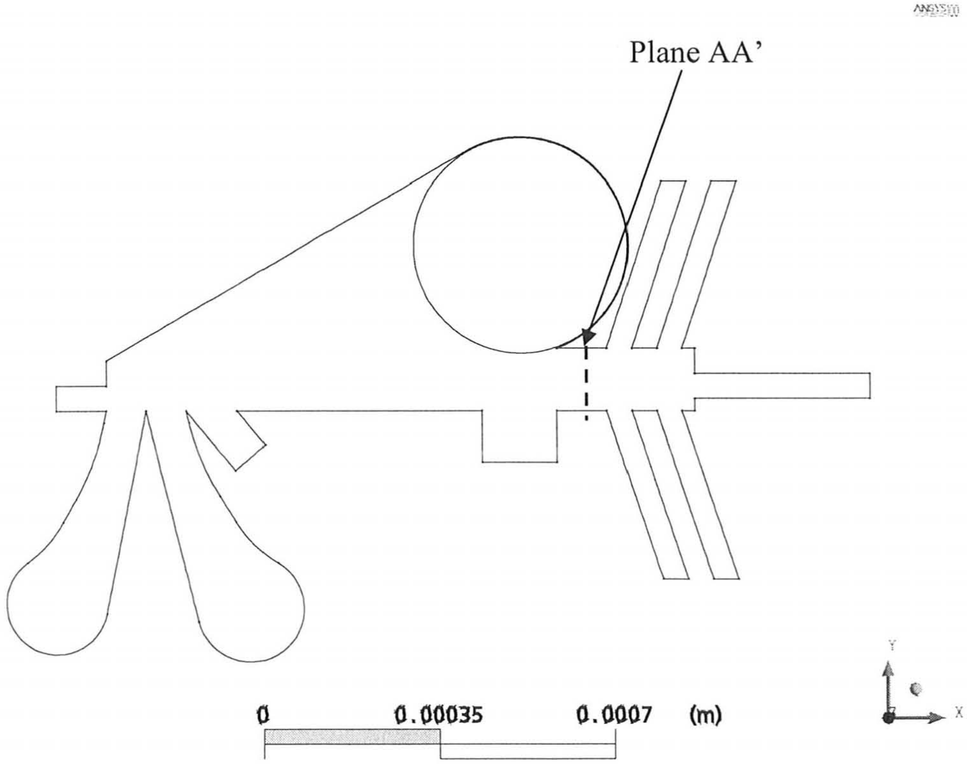

Figure 7-30: (b) Figure showing five dummy loads reflected geometrically

Substituting the values in Equation 7-4 we found L_{load} to be 844μm. However, when we simulated and plotted the flow rate vs. the pressure drop for a pipe (square cross-section: 50μm×50μm) of length 844μm and compared it with Q_c vs. P_c, we found that the impedance of the pipe of length 844μm is smaller by a factor of 2 than the expected value. We find that a constant of 16.49 in Equation 7-4 instead of 28.43, will give the theoretical impedance values in better agreement with the simulated values. The discrepancy in the impedance obtained from the simulations and Equation 7-4 cannot be accounted for at this point of time. We created a dummy load with an impedance of 4.89×10^{12} Pa·s/m^3. (as shown in Figure 7-29 (c)) by using a pipe of length=1500μm.

Fan-out is defined as the number of similar elements in parallel that an element can drive. Thus to load the driving element with 'n' driven elements we can add 'n' elements of width W_{load} (50μm) and length L_{load} (1500μm) to the outlet. For example Figure 7-30 (b) shows five dummy loads reflected geometrically. However we found that if we connect 'n' elements of width W_{load} (50μm) and length L_{load} (1500μm) to the outlet, the resultant impedance is not 'n' times the impedance of a single element. This is due to the presence of the bends between the outlet and the load (as shown in Figure 7-30 (b)). We found that it is more accurate to calculate the loading condition as follows: We evaluated the pressure along AA' (as shown in Figure 7-30 (b)). Let us say that the pressure along AA' is P for a particular loading condition. We then evaluated the flow rate through the plane AA'. We divided this flow rate with Q_c (as shown in Figure 7-29 (a)) corresponding to pressure P, to determine the loading condition.

Figure 7-31 shows a plot of the transfer curves of an element for different loading conditions. It is believed that Point A (as shown in Figure 7-31) is not accurate. It is expected to be below Point B. This is due to the bad solver convergence at Point A. The reason for the bad solver convergence cannot be accounted for at this point of time.

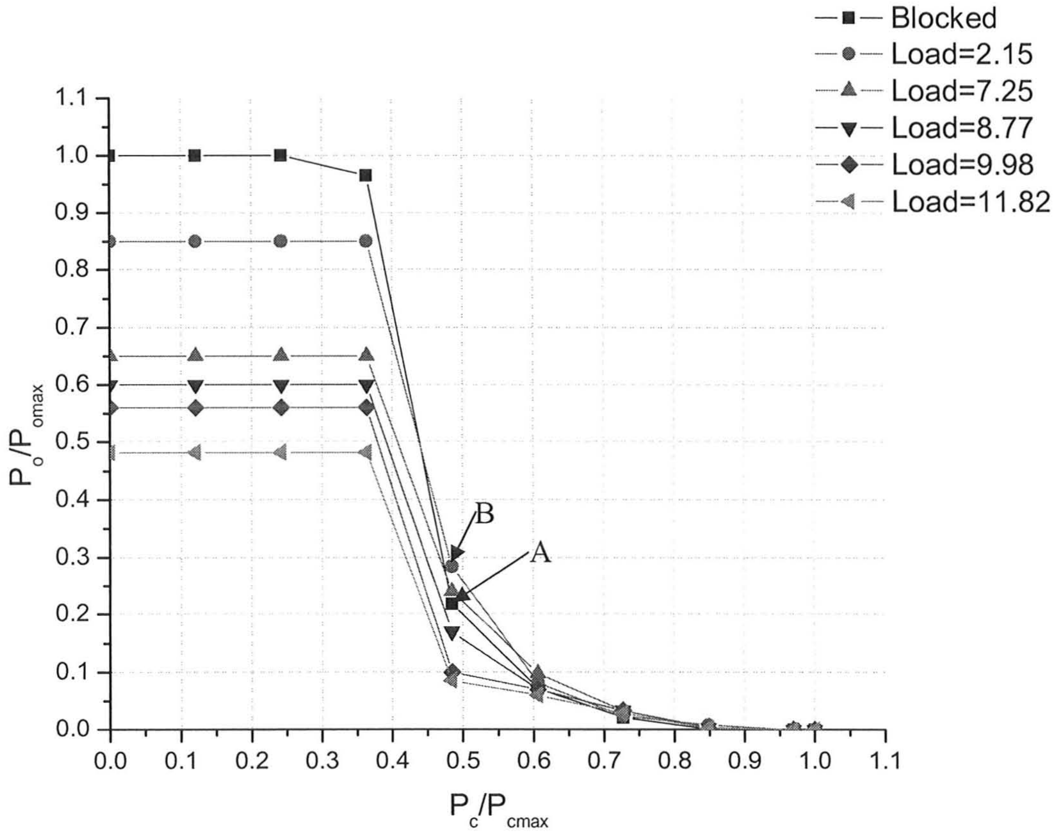

Figure 7-31: Plot of the transfer curve of an element for different loading conditions (L=18w, W_o=3w, W_c=80μm, P_{omax}=P_{cmax}=16.5KPa and Re~600)

This transfer curve was then fed into a transfer curve of a NOR element for blocked load to get the transfer curves of the driven elements. The obtained transfer curves of the driven-elements when the driving-element was loaded with different number of elements, is shown in Figure 7-32. Figure 7-33 shows a plot of the derivative of the transfer curves of the driven-elements when the driving-element was loaded with different number of elements.

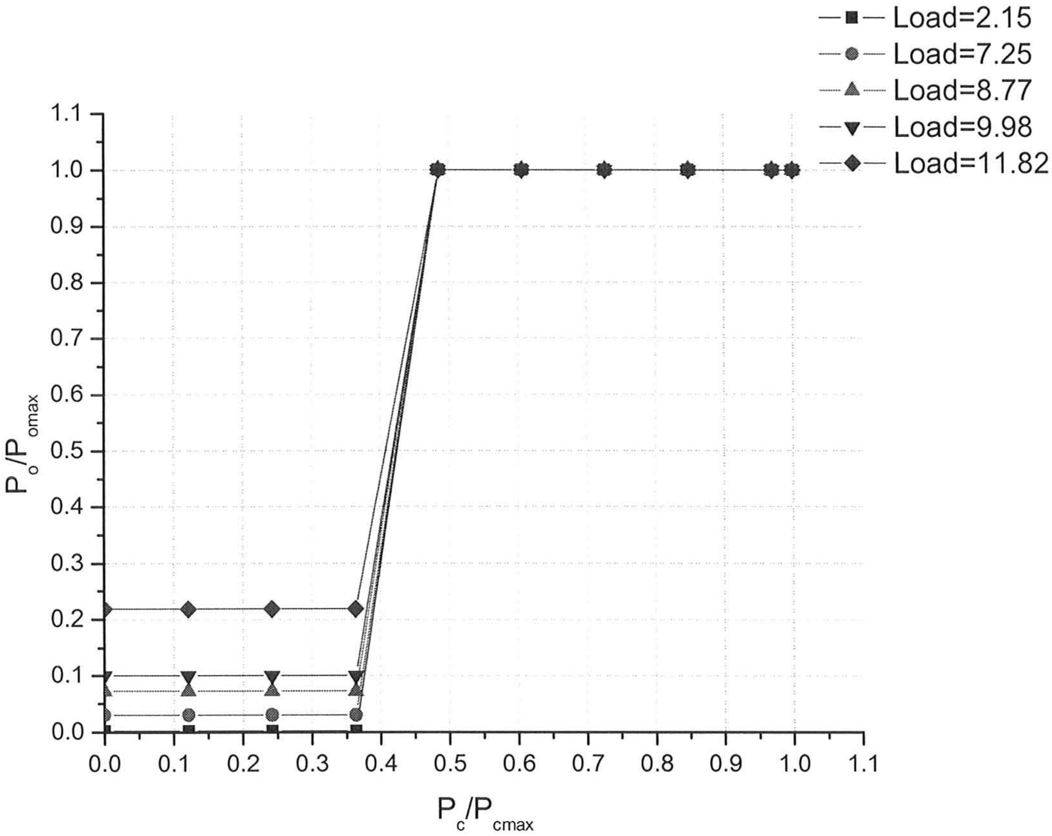

Figure 7-32: Transfer curves of the driven elements when the driving element was loaded with different number of elements (L=18w, W_o=3w, W_c=80μm, P_{omax}=P_{cmax}=16.5KPa and Re~600)

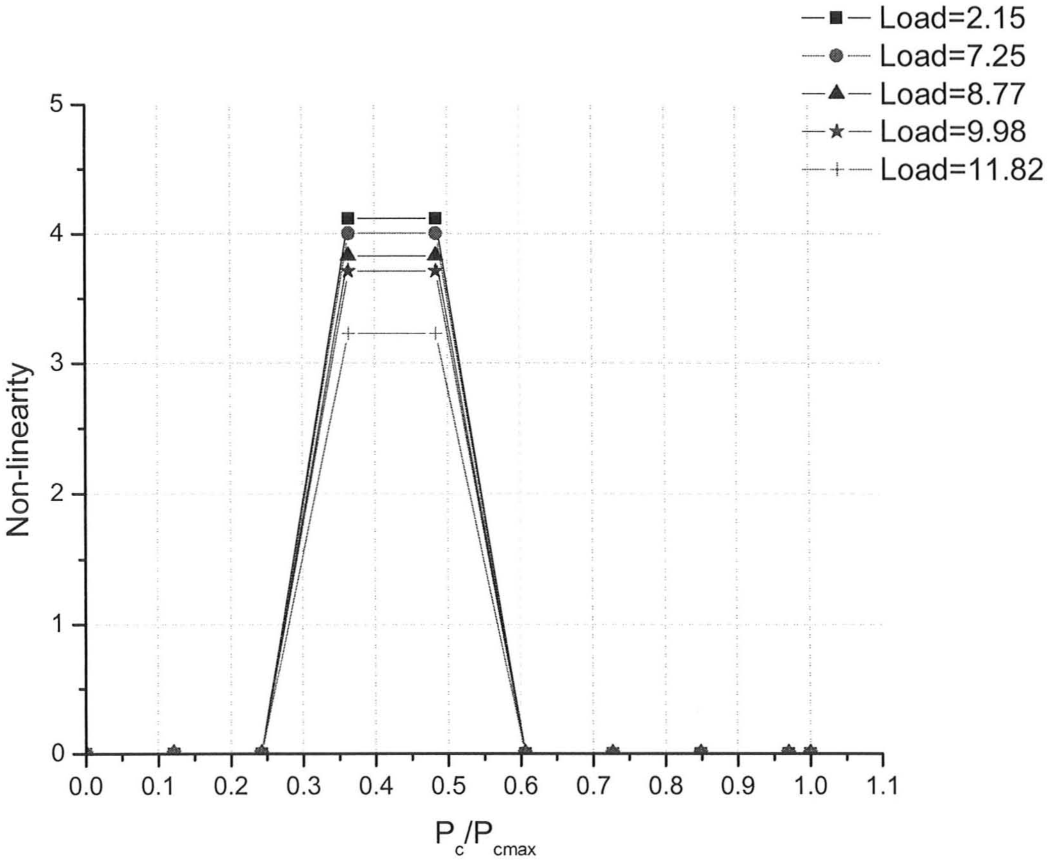

Figure 7-33: Derivative of transfer curves of the driven elements when the driving element was loaded with different number of elements (L=18w, W_o=3w, W_c=80μm, P_{cmax}=16.5KPa and Re~600)

As can be seen from Figure 7-31, Figure 7-32 and Figure 7-33 for load=1 to load=12, the changes in the transfer curve of the driving element are demagnified in the transfer curve of the driven-elements, and therefore the transfer curve of the driven elements does not look very different from the ideal blocked-load case scenario.

As a device is loaded the output pressure recovery of the device begins to drop. This is because some of the pressure head has to be converted to the flow head to drive the next level gates. When the driving element is loaded with 12 elements the pressure recovery drops to 46% of the pressure recovery for the blocked load case. Due to a high non-linearity of the transfer curves of our device, this value regresses to an OFF state after a single iteration. The non-linearity of the resultant transfer curve is also good. Therefore our devices can be loaded with 12 elements without affecting the performance of the next-stage gates.

7.4 CONSTANT VELOCITY VS. CONSTANT PRESSURE SUPPLY

As mentioned in Chapter 3, the performance of the two control ports was different in the design reported by Walker and Trask [8]. In this section of Chapter 7, we will explain how a vent downstream of the second control port solves the problem of asymmetry in the performance of the control ports for constant supply velocity. We will also explain how a vent upstream of the first control port solves the problem of asymmetry in the performance of the control ports for constant supply pressure. A vent upstream of the first control port provides an additional advantage of feedback prevention.

7.4.1 SYMMETRICAL PERFORMANCE OF CONTROL PORTS A AND B FOR CONSTANT SUPPLY VELOCITY

By looking at the flow profiles shown in Figure 3-5, it was thought that a mismatch in the performance of the two control ports can be solved by introducing a vent adjacent to the second control port. This design is shown in Figure 7-34.

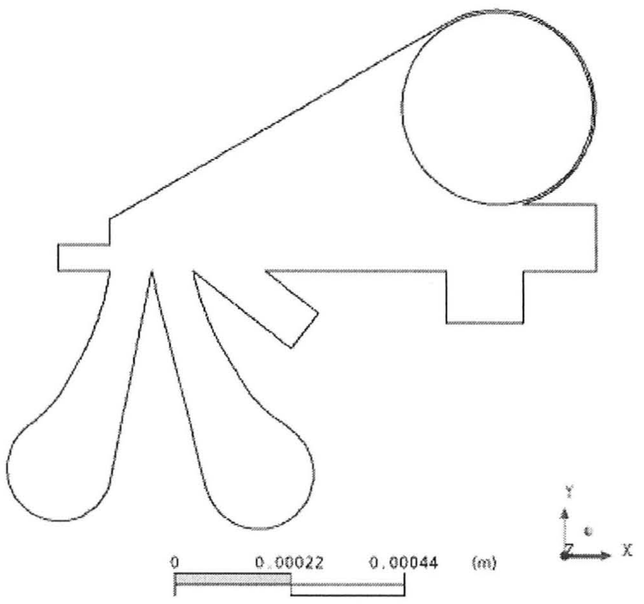

Figure 7-34: A design with a vent adjacent to the second control port

An explanation for the successful functioning of this design is that a vent adjacent to the second control port acts as a source to replenish the entrained molecules as the jet spreads. But the presence of an inclined wall on the other side of the jet results in removing the fluid molecules faster than they are replenished. This results in the formation of a low pressure region near the inclined wall, thereby allowing the second control port to deflect the jet at the same control pressure as that required by the first control port.

The transfer curves and the fan-out for both the first and the second control ports are shown in Figure 7-35 (a) and Figure 7-35 (b). P_c^* is ~7.2-7.6KPa and the device has a fan-out ~9.4 for both control ports.

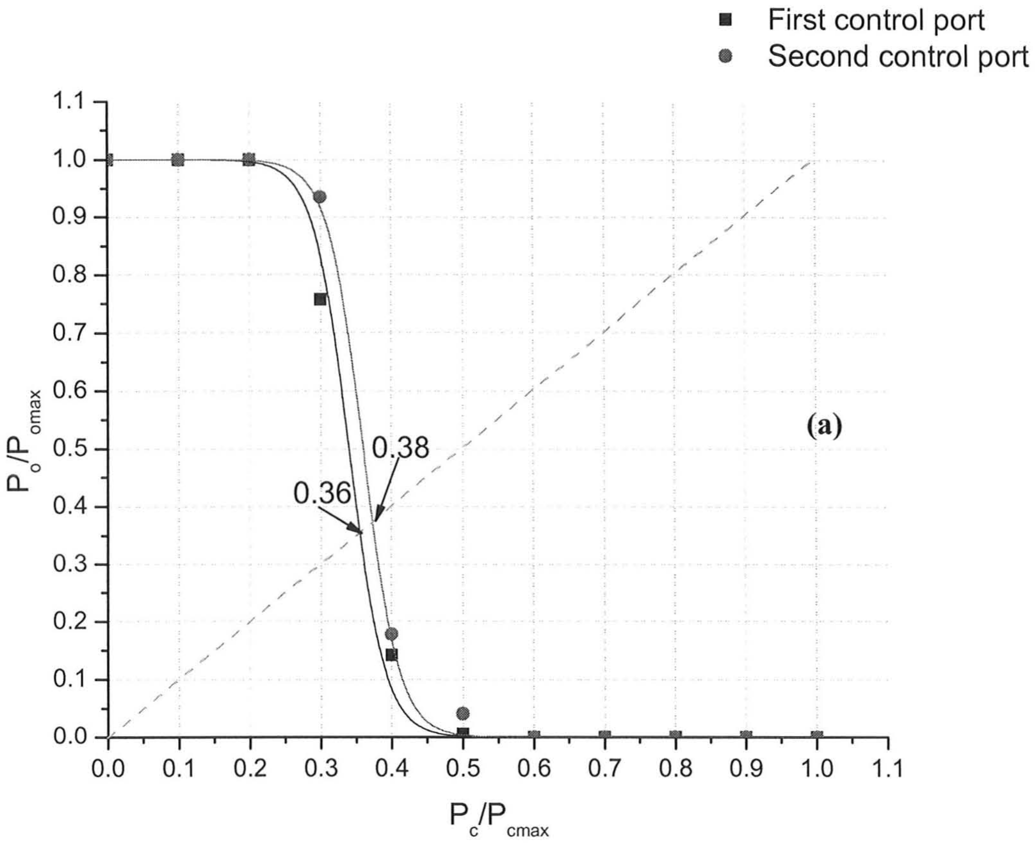

Figure 7-35: (a) Transfer curves for the first and second control ports for the design with a vent downstream of the second control port (L=15w, W_o=1.5w, W_c=100μm, P_{omax}=P_{cmax}=20KPa and Re~600)

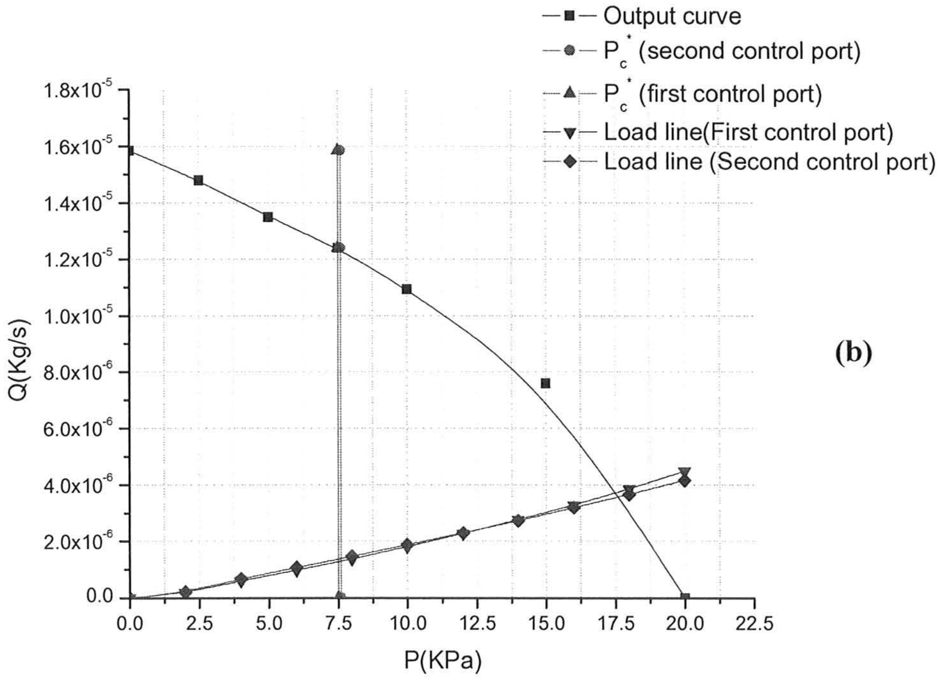

(b)

Figure 7-35: (b) Fan-out for the first and second control ports for the design with a vent adjacent to the second control port (L=15w, W_o=1.5w, W_c=100μm, P_{omax}=P_{cmax}=20KPa and Re~600)

7.4.2 SYMMETRICAL PERFORMANCE OF CONTROL PORTS A AND B FOR CONSTANT SUPPLY PRESSURE

The results presented in Subsection 7.4.1 were simulated by applying constant velocity at the supply. A constant velocity supply is chosen because the performance of our device is sensitive to the Reynolds number of the supply jet as will be explained in Section 7.5. However, the performance of the device by applying a constant pressure at the supply is also checked. Consider our device shown in Figure 7-36.

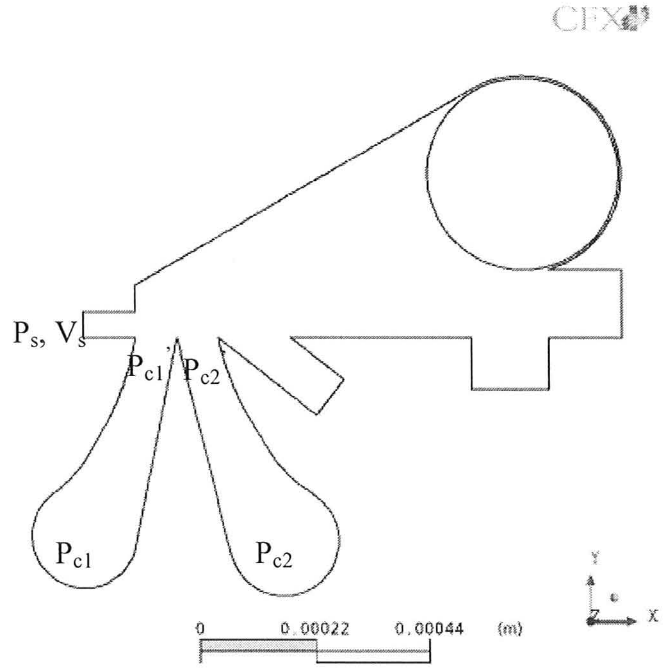

Figure 7-36: Microfluidic NOR

On applying constant pressure, P_s at the supply, an increase of pressure in the first control port, P_{c1} results in a local pressure drop of $P_s - P_{c1}'$. The supply impedance however remains the same due to the fixed supply nozzle geometry. The supply velocity is given as:

$$V_s = \frac{P_s - P_{c1}'}{Z_s} \tag{7-5}$$

where Z_S: supply impedance.

Thus, the supply velocity drops due to an increase of pressure in the first control port.

This is shown in Figure 7-37 (a) and Figure 7-37 (b) where the supply velocity drops from 10m/s to 5.28m/s when pressures of P_{c1}=0KPa and P_{c1}=16KPa are applied to the control port respectively.

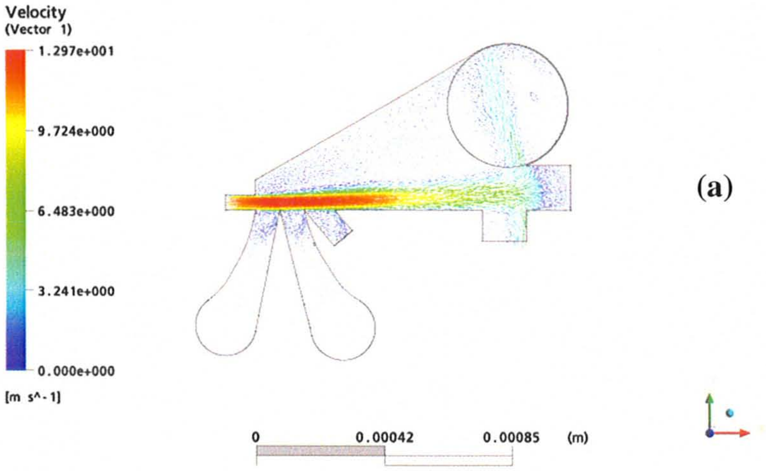

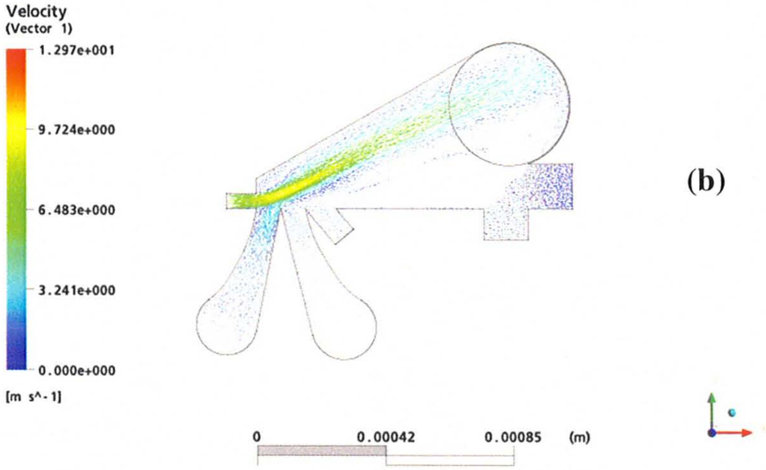

Figure 7-37: Change in supply velocity on applying higher control pressures to the first control port at constant supply pressure (a) P_s=20KPa, P_{c1}=0KPa and V_s=10m/s (b)P_s=20KPa, P_{c1}=16KPa and V_s=5.28m/s (xy plane and z=25μm)

The impedance of the control port is a function of the supply velocity as shown in Figure 7-27, because the supply jet blocks the control port. The higher the supply velocity is, the larger the control port impedance is. A decrease in supply velocity, therefore, results in reducing the impedance of the first control port. Thus in Figure 7-38 (a) the load line of the first control port is above the second control port at constant supply pressure.

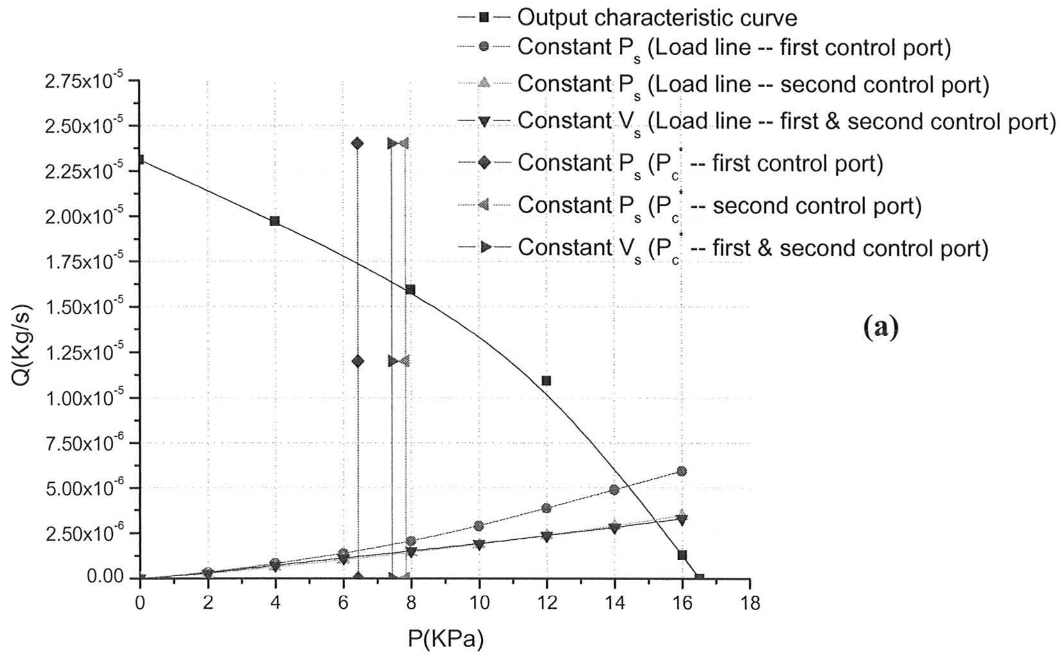

Figure 7-38: (a) Output curve and load line for constant pressure supply and constant velocity of both the control ports (L=18w, W_o=3w, W_c=80μm and Re~600)

Due to flow of information from the control port to the supply, the shape of the transfer curve of the first control port for constant supply pressure is significantly different as shown in Figure 7-38 (b). Also, it is easier to deflect the supply jet of lower velocity. This is reflected in the transfer curve as lower pressure required by the first control port to switch the device from ON to OFF and is shown in Figure 7-38 (b).

To solve the above problems we introduced a vent upstream of the first control port. This vent is labeled as vent A in Figure 7-39 (a).

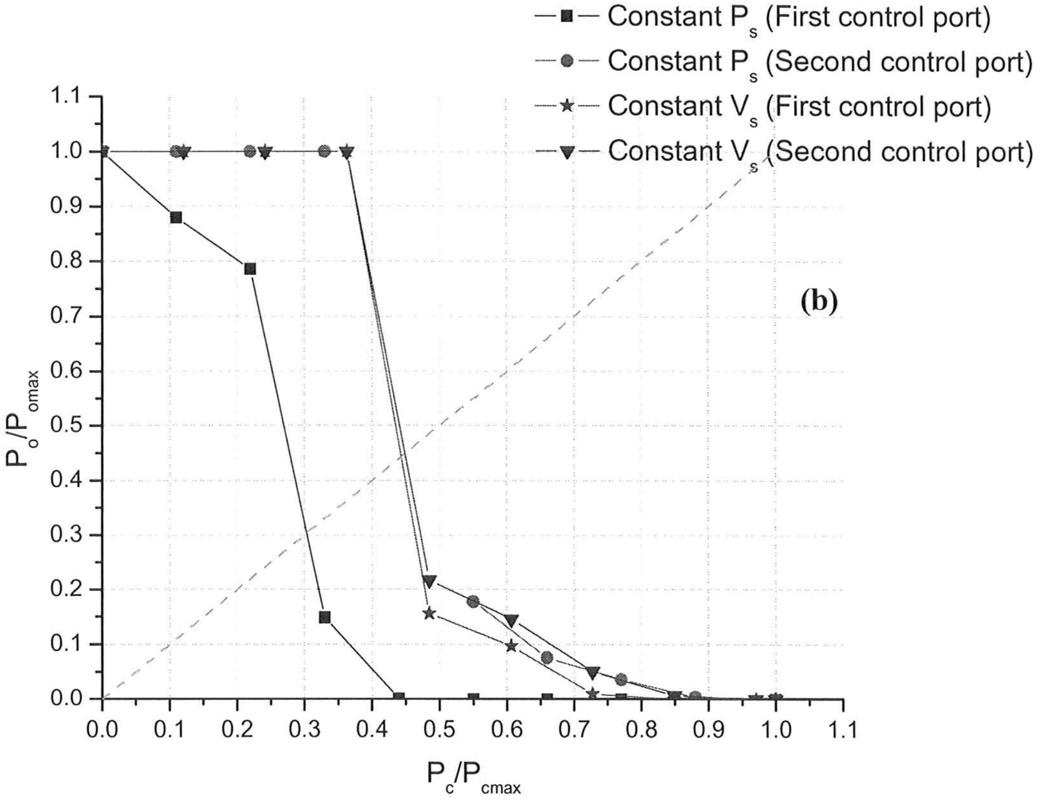

Figure 7-38: (b) Transfer curves for constant pressure supply and constant velocity of both the control ports without vent A ($L=18w$, $W_o=3w$, $W_c=80\mu m$, $P_{omax}=P_{cmax}=16.5KPa$ and Re~600)

Vent A isolates the control ports from the supply nozzle. Thus the Reynolds number of the supply jet at constant pressure does not change on applying pressure at the first control port (as shown in Figure 7-39 (b)). In other words, this geometrical isolation prevents the flow of information in the backward direction. As explained in Chapter 5 this is one of the five crucial requirements to make a computing system.

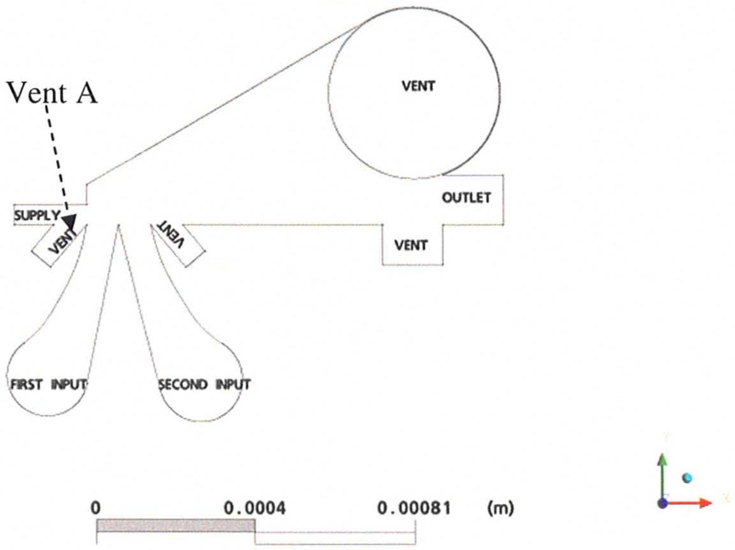

Figure 7-39 (a): Design with a vent upstream of the first control

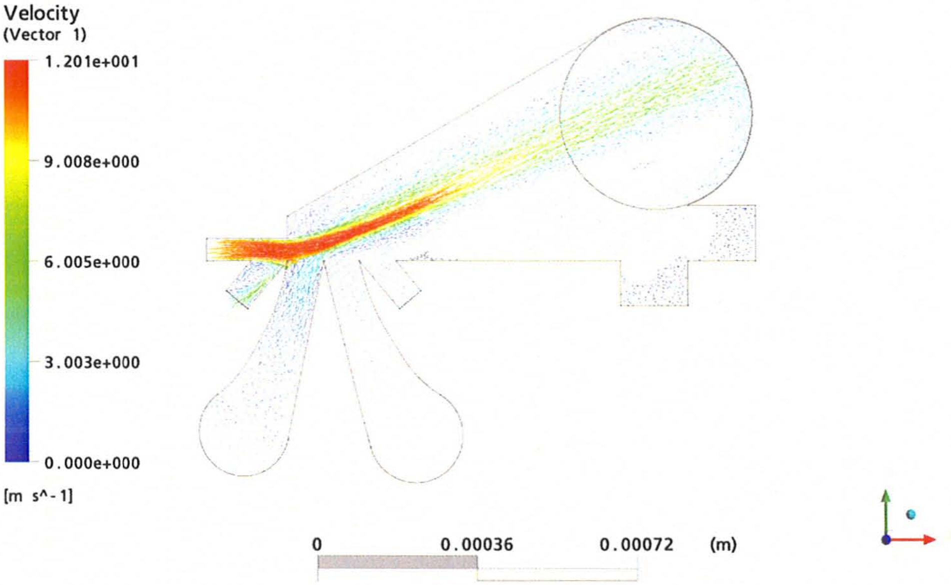

Figure 7-39 (b): Velocity profile for the design with vent A, P_s=20KPa, P_{c1}=16KPa and V_s=10m/s (xy plane and z=25μm)

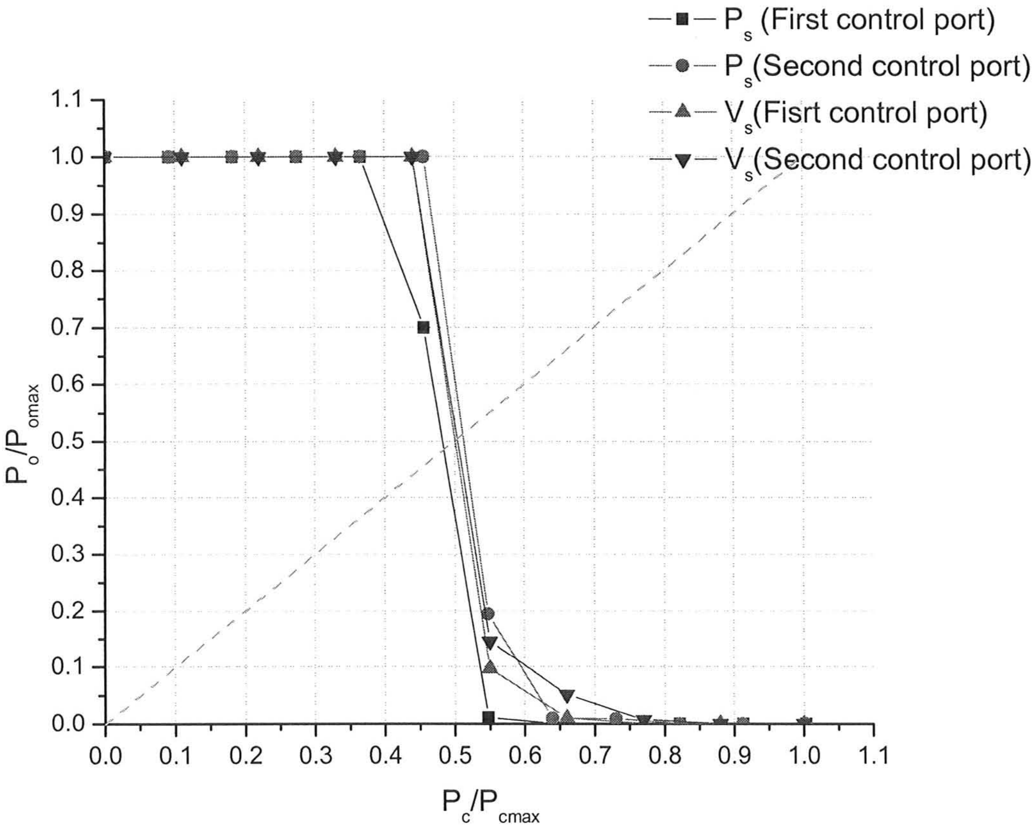

Figure 7-40: Transfer curve of the first and the second control ports with vent A (L=18w, W_o=3w, W_c=80µm, (L=18w, W_o=3w, P_{omax}=P_{cmax}=16.5KPa and Re~600)

Figure 7-40 shows the transfer curve of the both the control ports for the design shown in Figure 7-39 (a). For the design shown in Figure 7-39 (a) a flattened region in the transfer curve for low control pressures even at constant supply pressure is observed.

To conclude Section 7.4, we have achieved a device whose control ports have a symmetrical performance for both constant supply pressure and constant supply velocity.

7.5 REYNOLDS NUMBER SCALING

There are 4 distinct types of jet flow based on Reynolds number [2]:

1. Dissipated laminar flow (Re<300)
2. Laminar jet (300<Re<1000)
3. Laminar-turbulent transition (1000<Re<3000)
4. Turbulent jet (Re>3000)

Our devices need a jet to work. The jet characteristics are studied to examine the spreading of a jet of different Reynolds number as it moves downstream. Figure 7-41 shows a plot of no-load mass flow rate through the outlet for varying outlet width for different lengths and Reynolds number.

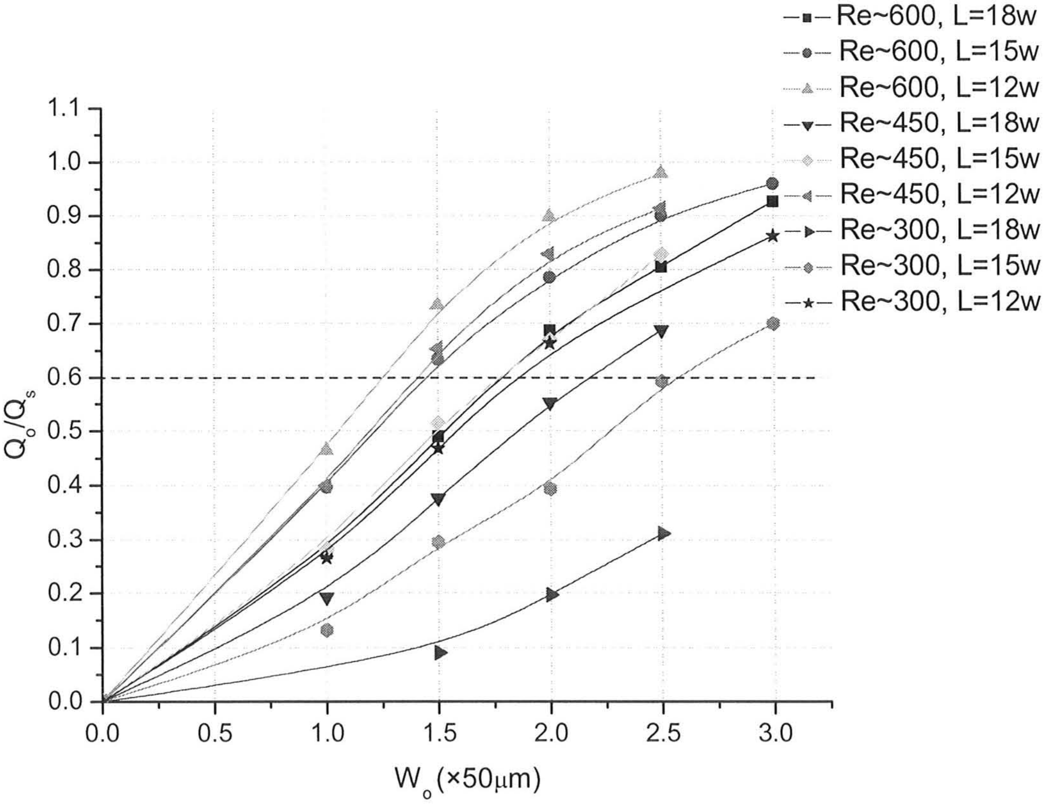

Figure 7-41: Plot of no-load mass flow rate through the outlet for varying outlet width for different lengths and Reynolds number

At Reynolds number 300, the jet spreads a lot. Therefore instead of noting the outlet widths required to capture 90% (as in Section 7.2.3) of the supply jet, the outlet widths required to capture 65% of the jet are noted from Figure 7-41 for different lengths and Reynolds number. The data is plotted as a function of length for different Reynolds number in Figure 7-42.

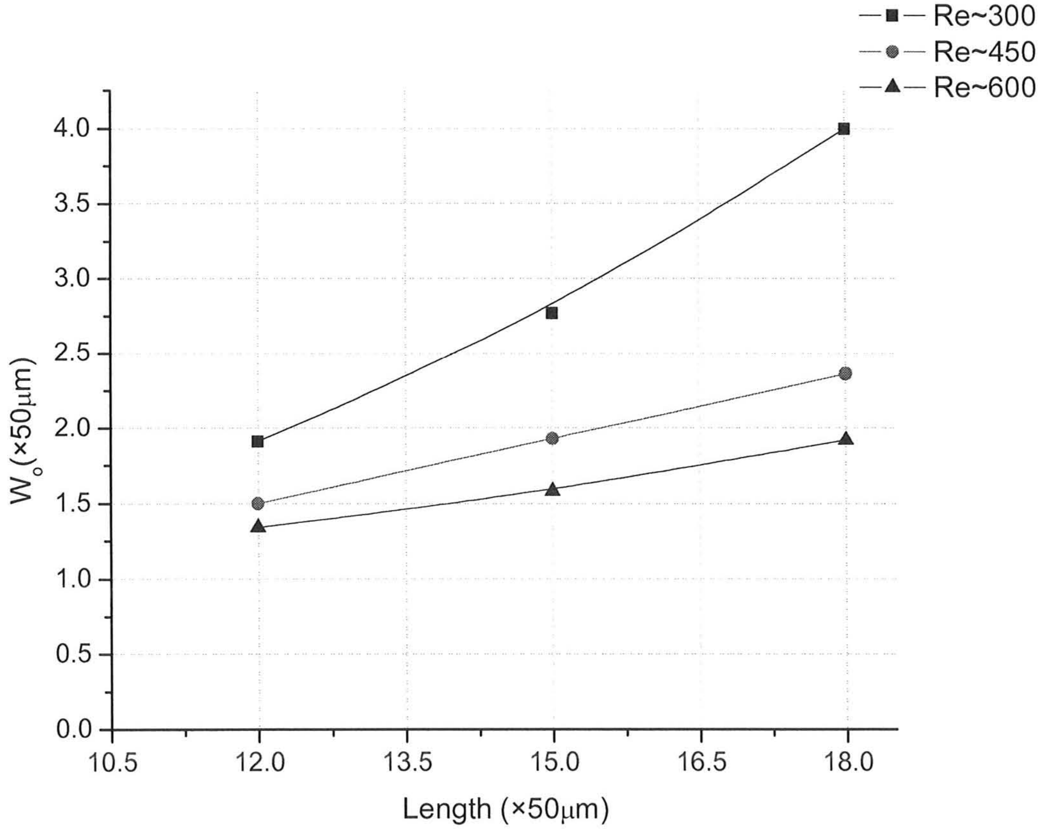

Figure 7-42: Outlet width to capture 65% of the supply jet for different lengths and Reynolds number

For the length range of 12w to 18w, W_o/L rises slowly for the jet of Reynolds number 600. W_o/L also rises slowly for the jet of Reynolds number 450 for the chosen length range. In other words the jets of Reynolds number 450 and 600 spreads linearly with length for the length range of 12w to 18w. But the jet of Reynolds number 300 spreads at a much more rapid rate. The jet of Reynolds number 300 disperses because it does not have the inertia to maintain the flow directionality.

This flow directionality is essential for the jet to flow straight from the supply to the outlet when pressure in both the control ports is low. Jet formation is usually observed in the turbulent regime. This is because at low Reynolds number the viscous forces dominate the inertial forces. As a result the flow gets dispersed to neutralize the pressure differentials. But there is a range of Reynolds number in the laminar regime at which a good jet is observed. This range of Reynolds number is 300-1000 [2]. Our devices are modeled at Re~600 because a laminar jet is desired throughout the length of the device. Laminar jets of lower Reynolds number remain laminar for an appreciable distance after leaving the supply nozzle whereas high Reynolds number jets become turbulent shortly after leaving the nozzle. Laminar jets of higher Reynolds number are also prone to become turbulent due to the disturbances introduced by the impact of flow through the control ports. Turbulent jets are undesirable due to the following reasons: Firstly, the output pressure recovery is independent of Reynolds number in the turbulent regime [2]. A higher supply pressure is required to achieve a jet of higher Reynolds number. Thus it is not energy efficient to use turbulent jets. Secondly, the leakage of the supply jet into the control ports will be much more serious problem when the supply jet is turbulent [2]. Conversely, laminar jets of very low Reynolds number are not appropriate due to low output pressure recovery. As shown in Figure 7-42 a jet of small Reynolds number spreads faster than the jet of higher Reynolds number. The velocity profile of a supply jet of Re~300 and Re~600 for a device of fixed geometry is shown in Figure 7-43 (a) and Figure 7-43 (b) respectively, further emphasizing that a jet of lower Reynolds number spreads faster than a jet of higher Reynolds number.

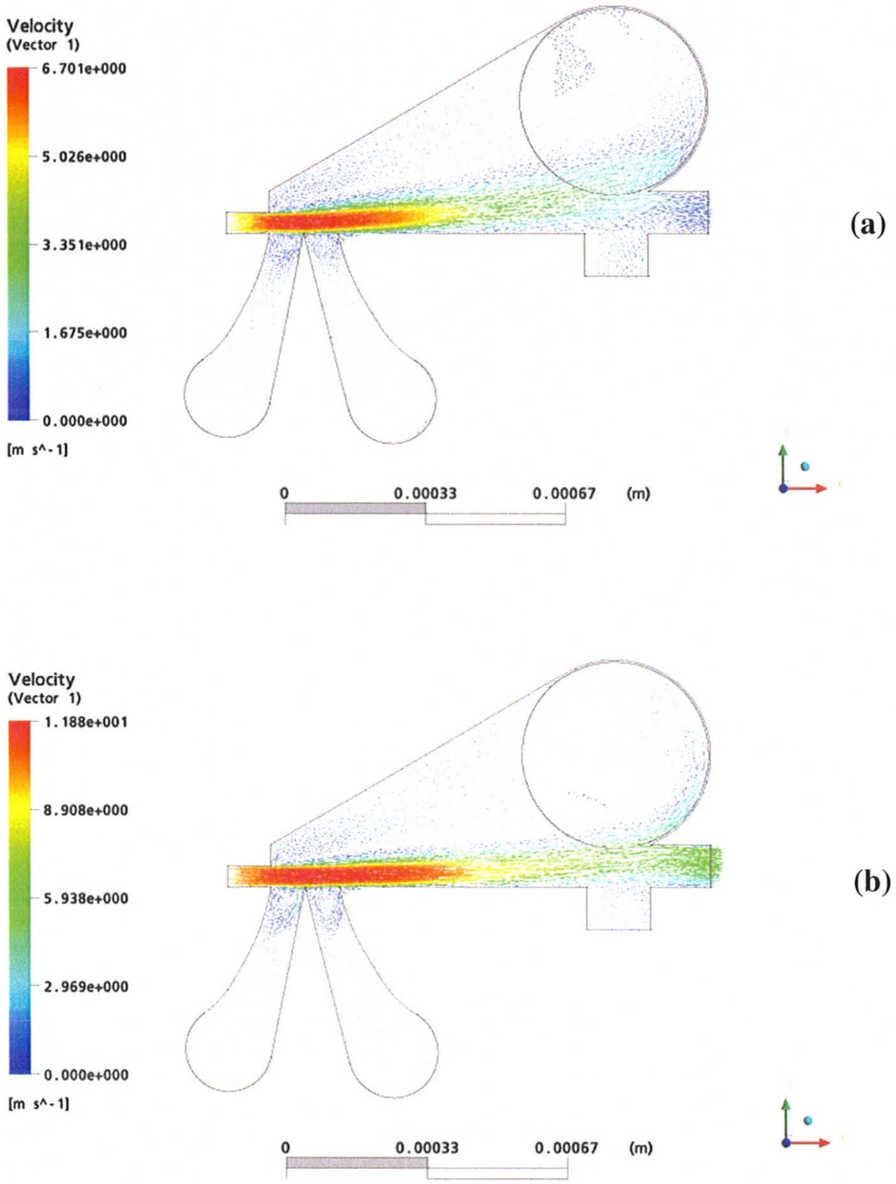

Figure 7-43: Velocity profile of a supply jet of Reynolds number (a) 300 and (b) 600 (xy plane and z=25μm)

The rate at which a jet spreads is a function of Reynolds number in the laminar regime. Therefore, for a fixed geometry the pressure recovery is also a function of Reynolds number in the laminar regime. Pressure recovery is low at lower Reynolds number due to excessive jet spreading as it moves downstream. A low pressure recovery leads to less non-linear transfer curves. For example the transfer curves and the corresponding non-linearity curves at Re~300 and Re~600 are shown in Figure 7-44 (a) and Figure 7-44 (b).

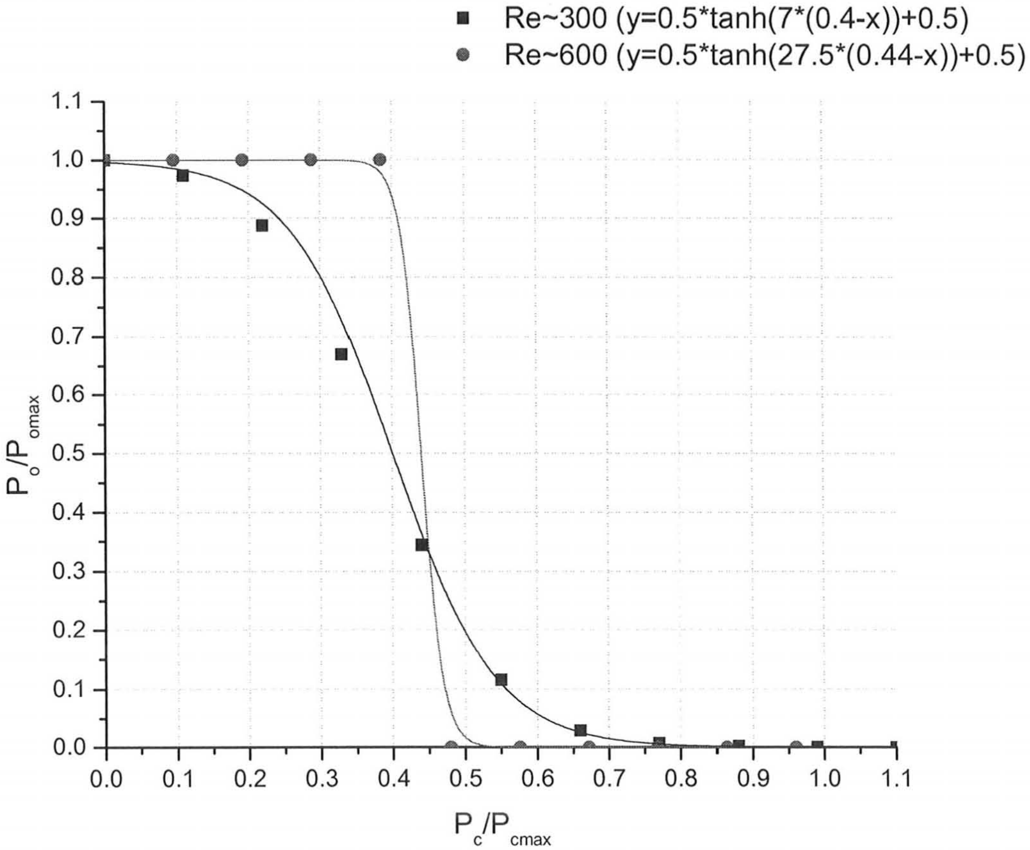

Figure 7-44: (a) Transfer curves at Re~300 and Re~600 (L=12w, W_o=1.5w and W_c=50μm) (Re~300: P_{omax}=P_{cmax}=4.54KPa and Re~600: P_{omax}=P_{cmax}=26KPa)

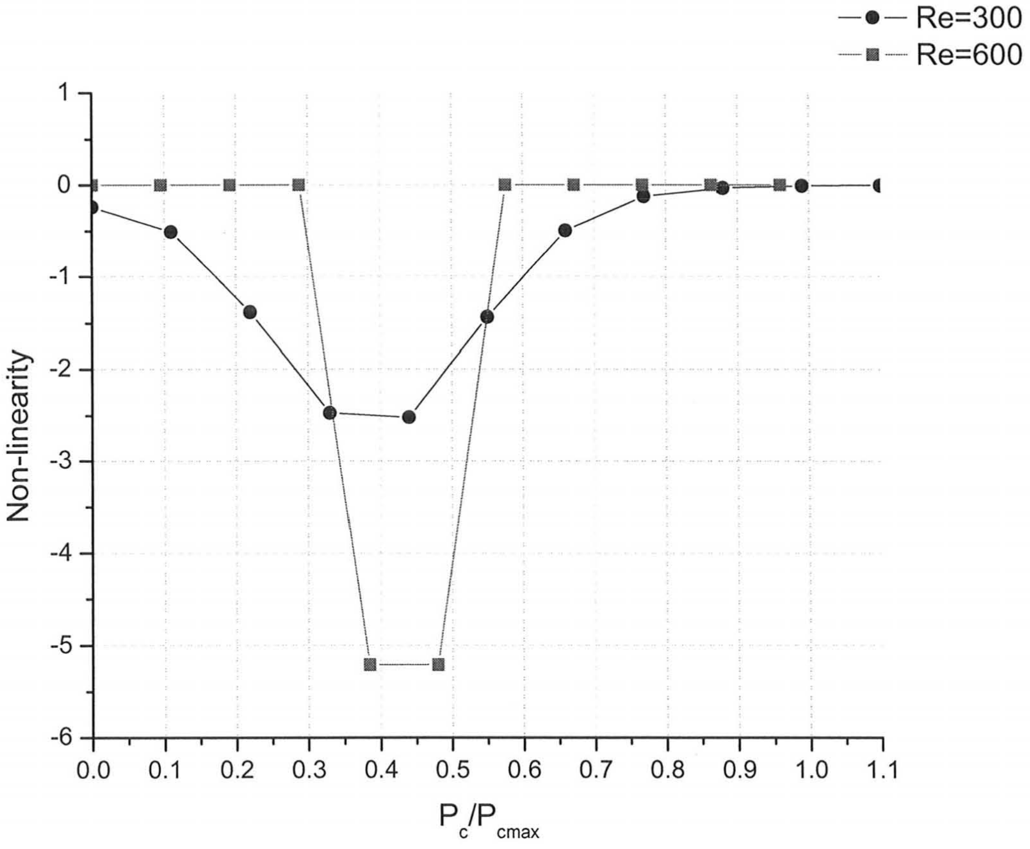

Figure 7-44: (b) The corresponding non-linearity curves at Re~300 and Re~600 (L=12w, W_o=1.5w and W_c=50μm) (Re~300: P_{cmax}=4.54KPa and Re~600: P_{cmax}=26KPa)

However, lower Reynolds number jets can be deflected more easily. It is possible that somewhat improved performance is possible in the range of 300-600. But in this thesis we have only tested the performance of our devices at Reynolds number of 600.

CHAPTER 8 FUNDAMENTAL DEPENDENCIES

8.1 GEOMETRY SCALING

If the geometry of the device is scaled uniformly but the Reynolds number is kept constant, the flow and pressure profiles, the transfer curve, the normalized output curve, the normalized load line and thus the fan-out do not change.

We refer to the device with a critical dimension of 50μm as the base geometry. The base geometry is then scaled by a factor of 10 and 0.1. The transfer curve, the normalized output curve, the normalized input curve and the fan-out of the scaled geometries are compared with the base geometry. Results shown in Figure 8-1 (a) and (b) clearly indicates that the performance of the device in terms of the transfer curve and the fan-out is independent of geometry scaling at constant Reynolds number. The quantities P_{omax}, P_{cmax}, Q_{max}, supply velocity, V_s for the base geometry, 10×base geometry and 0.1×base geometry are shown in Table 8-1.

	P_{omax} (KPa)	P_{cmax} (KPa)	Q_{max} (Kg/s)	V_s (m/s)
10×base geometry	0.02	0.02	1.98×10^{-4}	1
base geometry	20	20	1.98×10^{-5}	10
0.1×base geometry	2000	2000	1.98×10^{-6}	100

Table 8-1: Quantities P_{omax}, P_{cmax}, Q_{max} and supply velocity, V_s for the base geometry, 10×base geometry and 0.1×base geometry

Physical Quantity	Scaling at constant Reynolds number
Dimension	[L]
Area	$[L]^2$
Velocity	$[L]^{-1}$
Flow rate	[L]
Pressure	$[L]^{-2}$

Table 8-2: Scaling of the common physical quantities with geometry at constant Reynolds number

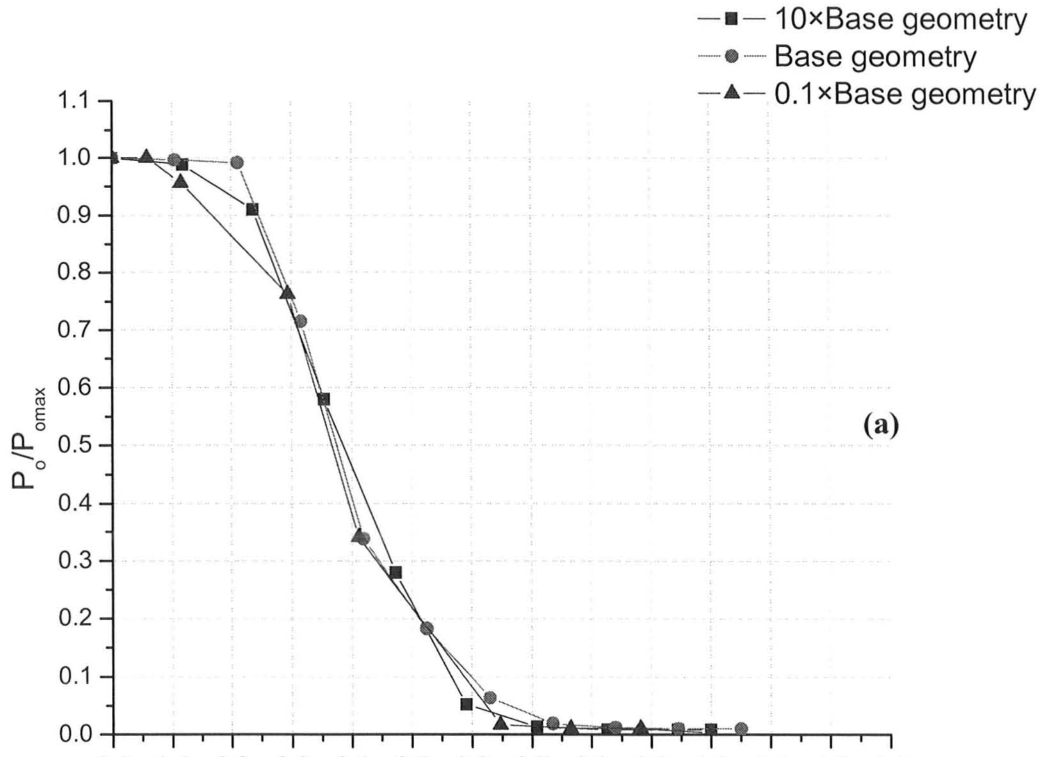

Figure 8-1: (a) Transfer curves for base geometry, 10×base geometry and 0.1×base geometry (L=15w, W_o=1.5w and W_c=100μm)

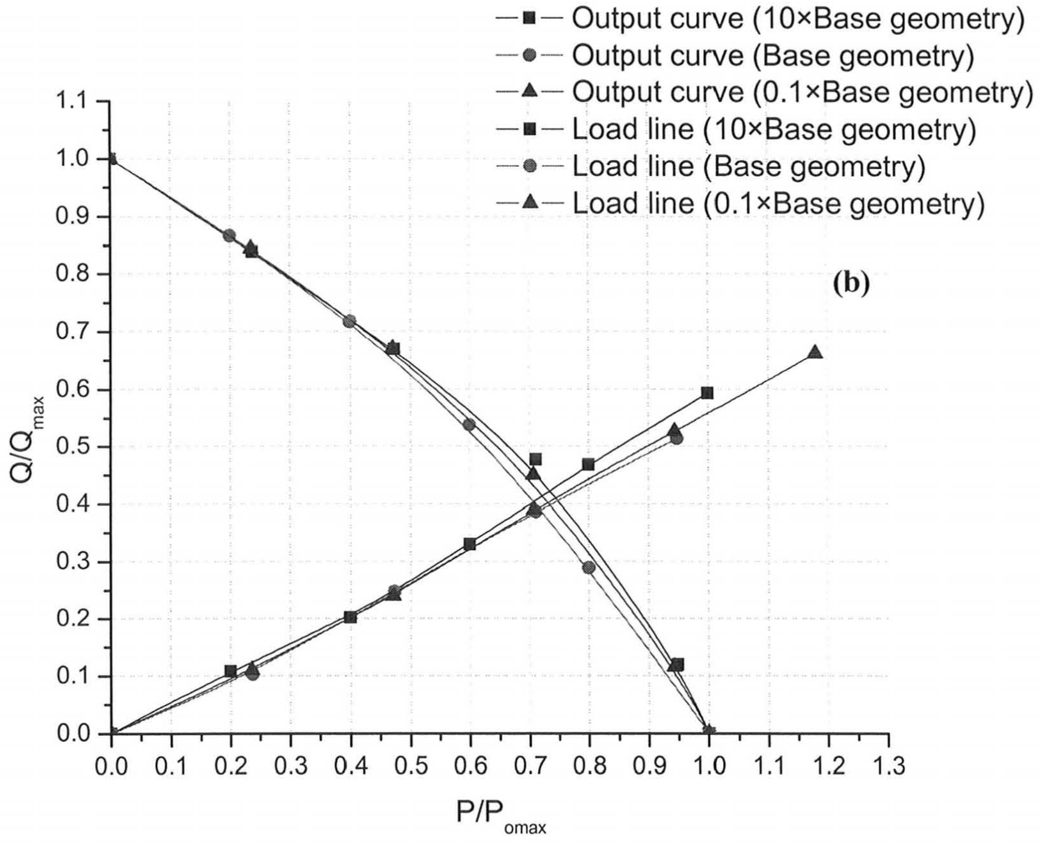

Figure 8-1: (b) The output characteristic curve and the load line for base geometry, 10×base geometry and 0.1×base geometry (L=15w, W_o=1.5w and W_c=100μm)

Thus the performance of the device is independent of geometry scaling at constant Reynolds number. It is important to understand how the switching time and the power consumption scales with geometry. The dependence of the switching time and the power consumption on geometry can be studied by scaling the geometry at constant Reynolds number. Switching time vs. geometry and power consumption vs. geometry at constant Reynolds number are explained in Section 8.2 and Section 8.3.1 respectively.

8.2 SWITCHING TIME vs. GEOMETRY

The switching time of a device is an important parameter of the device. The switching time of our device is the jet deflection time which is explained in Section 8.6.

The expected jet deflection time, $\tau_{Jexpected}$ is given as (Refer to Section 8.6):

$$\tau_{Jexpected} = \frac{\Delta P_s}{Q_s} \frac{W_c L^2 h}{2u_s^2 \rho W_s} \tag{8-1}$$

where ΔP_S: supply nozzle pressure drop

Q_S: flow rate through the supply nozzle

h: height of the device

W_c: width of the control ports

L: length of the device

u_S: supply velocity

W_S: width of the supply nozzle

ρ: fluid density

Thus if Reynolds number is to be kept constant, the jet deflection time scales as $\frac{[L]^{-2}}{[L]} \frac{[L]^3}{[L]^{-2}} = [L]^2$ (Refer to Table 8-2 for the scaling of the common physical quantities with geometry at constant Reynolds number).

Thus the switching time of the device scales as $[L]^2$. This is different from CMOS where intrinsic delays scale as [L]. Therefore, switching times benefit greatly from scaling down for microfluidic devices.

8.3.1 POWER vs. GEOMETRY

The power consumption of a jet is given by:

$$\text{Power} = P_s U_s A \tag{8-2}$$

where, P_s is the supply pressure, U_s is the velocity of the fluid in the nozzle and A is the cross-sectional area of the nozzle.

Thus at constant Reynolds number, Power scales as $[L]^{-3}[L]^{2}= [L]^{-1}$.

Thus the power consumption of the device goes up when the device is scaled down. This is quite surprising because in CMOS the power per unit area remains constant i.e. power consumption scales as $[L]^2$.

For a device with a supply nozzle width=50μm, height=50μm, supply pressure=20KPa and Reynolds number of supply jet=600, the power consumption was found to be 0.5mW. The energy is dissipated in the form of heat, which will raise the temperature of the fluid.

The heating might not be as severe as it first apperas as we scale down the devices. This is because as the devices are scaled down, the heat dissipation increases due to higher surface area to volume ratio. The effect of geometry on temperature is explored in Section 8.3.2.

The actual pump power required will be higher than what is calculated here because the efficiency of any available pump is not 100%. It is noted that Walker and Trask [8] reported a power consumption of 2mW, when 0.05mW is expected for their geometry and operating conditions. This discrepancy cannot be accounted for at this time.

8.3.2 TEMPERATURE CHANGE vs. GEOMETRY

As the supply jet moves, the shear forces (due to the viscosity of the fluid) act on the jet to change the constant velocity profile to a parabolic profile with zero velocity at the walls. The viscous work term is dissipative and is responsible for the heating of the fluid in our microfluidic devices. Shear forces are highest near the walls. Therefore the fluid near the walls is heated the most. This is shown in Figure 8-2.

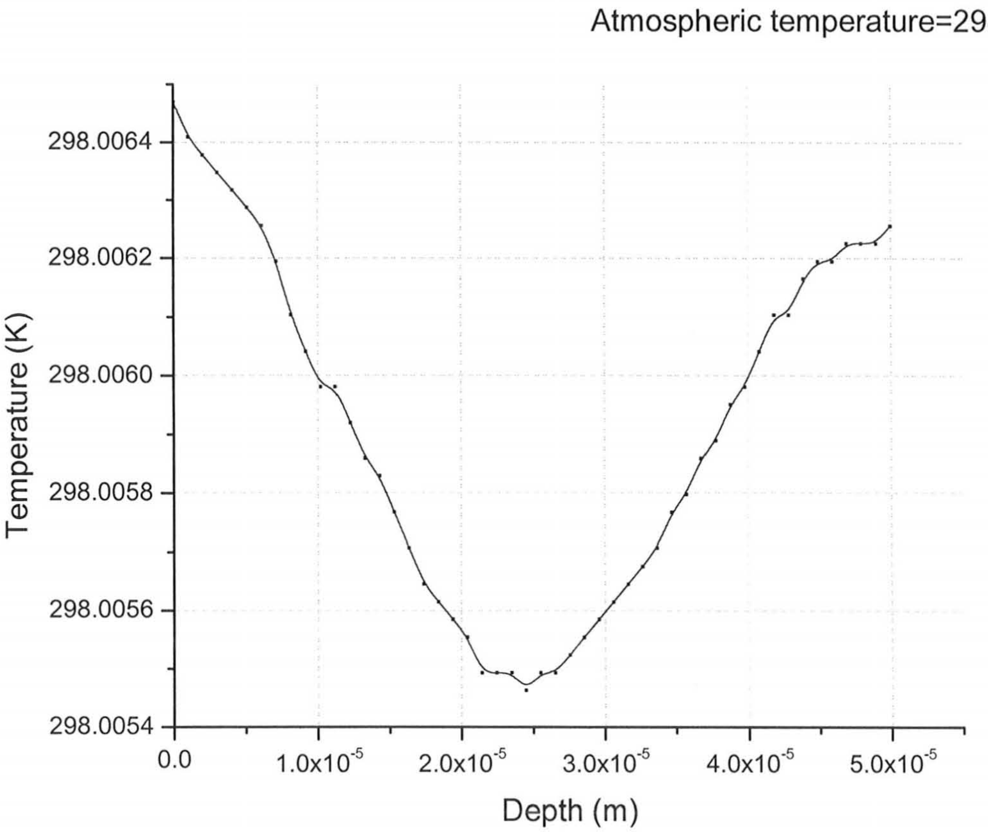

Figure 8-2: Temperature profile vs. depth of the device (L=18w, W_o=3w and W_c=80μm; Assumption: walls are adiabatic)

The change of temperature of a jet can be approximately given as:

$$\text{Power} = \dot{m} \times C \times \Delta T \tag{8-3}$$

where $\dot{m}$ is the mass flow rate of the supply jet, C is the specific heat of the fluid and ΔT is the change in temperature of the fluid.

From Section 8.3.1 we know that at constant Reynolds number power scales as $[L]^{-1}$ and from Table 8-2 we know that $\dot{m}$ scales as [L]. Therefore, ΔT scales as $[L]^{-2}$.

8.4 SUMMARY OF SCALING AT CONSTANT REYNOLDS NUMBER

A summary of the important parameters such as supply velocity (V_s), supply pressure (P_s), switching time (τ) and power consumption vs. geometry at constant Reynolds number is presented in Table 8-3.

	V_s (m/s)	P_s (KPa)	τ (ms)	Temperature change (K)	Power (mW)
10×base geometry	1	0.02	2.35×10^{1}	10^{-5}	0.05
base geometry	10	20	2.35×10^{-1}	10^{-3}	0.5
0.1×base geometry	100	2000	2.35×10^{-3}	10^{-1}	5

Table 8-3: Summary of the supply velocity (V_s), supply pressure (P_s), switching time (τ) and power consumption vs. geometry at constant Reynolds number

8.5 PHYSICAL BASIS FOR NON-LINEARITY IN TRANSFER CURVES

In this section the physical basis for non-linearity in the transfer curves of our device is explained.

The blocked load output pressure and the no-load velocity profiles are related to one another. The output pressure for the blocked load case and the corresponding output velocity for the no load case are plotted in Figure 8-3. Though the detailed relationship between the blocked load output pressure and the no-load velocity is complex, Figure 8-3 does show that the blocked load output pressure and the no-load velocity are simply related. Thus we can look at the velocity profiles to understand the blocked load output pressure.

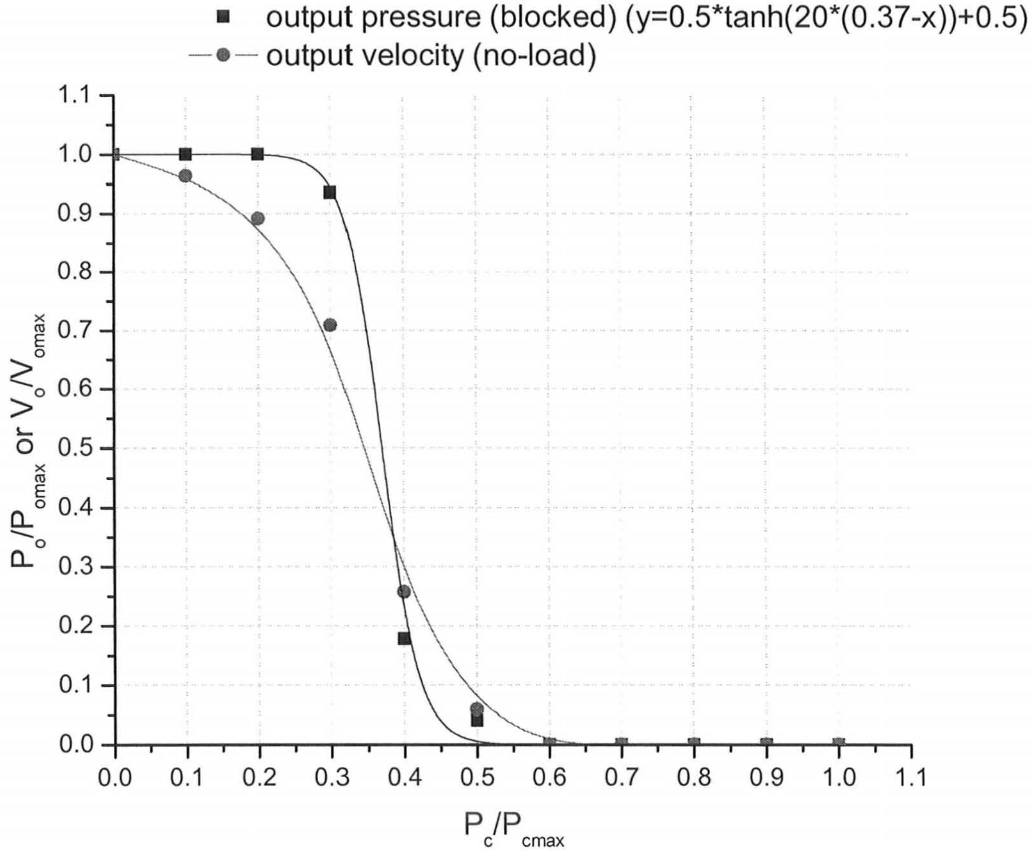

Figure 8-3: Blocked-load output pressure recovery and no-load output velocity as a function of control pressure (L=15w, W_o=1.5w and Re=600)

As shown in Figure 8-3 the transfer curve of the design shown in Figure 7-12 has a flattened region for low control pressures. Figure 8-4 (a), shows that a design with a straight bottom wall results in reducing the amount by which the supply jet is deflected on applying pressure in the control port. This is because there is a low pressure region near the bottom wall and is shown in Figure 8-4 (b). This low pressure region creates a wall-clinging effect, thereby reducing the deflection of the supply jet.

Physical Quantity	Scaling at constant Reynolds number
Dimension	[L]
Area	$[L]^2$
Velocity	$[L]^{-1}$
Flow rate	[L]
Pressure	$[L]^{-2}$

Table 8-2: Scaling of the common physical quantities with geometry at constant Reynolds number

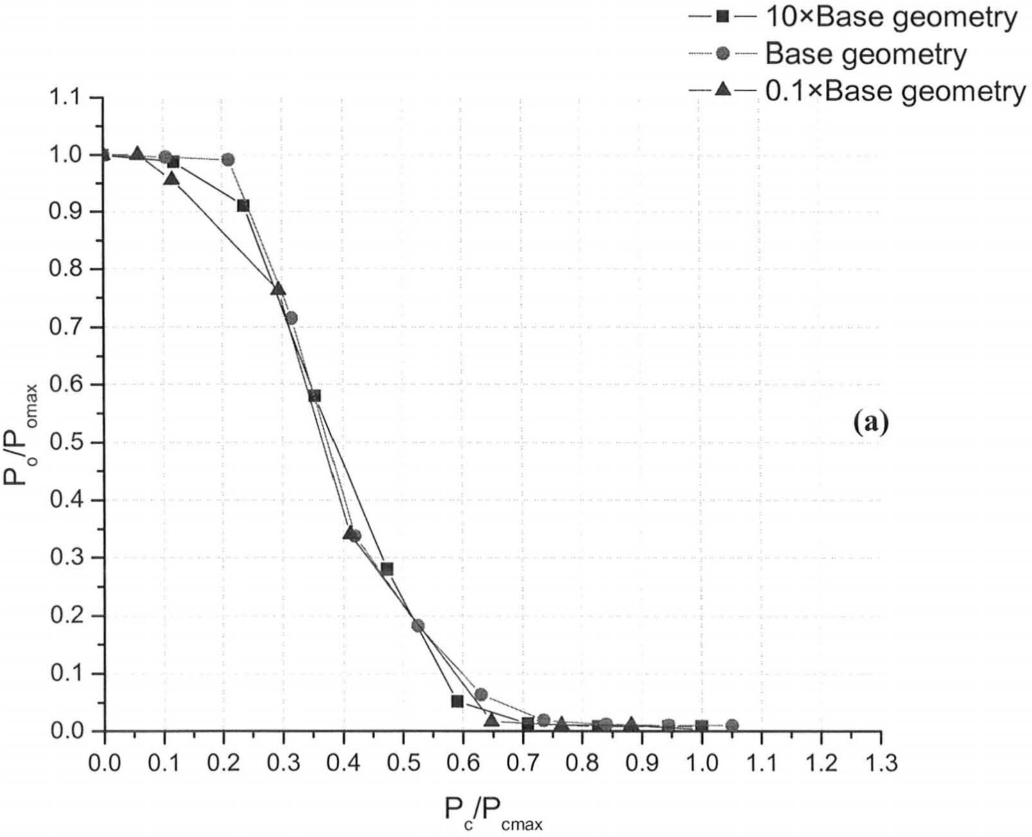

Figure 8-1: (a) Transfer curves for base geometry, 10×base geometry and 0.1×base geometry (L=15w, W_o=1.5w and W_c=100μm)

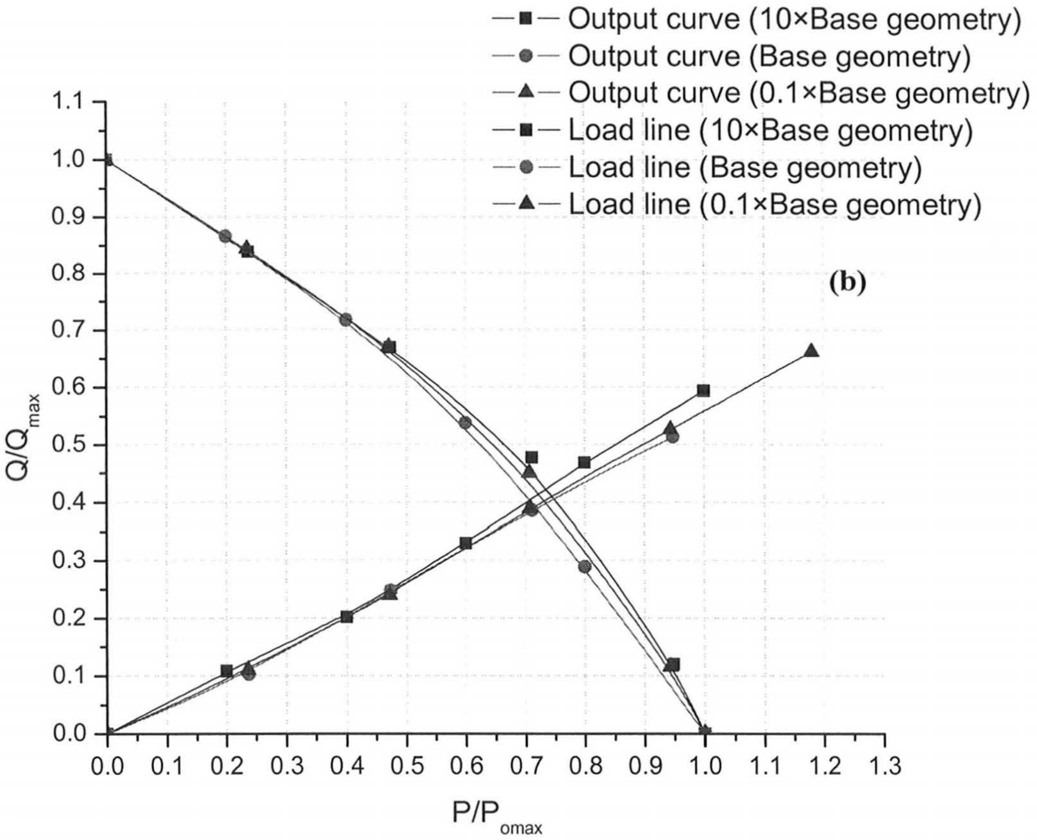

Figure 8-1: (b) The output characteristic curve and the load line for base geometry, 10×base geometry and 0.1×base geometry (L=15w, W_o=1.5w and W_c=100μm)

Thus the performance of the device is independent of geometry scaling at constant Reynolds number. It is important to understand how the switching time and the power consumption scales with geometry. The dependence of the switching time and the power consumption on geometry can be studied by scaling the geometry at constant Reynolds number. Switching time vs. geometry and power consumption vs. geometry at constant Reynolds number are explained in Section 8.2 and Section 8.3.1 respectively.

8.2 SWITCHING TIME vs. GEOMETRY

The switching time of a device is an important parameter of the device. The switching time of our device is the jet deflection time which is explained in Section 8.6.

The expected jet deflection time, $\tau_{\text{Jexpected}}$ is given as (Refer to Section 8.6):

$$\tau_{\text{Jexpected}} = \frac{\Delta P_s}{Q_s} \frac{W_c L^2 h}{2u_s^2 \rho W_s} \tag{8-1}$$

where ΔP_S: supply nozzle pressure drop

Q_s: flow rate through the supply nozzle

h: height of the device

W_c: width of the control ports

L: length of the device

u_s: supply velocity

W_S: width of the supply nozzle

ρ: fluid density

Thus if Reynolds number is to be kept constant, the jet deflection time scales as $\frac{[L]^{-2}}{[L]} \frac{[L]^3}{[L]^{-2}} = [L]^2$ (Refer to Table 8-2 for the scaling of the common physical quantities with geometry at constant Reynolds number).

Thus the switching time of the device scales as $[L]^2$. This is different from CMOS where intrinsic delays scale as [L]. Therefore, switching times benefit greatly from scaling down for microfluidic devices.

8.3.1 POWER vs. GEOMETRY

The power consumption of a jet is given by:

$$\text{Power} = P_sU_sA \tag{8-2}$$

where, P_s is the supply pressure, U_s is the velocity of the fluid in the nozzle and A is the cross-sectional area of the nozzle.

Thus at constant Reynolds number, Power scales as $[L]^{-3}[L]^{2}= [L]^{-1}$.

Thus the power consumption of the device goes up when the device is scaled down. This is quite surprising because in CMOS the power per unit area remains constant i.e. power consumption scales as $[L]^2$.

For a device with a supply nozzle width=50µm, height=50µm, supply pressure=20KPa and Reynolds number of supply jet=600, the power consumption was found to be 0.5mW. The energy is dissipated in the form of heat, which will raise the temperature of the fluid.

The heating might not be as severe as it first apperas as we scale down the devices. This is because as the devices are scaled down, the heat dissipation increases due to higher surface area to volume ratio. The effect of geometry on temperature is explored in Section 8.3.2.

The actual pump power required will be higher than what is calculated here because the efficiency of any available pump is not 100%. It is noted that Walker and Trask [8] reported a power consumption of 2mW, when 0.05mW is expected for their geometry and operating conditions. This discrepancy cannot be accounted for at this time.

8.3.2 TEMPERATURE CHANGE vs. GEOMETRY

As the supply jet moves, the shear forces (due to the viscosity of the fluid) act on the jet to change the constant velocity profile to a parabolic profile with zero velocity at the walls. The viscous work term is dissipative and is responsible for the heating of the fluid in our microfluidic devices. Shear forces are highest near the walls. Therefore the fluid near the walls is heated the most. This is shown in Figure 8-2.

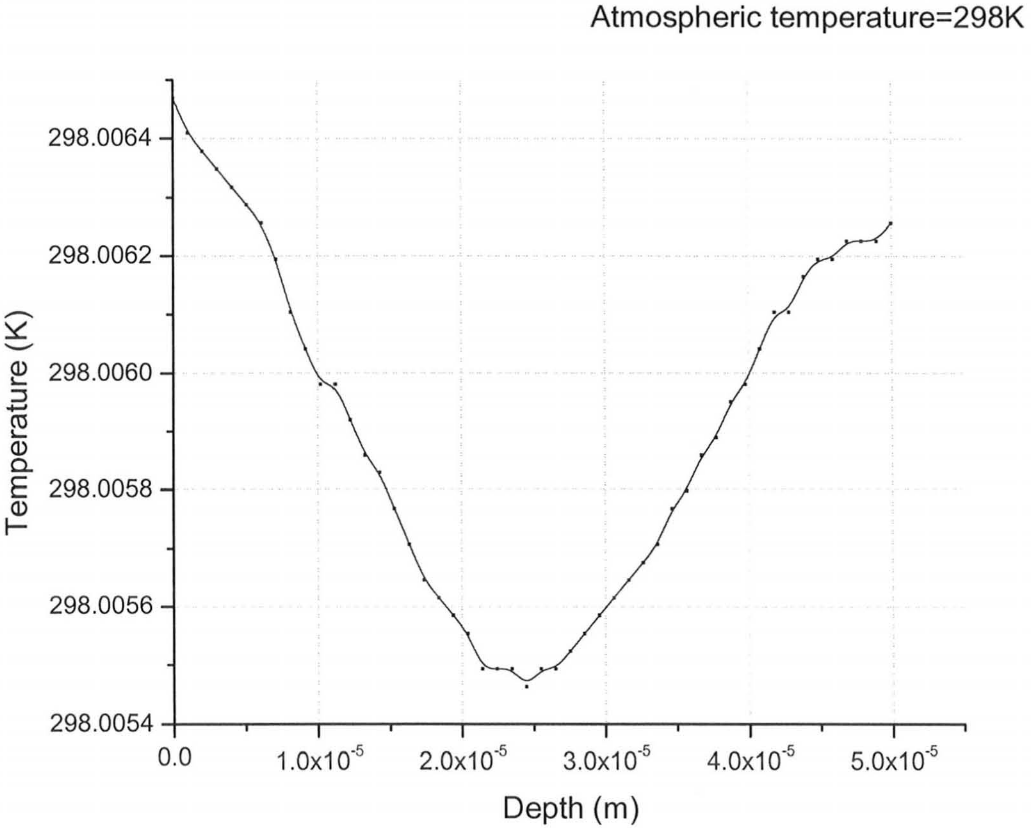

Figure 8-2: Temperature profile vs. depth of the device (L=18w, W_o=3w and W_c=80μm; Assumption: walls are adiabatic)

The change of temperature of a jet can be approximately given as:

$$\text{Power} = \dot{m} \times C \times \Delta T \qquad (8\text{-}3)$$

where $\dot{m}$ is the mass flow rate of the supply jet, C is the specific heat of the fluid and ΔT is the change in temperature of the fluid.

From Section 8.3.1 we know that at constant Reynolds number power scales as $[L]^{-1}$ and from Table 8-2 we know that $\dot{m}$ scales as [L]. Therefore, ΔT scales as $[L]^{-2}$.

8.4 SUMMARY OF SCALING AT CONSTANT REYNOLDS NUMBER

A summary of the important parameters such as supply velocity (V_s), supply pressure (P_s), switching time (τ) and power consumption vs. geometry at constant Reynolds number is presented in Table 8-3.

	V_S (m/s)	P_S (KPa)	τ (ms)	Temperature change (K)	Power (mW)
10×base geometry	1	0.02	2.35×10^{1}	10^{-5}	0.05
base geometry	10	20	2.35×10^{-1}	10^{-3}	0.5
0.1×base geometry	100	2000	2.35×10^{-3}	10^{-1}	5

Table 8-3: Summary of the supply velocity (V_s), supply pressure (P_s), switching time (τ) and power consumption vs. geometry at constant Reynolds number

8.5 PHYSICAL BASIS FOR NON-LINEARITY IN TRANSFER CURVES

In this section the physical basis for non-linearity in the transfer curves of our device is explained.

The blocked load output pressure and the no-load velocity profiles are related to one another. The output pressure for the blocked load case and the corresponding output velocity for the no load case are plotted in Figure 8-3. Though the detailed relationship between the blocked load output pressure and the no-load velocity is complex, Figure 8-3 does show that the blocked load output pressure and the no-load velocity are simply related. Thus we can look at the velocity profiles to understand the blocked load output pressure.

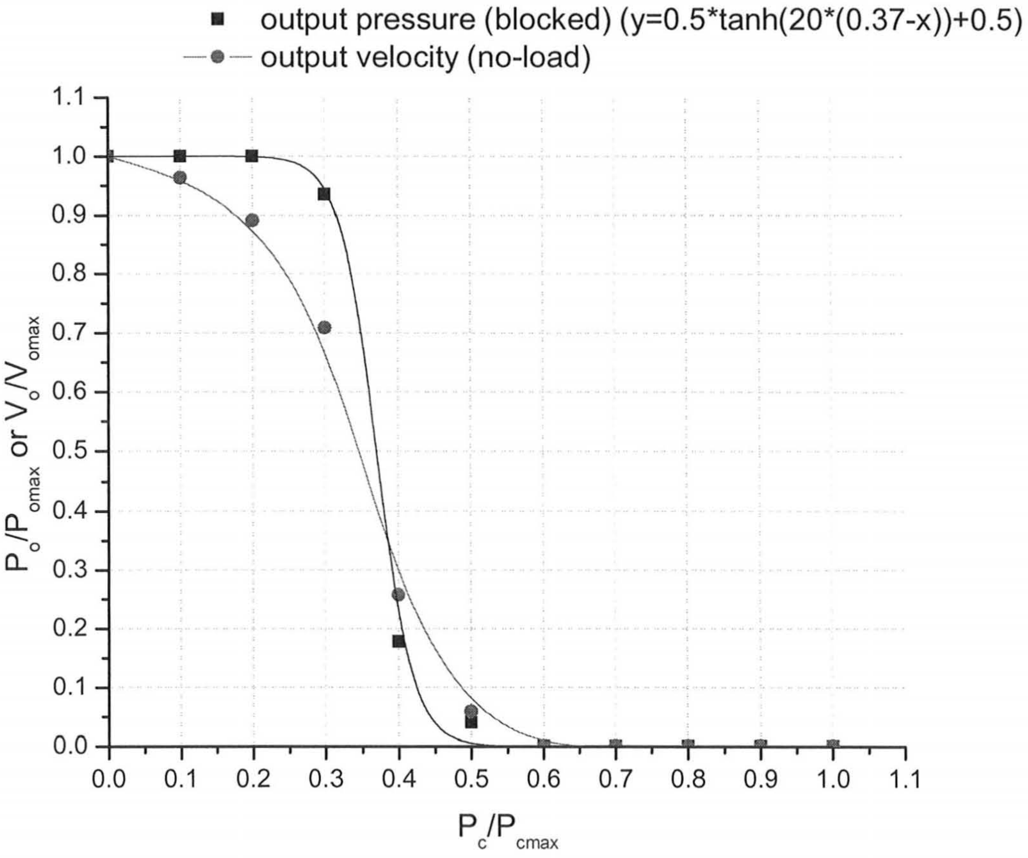

Figure 8-3: Blocked-load output pressure recovery and no-load output velocity as a function of control pressure (L=15w, W_o=1.5w and Re=600)

As shown in Figure 8-3 the transfer curve of the design shown in Figure 7-12 has a flattened region for low control pressures. Figure 8-4 (a), shows that a design with a straight bottom wall results in reducing the amount by which the supply jet is deflected on applying pressure in the control port. This is because there is a low pressure region near the bottom wall and is shown in Figure 8-4 (b). This low pressure region creates a wall-clinging effect, thereby reducing the deflection of the supply jet.

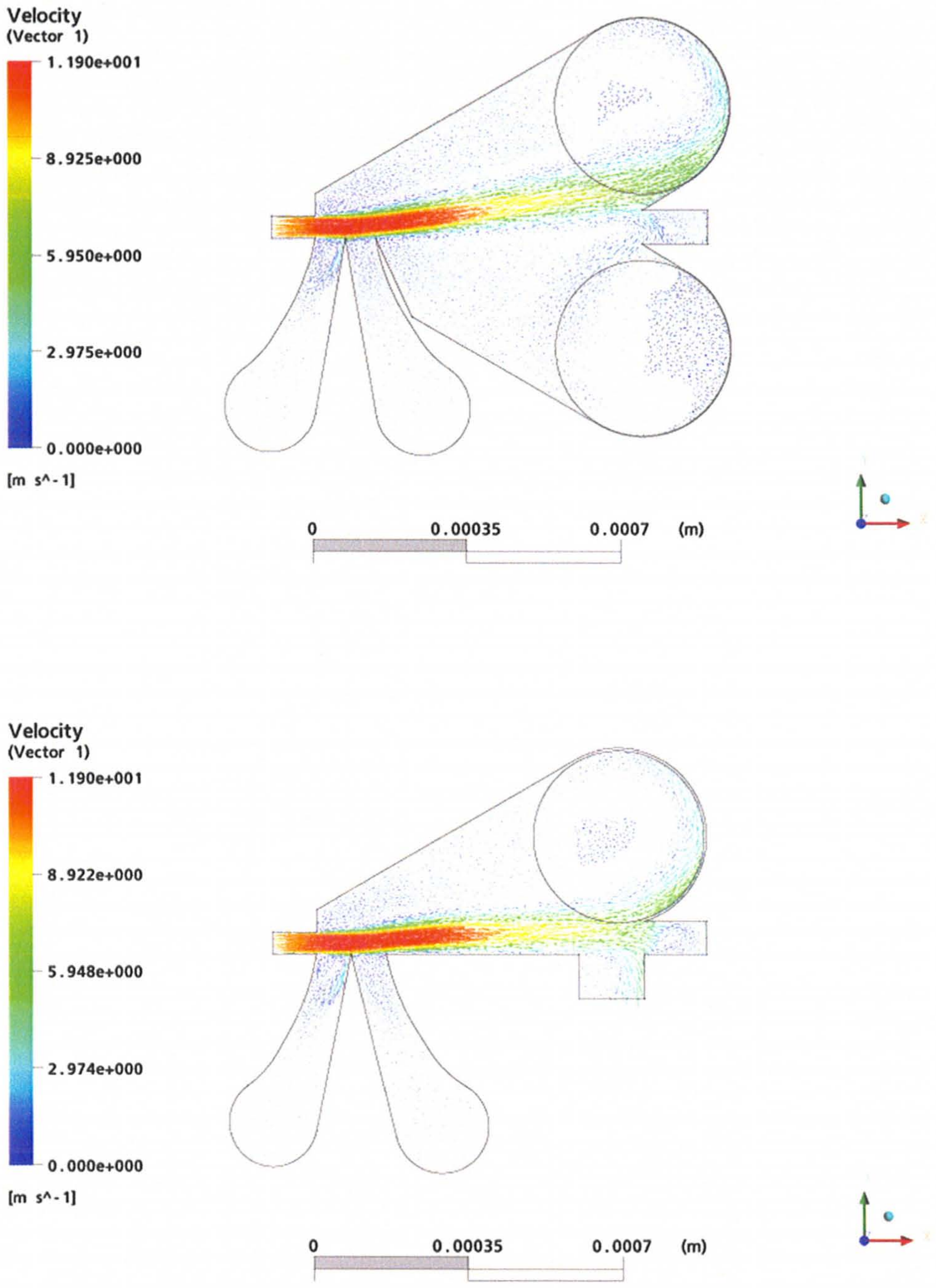

Figure 8-4: (a) A comparison of the jet deflection of two designs on applying a pressure of 6KPa to the second control port (L=15w, W_o=1.5w, Re=600 and xy plane at z=25μm)

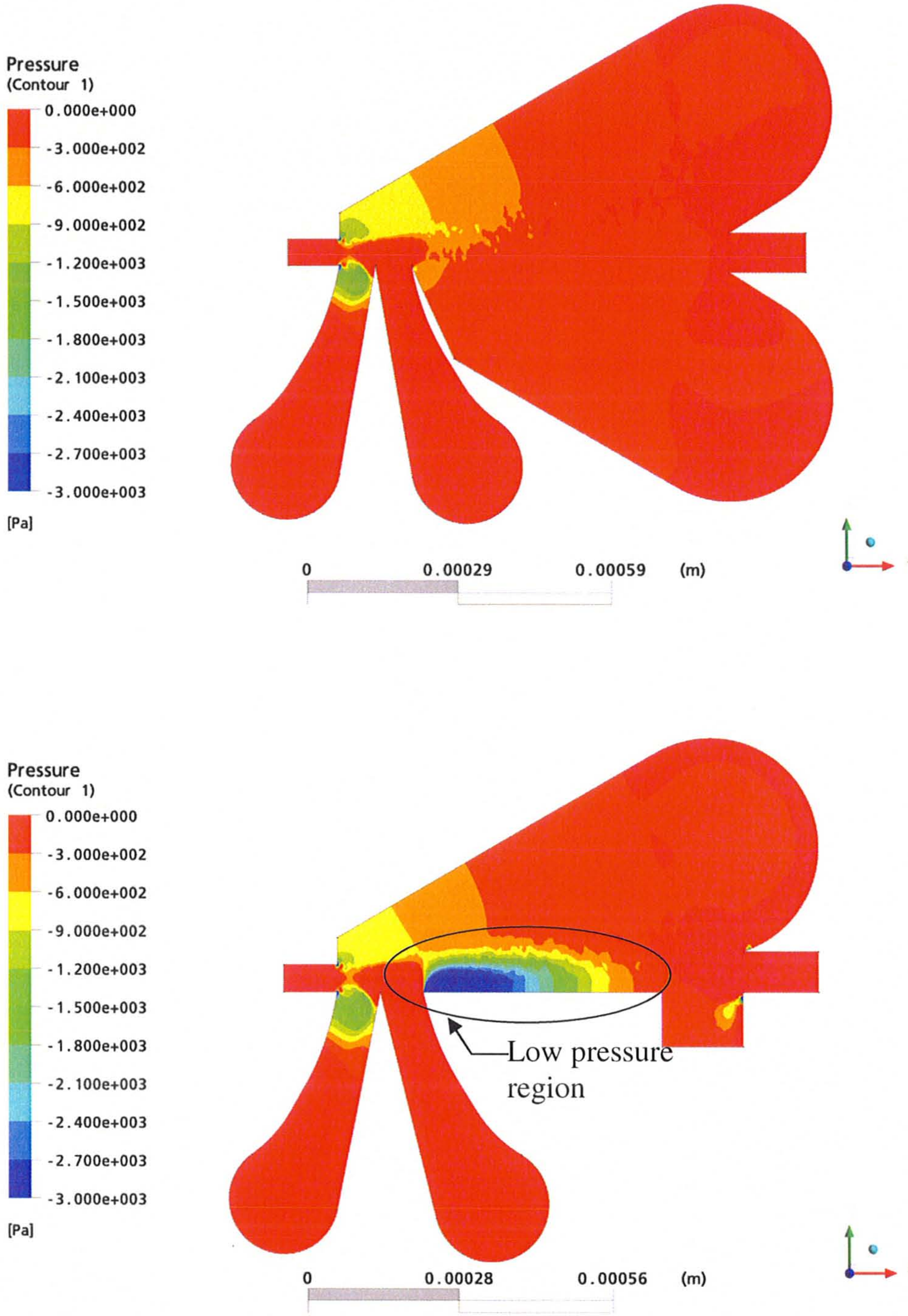

Figure 8-4: (b) A comparison of the pressure profile near bottom wall for the two designs on applying a pressure of 6KPa to the second control port (L=15w, W_o=1.5w, Re=600 and xy plane at z=25μm)

Since the supply jet is deflected by a small amount on applying higher control pressures, it can grow between the bottom wall and the deflected core. Thus the average velocity of the captured jet remains the same for a range of applied control pressures which results in a flattening effect in the transfer curve for low control pressures. On increasing the pressure in the control port further the core of the jet is deflected by a large amount. Then the output pressure recovery begins to drop. The velocity profile of the jet as a function of the distance with respect to the bottom wall for different control pressures is illustrated in Figure 8-5. It is noted that the velocity at the wall>0. This is because the development length of the jet at Re~600 is 30W (1500μm) where W is the width of the supply nozzle, which is much longer than the length of the device. The development length is defined as the length at which the jet velocity distribution acquires a parabolic profile with a zero velocity at the walls.

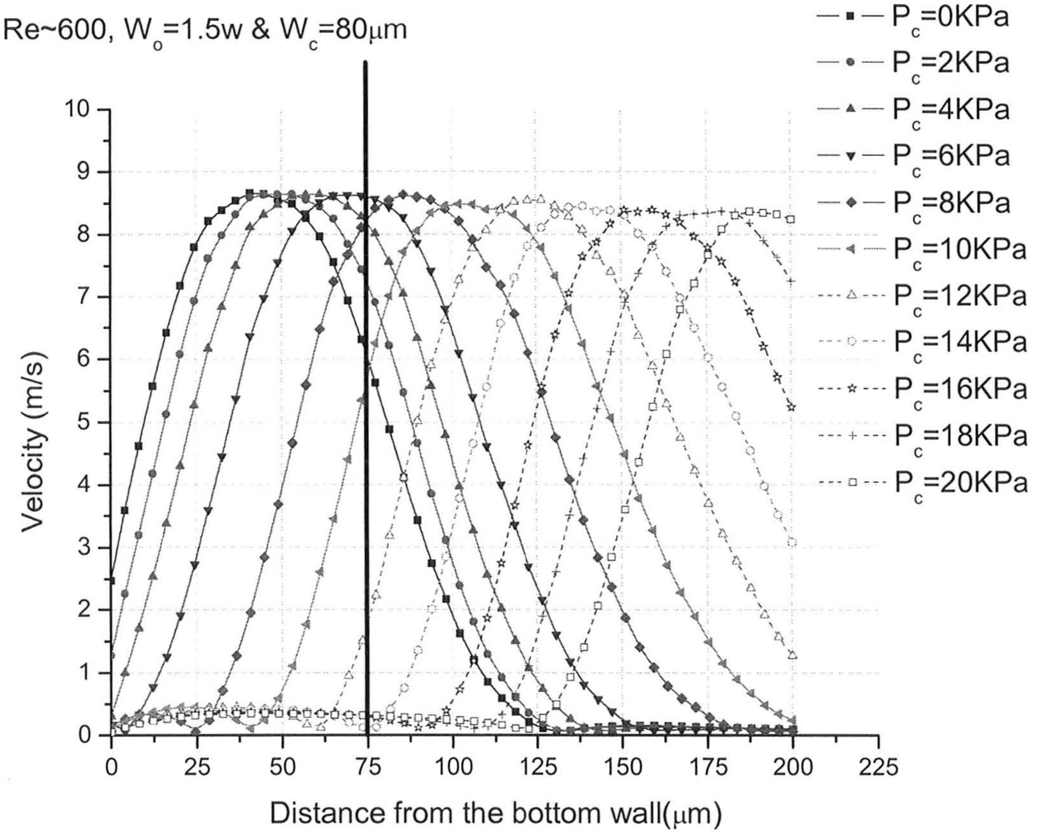

Figure 8-5: Jet velocity profile for different control pressures (Re~600, W_o=1.5w=75μm, W_c=80μm) (x=550μm, z=25μm)

A flat region is observed for high control pressures due to the following reason: Once the pressure in the control port is large enough to deflect the supply jet to the circular vent the output pressure is close to zero. As the control pressure is increased the angle by which the jet is deflected continues to increase but the output pressure is fixed to zero because the entire supply jet is dumped into the circular vent. Thus we observe a flat region in the transfer curves for high control pressures.

8.6 PHYSICAL BASIS FOR SWITCHING TIME

The switching time is an important characteristic of the device. The switching time could be of two general types:

(1) Transit time and;
(2) Jet deflection time.

The switching time was calculated by simulating the time-dependant behavior of a NOR device. A pressure of 15KPa was applied at the control port. The time was varied from 0-2ms in the time-steps of 0.02ms.

The angle of deflection of the jet (as shown in Figure 8-6 (a)) at x=100μm and x=500μm ('x' are marked in Figure 8-6 (b)) are plotted in Figure 8-7. The time required to deflect the jet at x=500μm is larger than the time required to deflect the jet at x=100μm. This is because the supply jet is not rigid.

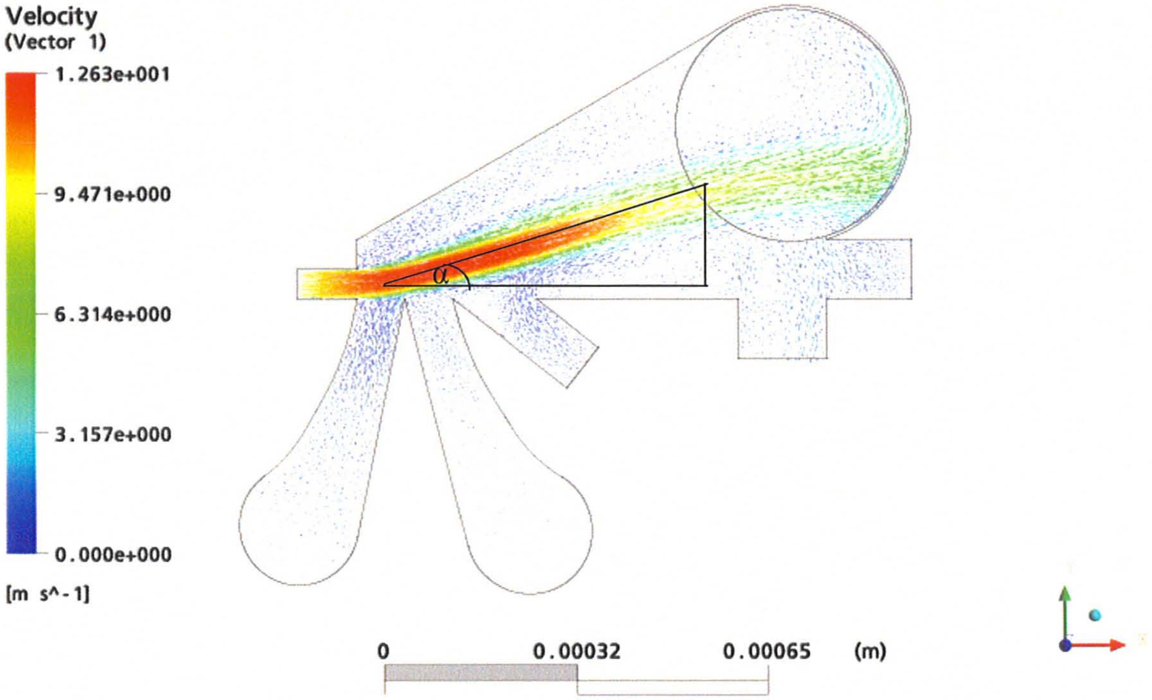

Figure 8-6: (a) Inset showing the angle of deflection (α) of the supply jet

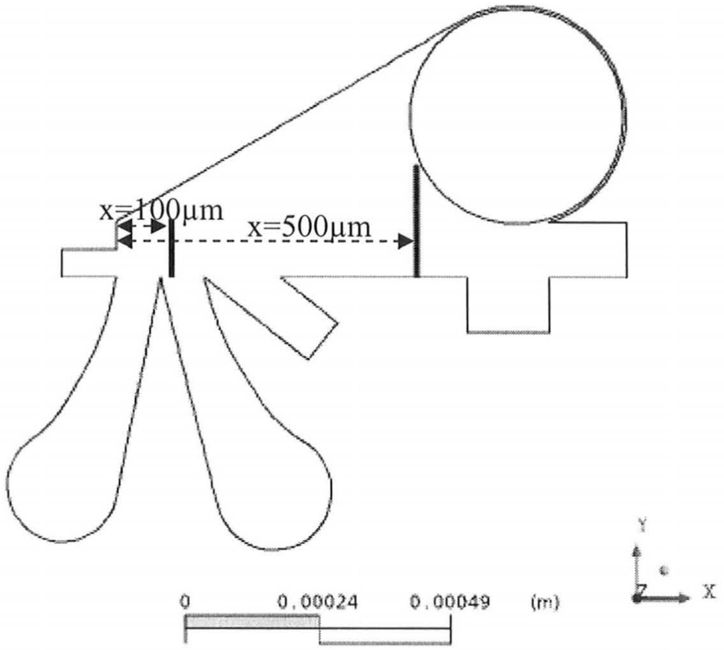

Figure 8-6: (b) Inset showing x=100µm and x=500µm

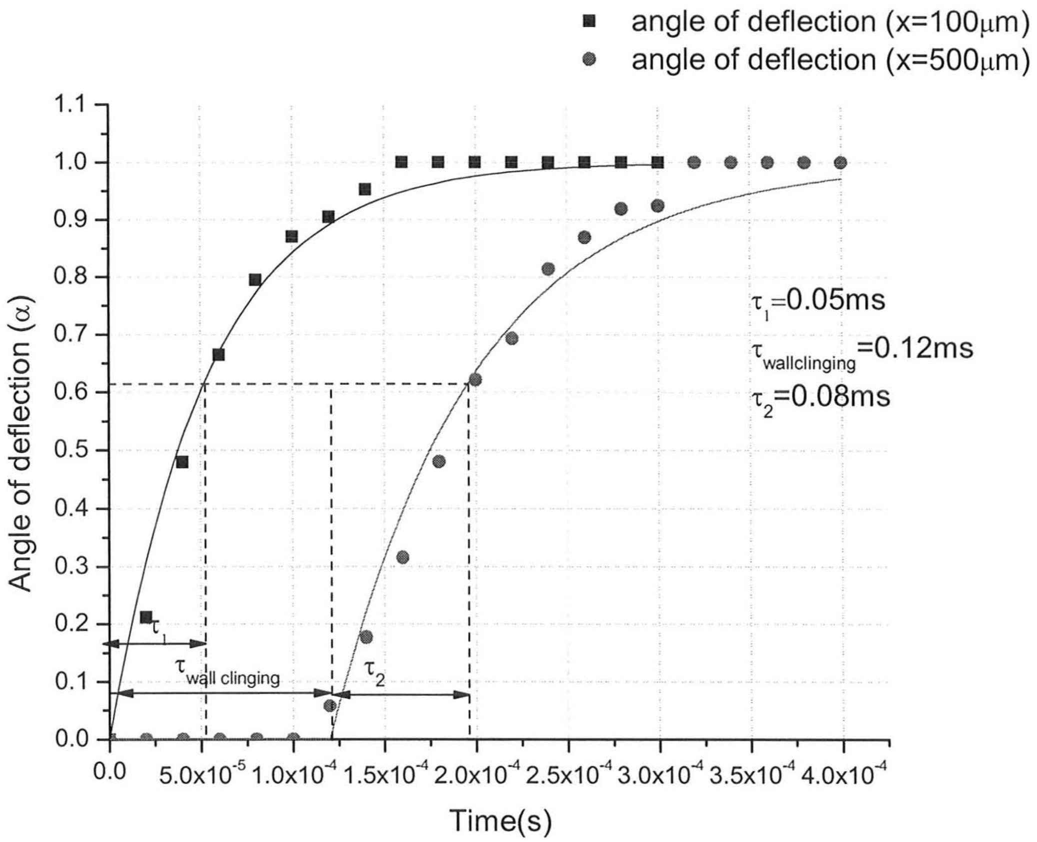

Figure 8-7: Switching time of a device with critical dimension of 50μm, Wc=80μm, L=15w and Re~600

The time required to deflect the tail of the jet determines the switching time of the device. Therefore the angle of deflection of the jet at x=500μm was fit to the following function:

$$y_o + Ae^{\left(\frac{-t}{\tau_J}\right)} \tag{8-4}$$

This is shown in Figure 8-7. The switching time (τ) obtained from the simulation results is approximately equal to the jet deflection time (τ_J) which will be explained in Subsection 8.6.2.

$$\tau = \tau_J \tag{8-5}$$

where τ: switching time

τ_J: jet deflection time

We found that the jet deflection time (τ_2) =0.08ms and the time constant associated with the wall clinging effect ($\tau_{wallclinging}$) =0.12ms.

To provide theoretical insights to the time constants, in the following sub sections we have used the concept of fluidic resistance, capacitance and inductance. This analysis is valid for our devices because at the operating Reynolds number the flow in our devices is Poiseuille's flow.

8.6.1 TRANSIT TIME (τ_T):

The transit time is defined as the time required by the control pressure to propagate from the bottom of the control port to the top of the control port. The expected transit time ($\tau_{Texpected}$) is calculated as follows:

$$\tau_{Texpected} = \frac{L}{R} \tag{8-6}$$

where R: resistance of the control port

L: Inductance of the control port

From Section 7.3, we know that:

$$R = 5 \times 10^{12} \ \text{Pa·s/m}^3 \tag{8-7}$$

Inductance of the control port is defined as:

$$L = \frac{\rho l}{A} \tag{8-8}$$

where l is the length of the control port, A is the cross-sectional area and ρ is the fluid density. Substituting numbers in Equation 8-8, we obtain:

$$L=1.0\times10^{8}\ Kg/\ m^{4} \tag{8-9}$$

Substituting Equation 8-9 and Equation 8-7 in Equation 8-6, we obtain:

$$\tau_{Texpected}=0.02ms \tag{8-10}$$

The simulated transit time ($\tau_{Tsimulated}$) was obtained as follows: A plane was cut near the top of the control port. The normalized control pressure (at the plane) vs. time was plotted in Figure 8-8. The obtained data was fitted to an exponential growth function to obtain the simulated transit time. The simulated transit time ($\tau_{Tsimulated}$) of the device was found to ~0.024ms.

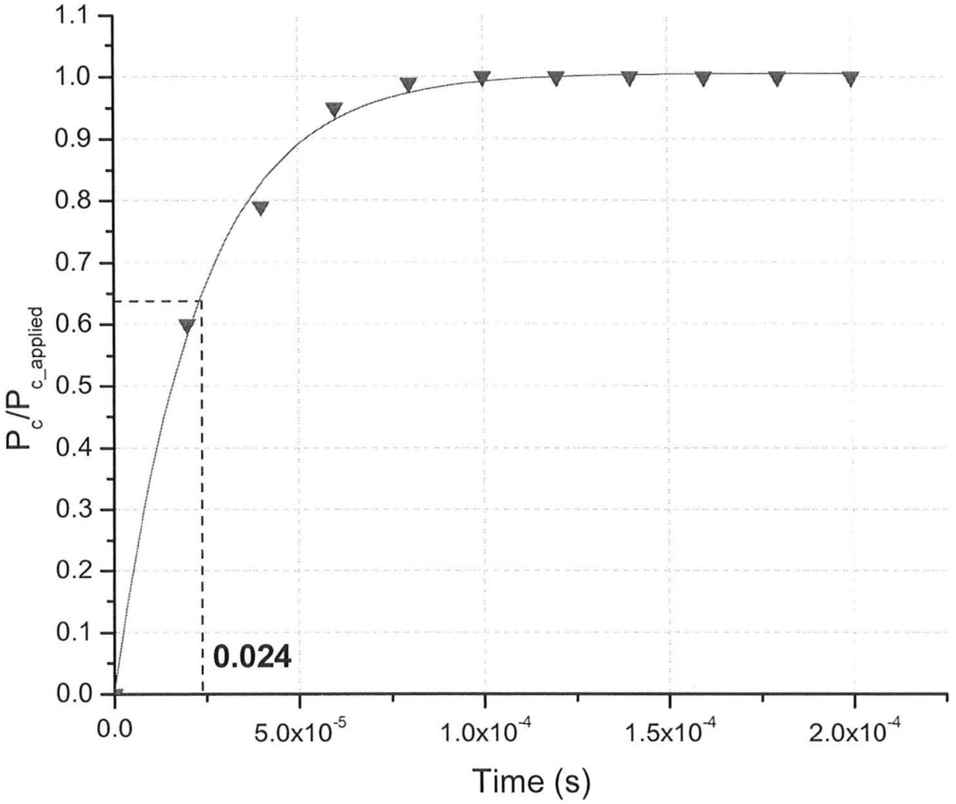

Figure 8-8: Transit time of a device with critical dimension of 50μm and Re~600

The expected transit time ($\tau_{Texpected}$) and the simulated transit time ($\tau_{Tsimulated}$) are quite close. The simulated transit time is however 10 times smaller than the switching time of the device (shown in Figure 8-7). Therefore, the switching time of the device is not governed by the transit time of the device.

8.6.2 JET DEFLECTION TIME (τ_J):

The expected jet deflection ($\tau_{Jexpected}$) time can be calculated by using a simple theoretical model. It was calculated as follows:

$$\tau_{Jexpected}=RC \tag{8-11}$$

where R: supply jet resistance

and C: fluid capacitance.

$$\text{Supply jet resistance, } R = \frac{\Delta P_s}{Q_s} \tag{8-12}$$

where ΔP_s is the supply pressure and Q_s is the supply flow rate.

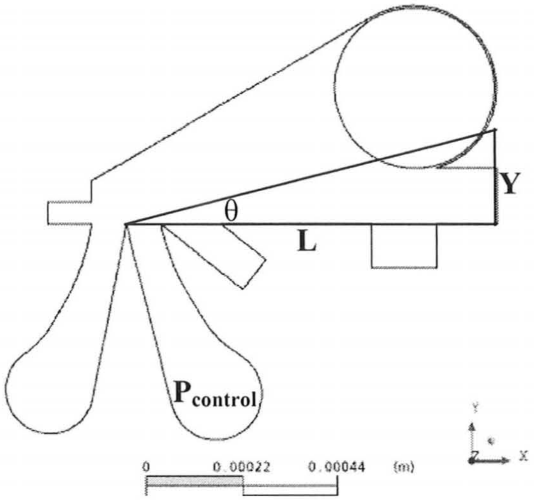

Figure 8-9: Required parameters to define the capacitance of the device

Fluidic capacitance is defined as:

$$\frac{dV}{dP} = \frac{Lh}{2}\frac{dY}{dP_c} \tag{8-13}$$

where, V is the volume, P is the pressure, h is the height of the device and L and Y are defined in Figure 8-9.

From Equation 3-9:

$$\tan\theta = \frac{Y}{L} = \frac{P_c W_c + F_{wall}/h}{\rho u_s^2 W_s} \tag{8-14}$$

Substituting Equation 8-14 in Equation 8-13 and taking the derivative with respect to P_c, we obtained:

$$C = \frac{W_c L^2 h}{2u_s^2 \rho W_s} \tag{8-15}$$

Substituting Equation 8-12 and Equation 8-15 in Equation 8-11, we obtained:

$$\tau_{\text{Jexpected}} = \frac{\Delta P_s}{Q_s} \frac{W_c L^2 h}{2u_s^2 \rho W_s} \tag{8-16}$$

Substituting numbers in Equation 8-16, $\tau_{\text{Jexpected}}$=0.24ms. The expected jet deflection time ($\tau_{\text{Jexpected}}$) and the simulated jet deflection time of the device (τ_2=0.08ms) as observed in Figure 8-7, agree to one another by a factor of 3. Therefore we conclude that the switching time of the device is governed by the jet deflection time.

From Figure 8-7, we can see that τ_1 (0.05ms) and τ_2 (0.08ms) are quite close. This is because τ_1 and τ_2 are both associated with the jet deflection time of the device. It should also be noted that there is another time constant called $\tau_{\text{wallclinging}}$ as shown in Figure 8-7. The origin of this time constant is due to the clinging of the jet to the bottom wall. This is because there is a low pressure region near the bottom wall (as shown in Figure 8-4 (b)). This low pressure region created a wall-clinging effect, thereby introducing a time constant associated with it.

CHAPTER 9 MICROFLUIDIC LOGIC DEVICES

9.1 HALF ADDER

A half adder is an important component of a computing system to perform arithmetic operations [17]. A half adder performs one digit operation. It has two inputs, 'A' and 'B' and two outputs, 'Sum' and 'Carry'. Refer to Table 5-2 for the truth table of a half adder. Our half-adder is a combination of 5 NOR gates and is shown in Figure 9-1.

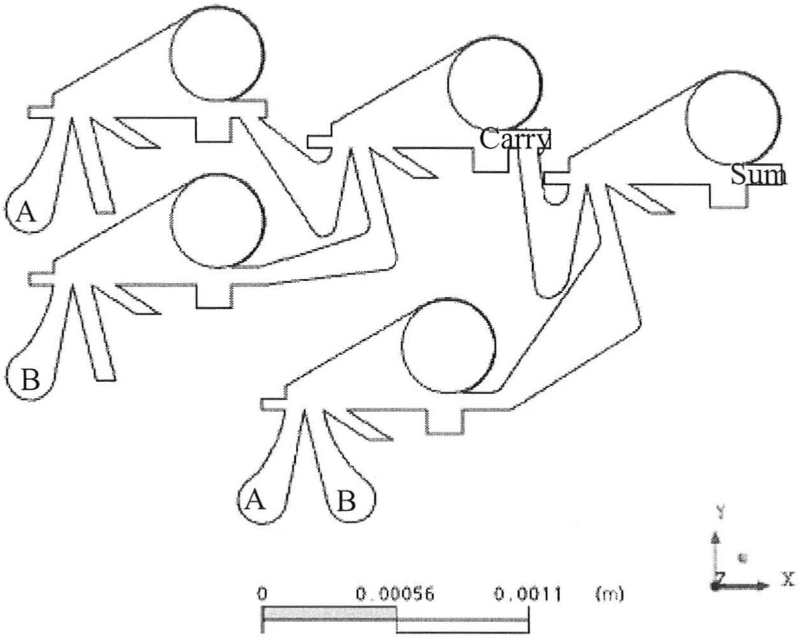

Figure 9-1: Microfluidic half-adder

Steady-state simulations were performed to analyze a half-adder circuit because the time-dependence is not of critical importance for a half-adder. The output 'Sum' of a half adder is high when either of the inputs is high. 'Sum' is low when both the inputs are either low or high. When both the inputs are high, 'Carry' is high. All these four states of a half-adder circuit are shown in Figure 9-2 (a), (b), (c) and (d).

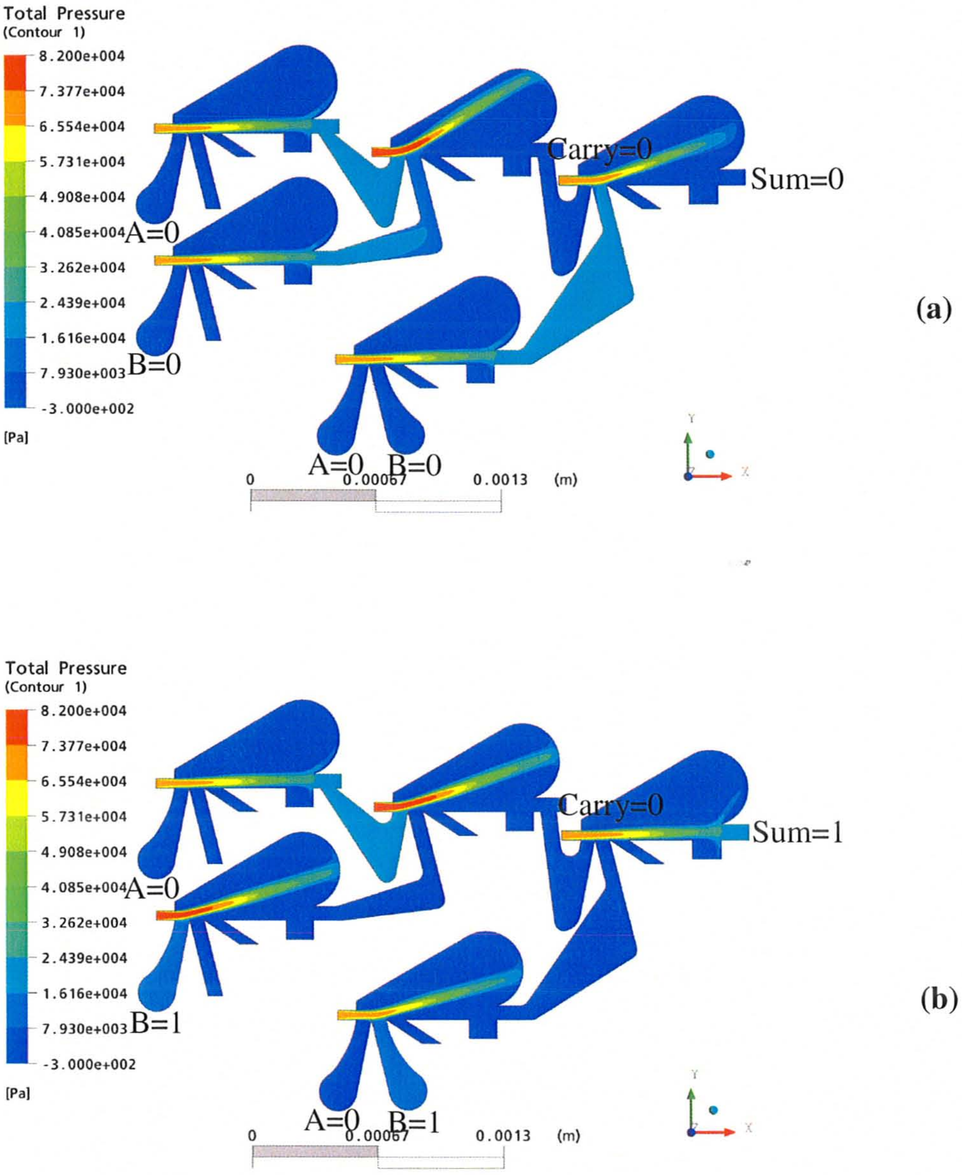

Figure 9-2: (a) A=0, B=0, Carry=0, Sum=0 and (b) A=0, B=1, Carry=0, Sum=1

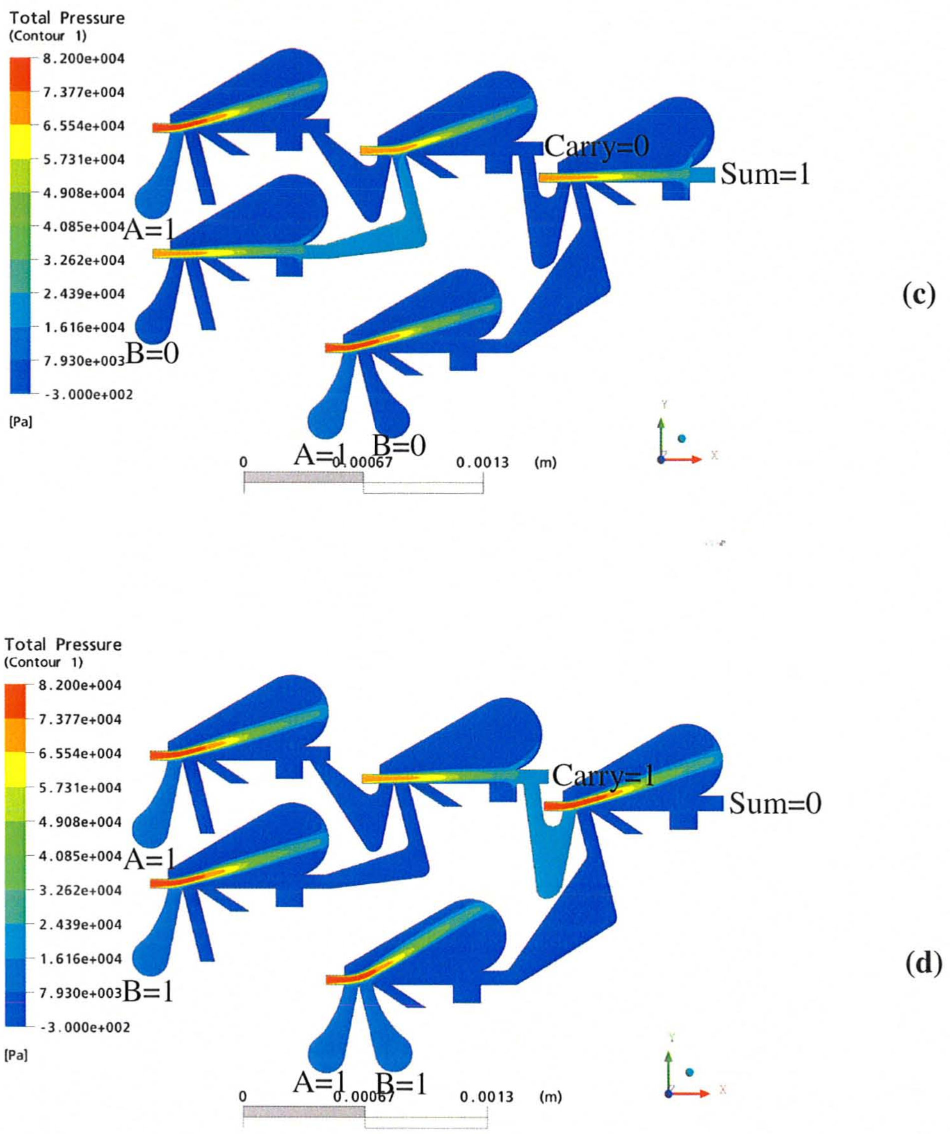

Figure 9-2: (c) A=1, B=0, Carry=0, Sum=1 and (d) A=1, B=1, Carry=1, Sum=0

The pressure drop in interconnects should be low because we need the pressure head to drive the next-level gates. A possible design for low impedance interconnects is shown in the half-adder model. A half adder does not give any new information about the device. It simply demonstrates that arithmetic operations can be performed using microfluidic logic.

9.2 CLOCK

A clock is a fundamental requirement of a synchronized computing system [23]. The timing specifications of a system are performed by using a clock system. A clock system has two functions: clock generation and clock distribution. Clock generation circuitry is used to generate timing signals which are then used to synchronize the changes in the system state. A network called clock distribution, distributes the generated signal to its destination. Our designed microfluidic clock is shown in Figure 9-3.

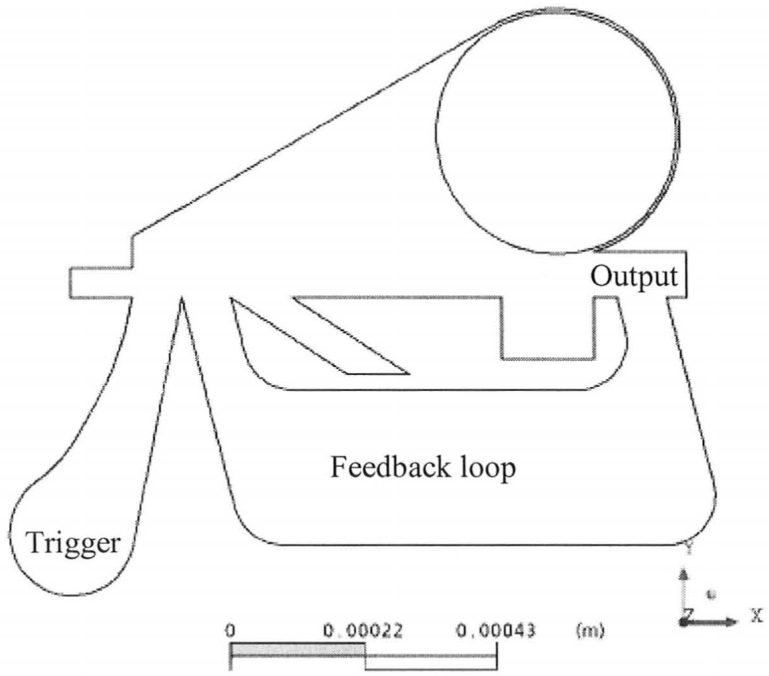

Figure 9-3: Microfluidic clock

This clock is the simplest example of a ring oscillator. A ring oscillator is N stages of cascaded inverting gates where N is an odd number. The clock cycles are shown in Figure 9-4. The frequency of the circuit can be reduced by increasing the number of stages. Also as the number of stages increases, the waveform changes from a sinusoidal oscillation to a square-wave oscillation. This is because as the number of stages increases, the time period gets much larger than the switching time, thereby making the waveform looks like a square-wave.

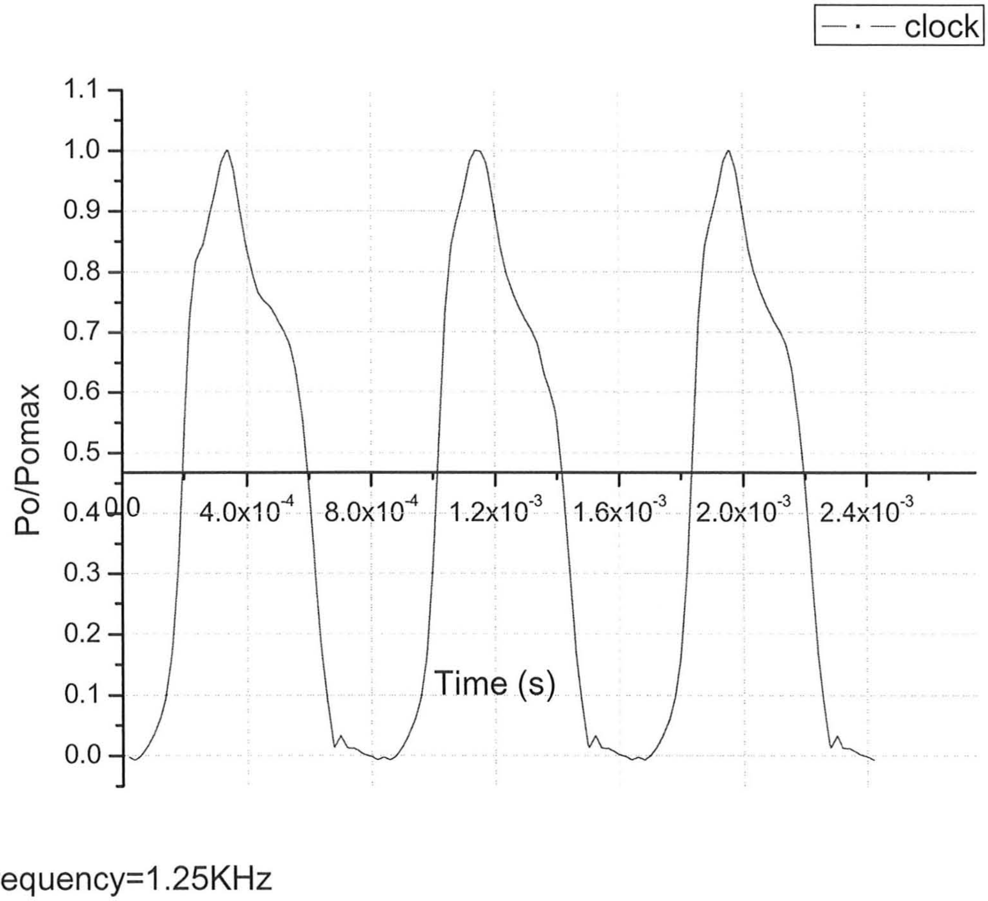

Figure 9-4: Clock cycles of the ring-oscillator

A high pressure pulse is applied to 'Trigger' which forces the output to be zero as shown in Figure 9-5 (a). Once the pressure pulse applied to 'Trigger' disappears, both the inputs of the clock become zero. As a result the deflected jet is unable to maintain its deflection. The output of the device becomes as shown in Figure 9-5 (b). This high-state output when fedback to the input results in the deflection of the jet, thereby forcing the output to zero. This is shown in Figure 9-5 (c). Thus the ring oscillator oscillates from low to high and high to low.

The frequency of the clock is 1.25 KHz. As shown in Section 8-6 the time constant of a NOR gate is 0.216×10^{-3}s which approximately give us a frequency of 2.3 KHz. The frequency of the clock is slower than that of a NOR device because of the following reason: As mentioned in Section 8.6 the supply jet is not rigid. Therefore the tail of the jet continues to cling to the bottom wall even when the middle of the jet is deflected. This wall clinging effect is responsible for the smaller frequency of the clock. Another reason for the slower frequency of the clock is the delay introduced due to the presence of a feedback path.

In a clock, the device has to switch its state back and forth. Thus the dynamics of the device has to be stable for a clock to function properly. Our simulated results showed that the clock made from our basic NOR element can switch states back and forth. In other words the dynamics of the NOR device is stable.

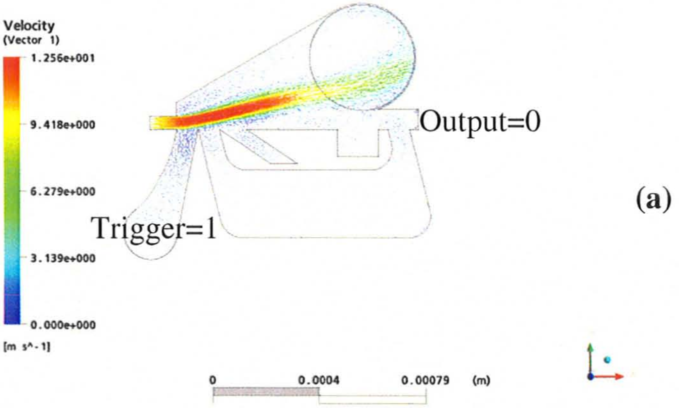

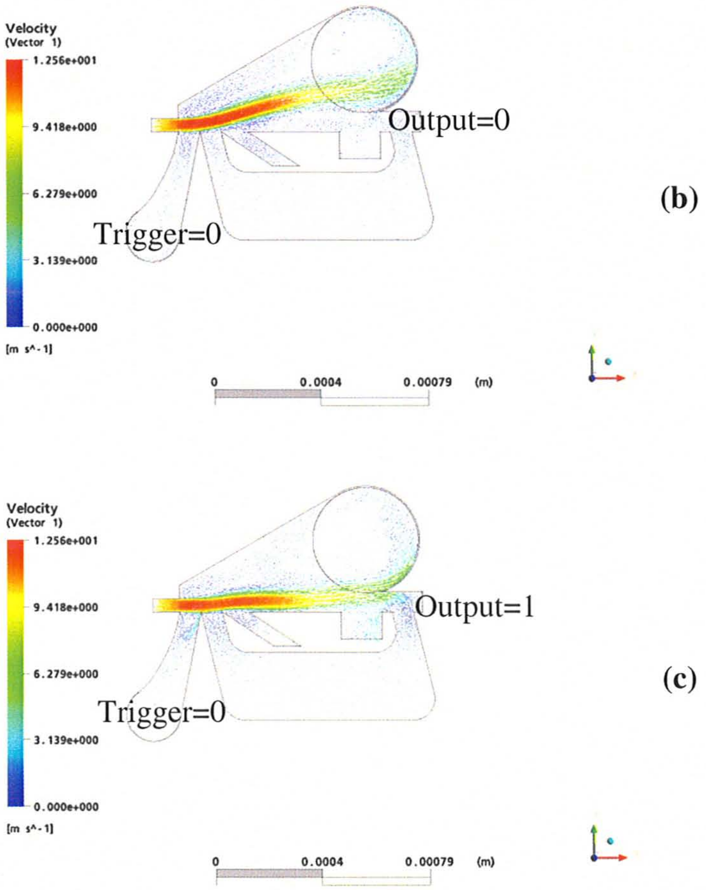

Figure 9-5: (a) Trigger=1, output =0 (b) Trigger=0, output=0 and (c) Trigger=0, output=1

Unger et. al. describes a peristaltic pump from three pneumatic valves arranged on a single channel [37]. Currently electrical signals are used to actuate the pneumatic valves. The actuation of the pneumatic valves using electrical signals requires transducers to convert the electrical signal into a pressure signal. Our clock however, can be used to actuate the peristaltic pumps without changing domains or even any further amplification.

9.3 LATCH

The output of combinational logic circuits such as a half adder is only a function of the current input states assuming that steady state is reached. But a computing system requires sequential logic circuits to store information [27-29]. In sequential circuits the output is a function of the present and past states. In other words a sequential circuit has a memory storing either a 1 or 0. Memories can be static or dynamic. A static memory preserves the state as long as the power is on. Static memories are useful when the register will not be updated for extended periods of time. Memories have a minimum of two stable states. Static memories use positive feedback to create a bistable circuit. In the absence of any triggering the circuit holds its previous state as long as the power is on. In order to change the stored value, a short time pulse is applied. For example in our simulations we applied a time pulse of 2ms. The positive feedback regenerates the effect of the trigger pulse and the circuit changes its state.

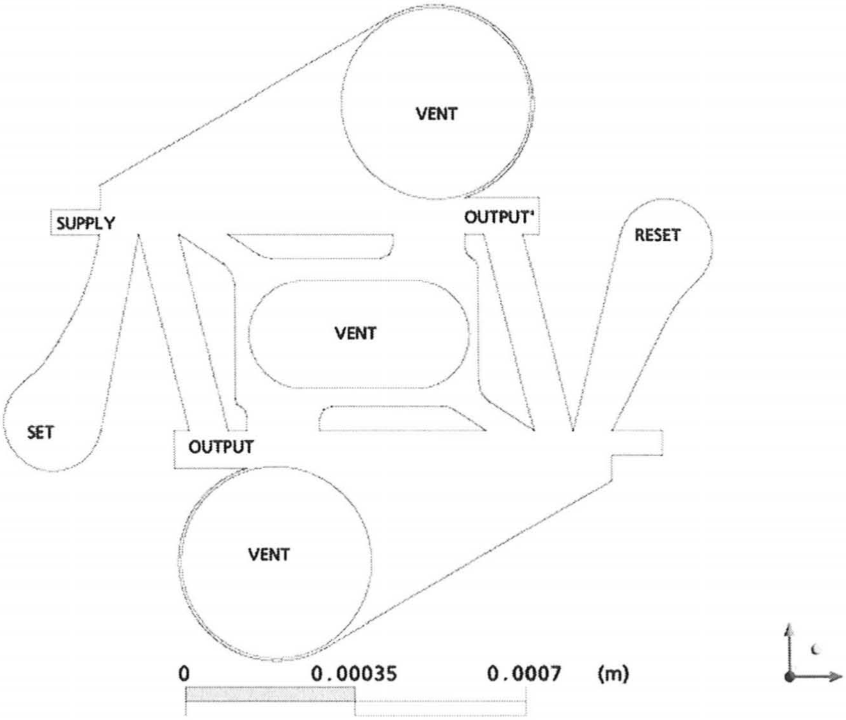

Figure 9-6: Microfluidic latch

Our designed microfluidic static memory is shown in Figure 9-6. It has two inputs: 'Set' and 'Reset'. The outputs are complementary. When both the inputs are zero the complementary outputs maintain their previous states. If a high pressure pulse is applied to 'Set', the output is forced to high. The state of the output can be changed to low by applying a high pressure pulse to 'Reset'.

We used transient simulations to simulate the latch. As mentioned before in Section 9.2, a simulator requires initial conditions for transient analysis. We obtained the initial conditions by applying a high pressure to 'Set'. Once the initial conditions were obtained, we applied the following step functions to 'Set' and 'Reset' respectively:

Set = b×step(t) - b×step(t-2)
Reset = b×step(t-4) - b×step(t-6)

Where t: time in ms
And b: 15KPa

The time was varied from 0-8ms in the time-steps of 0.02ms. Thus we obtained 400 time frames. Each of these time frames contains valuable information about the velocity and pressure profile. It is not possible to include the images of all the 400 time frames in this thesis. Thus, we have chosen to present the steady-state velocity profiles of the 4 important states of the latch.

In Figure 9-7 (a) a high pressure pulse applied to 'Set' makes the output high. Figure 9-7 (b) shows that when both the inputs 'Set' and 'Reset' are zero, the complementary outputs maintain their previous states. In Figure 9-7 (c) the output of the memory element is forced to low on applying a high pressure pulse to 'Reset'. Figure 9-7 (d) further emphasizes that when both the inputs 'Set' and 'Reset' are zero, the complementary outputs maintain their previous states.

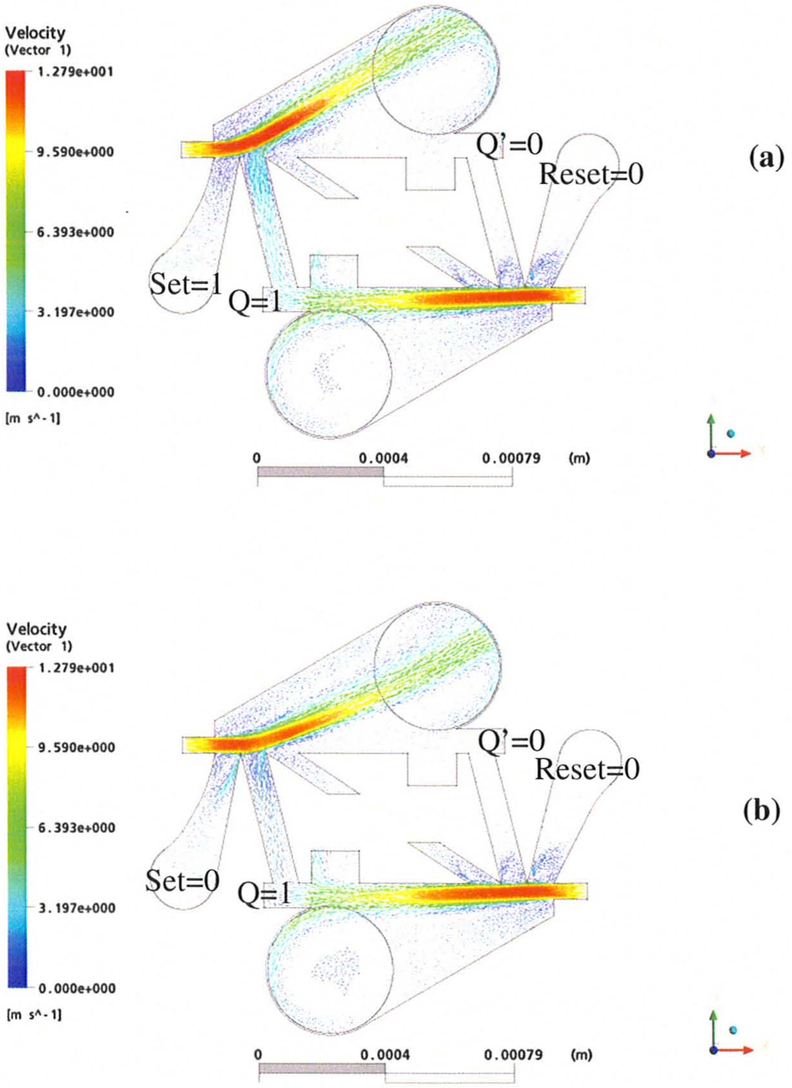

Figure 9-7: (a) Set=1, Reset=0, Q_{i-1}=0/1, Q_i=1 and Q_i'=0, (b) Set=0, Reset=0, Q_{i-1}=1, Q_i=1 and Q_i'=0

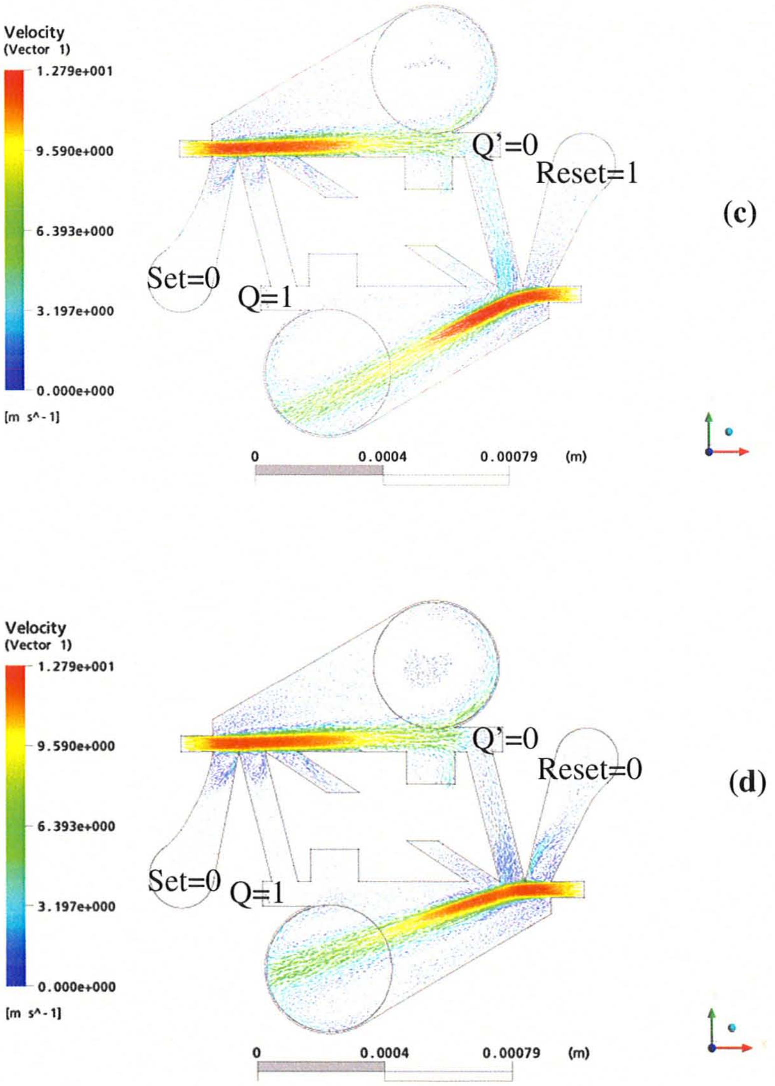

Figure 9-7: (c) Set=0, Reset=1, Q_{i-1}=0/1, Q_i=0 and Q_i'=1 (d) Set=0, Reset=0, Q_{i-1}=0, Q_i=0 and Q_i'=1

To summarize, a memory element was simulated. A memory element can be very useful for lab-on-a-chip systems. Any information can be stored in the memory element. The stored information can be read and used for further processes. It is also possible to change the stored information whenever it is required.

CHAPTER 10 CONCLUSIONS

10.1 DEVICE DESIGN AND CAPABILITIES

In this thesis a highly reliable microfluidic NOR with no-moving parts is presented, improving upon an early design introduced by Walker and Trask [8]. The basic principle of the device operation is the pressure-controlled jet deflection. We modeled our devices using a computational fluid dynamics software package called ANSYS-CFX. The fluid used for our models is water. The critical dimension of the device is 50μm, depth is 50μm and length is 19.5w where w is the critical dimension of the device. Our optimized device has a fan-out of greater than 12, non-linearity gain=4 at a supply pressure of 20KPa and a supply jet Reynolds number of 600. The device has a power consumption of 0.5mW. The frequency of the device is 1.25 KHz.

NOR is one of the universal gates. Thus simple Boolean laws and theorems can be used to express all logic functions as a combination of NORs. In Chapter 3 the several weaknesses, mistakes, deficiencies and omissions in the NOR element designed by Walker and Trask [8] were discussed. All those issues have been investigated in Chapter 7. Physical insights into the device operation were provided in Chapter 8.

In this project the three basic computing elements: a half adder, a clock and a memory element/ latch were also modeled. A half-adder is an essential component of Arithmetic Logic Unit (ALU) of a computer. A clock helps to synchronize the processes in a computing system. And the information of a state is stored using memory elements. These are discussed in Chapter 9.

Our designed NOR exhibits high non-linearity, high fan-out, isolation of input and output and compatibility of input and output signals. Therefore our microfluidic NOR serves as an excellent building block of a practical microfluidic computer. There are very few other examples of microdevices that meet these stringent requirements.

10.2 SUITABILITY FOR LAB-ON-A-CHIP

No on-chip computing is available for the current lab-on-a-chip systems. A general purpose and inexpensive computer is required for lab-on-a-chip systems. In this thesis we have investigated a microfluidic NOR gate. A NOR is one of the universal gates. Therefore we believe that a general purpose microfluidic computing system can be realized by using our designed microfluidic NOR elements. In this section the suitability of our microfluidic computing system for lab-on-a-chip systems is discussed.

The size of the current lab-on-a-chip is in the range of 50mm×35mm to 75mm×50mm [40]. Let us assume that about 10% of the chip area is devoted for the logic circuitry. Therefore the area available for the logic circuitry is in the range of 175mm^2 to 375mm^2. Thus on an average an area of ~275mm^2 is available for the logic circuitry. A simple CPU consists of a memory, a control register, a function decoder, an ALU, a clock, some circuitry to enable the CPU to *jump* automatically as a result of the previous decisions, a data bus and an address bus. An optimized NOR device of critical dimension 50μm has L×W×H as 1mm×1mm×50μm. A latch made from two NORs of critical dimension 50μm therefore, will occupy an area of 2mm^2. Thus a 10 bit memory and a 10 bit control register will occupy an area of 20mm^2 each. The function decoder will be a 10 bit de-multiplexer. A 2 bit de-multiplexer is a combination of 8 NORs. Therefore a 10 bit de-multiplexer will roughly occupy an area of 40mm^2. An ALU is a collection of many adders. A half adder made from a combination of five NORs of critical dimension 50μm will occupy an area of approximately 5mm^2. Let us assume that the designed ALU consists of 10 half adders. Therefore the ALU will occupy an area of 50mm^2. A clock will occupy an area of 1mm^2. An area of about 10mm^2 might be appropriate for the circuitry required to enable *jump* statements. Thus the total area occupied by a 10 bit memory, a 10 bit control register, a bit function decoder, an ALU, a clock and some additional circuitry made from a combination of NORs of critical dimension 50μm will occupy an area of approximately 140mm^2. Also, we have estimated that for the lab-on-a-chip systems an average area of ~275mm^2 is available for the logic circuitry. Therefore, we can scale our devices only up to a critical dimension 70μm.

The power consumption of the device with critical dimension of 50μm is 0.5mW. Thus the power consumption and the power density of a CPU with a 10 bit memory, a 10 bit control register, a bit function decoder, an ALU, a clock and some additional circuitry made from a combination of NORs of critical dimension 50μm will be 70mW and 0.5mW/mm^2 or 0.05W/cm^2. The maximum allowable power density for an electronic microprocessor with conventional cooling methods is ~10W/cm^2. Thus our devices can be scaled down to a critical dimension 8μm.

The pump power provides an incomplete story. When designing a pump, attention must be paid to the required pressure head. Thus the required supply pressure head should be considered to discuss the suitability of our devices for lab-on-a-chip systems. A NOR device of critical dimension of 50μm requires a supply pressure of 20KPa. A pressure of 20KPa can be easily provided by an off-chip pump. The output pressure of our optimized device is 16.5KPa. This pressure is high enough to actuate valves or drive peristaltic pumps without any amplification. A supply pressure of 100KPa (~1atm) seems to be a reasonable maximum pressure for lab-on-a-chip applications. Thus our devices can be scaled down to a critical dimension 25μm. Currently, off-chip pumps such as infusion pumps and piezoelectric pumps are capable of providing a pressure of 20KPa or more [38]. But peristaltic pumps and synthetic jet pumps are currently being explored to realize reliable on-chip pumps.

Our clock with a critical dimension 50μm has a frequency 1.25 KHz. The speed at which the reagents and buffer travel is in the range of 1mm/s to 10mm/s for lab-on-a-chip systems. Let us assume that the speed at which the reagent/buffer travel is 5mm/s. Let us also assume that the length of the channel through which the reagent/buffer has to travel is ~0.5mm. Therefore the time required by the reagent/buffer to travel from one end to the other end of the channel is 0.1s. Therefore a microfluidic computing system which can perform the computing operations at a speed of 10Hz will still be in par with the average speed available for the transport of reagents and buffer for lab-on-a-chip systems. A device of critical dimension of 500μm has a frequency of ~12.5Hz (Refer to Section 8.2). Thus our devices can be scaled up to 500μm to reduce the supply pressure without degrading the computational speed to below 10Hz.

A 10 bit memory when clocked with 1.25 KHz can transfer approximately 12.5Kbits/second. An ASCII is a 7 bit code. The normal typing speed is 60words/min. Let us assume that the maximum typing speed could be 180words/min. Therefore the minimum required bit rate is 21bits/second. Let us assume that we want to read the content of at least 10 registers (memory) 10 bits each in a second. Therefore a bit transfer rate of 125bits/second is required. Thus we can scale our devices up to a critical dimension 160μm.

Criteria	**Upper bound to satisfy the criteria (μm)**	**Lower bound to satisfy the criteria (μm)**
Area (≤1.4mm^2/NOR)	70	
Power density (≤10W/cm^2)		8
Supply pressure (≤100KPa)		25
Speed (≥12.5Hz)	500	
Bit transfer rate (≥125bits/s)	160	

Table 10-1: Summary of the upper and the lower bounds imposed on the choice of the critical dimension due to the available area, supply pressure, speed and bit transfer rate.

From Table 10-1 the critical dimension of our devices can only be in the range of 25µm to 70µm. The choice of simulating the devices of critical dimension 50µm was arbitrary at the beginning of this project. But at the end of this thesis we believe that a critical dimension 50µm lies in the range where a reasonable compromise among supply pressure, frequency, size and bits transfer per second is achieved.

To conclude a general purpose, small size, low power and high reliability microfluidic computer could have a major impact for the development of lab-on-a-chip systems. And this work is the first step towards the realization of such a microfluidic computer.

CHAPTER 11 FUTURE WORK

The immediate next work will be concentrated on fabricating the modeled devices and characterizing their performance experimentally. The aim of the experiments is to demonstrate a working device. At this stage of experiments, we would not take the factors such as roughness of the surface into consideration. Thus it is not necessary to fabricate the devices using the best available techniques. Instead, we would like to fabricate devices in the shortest time possible. Keeping these factors in consideration a flow for the fabrication of the devices is suggested in Figure 11-1 [30, 31].

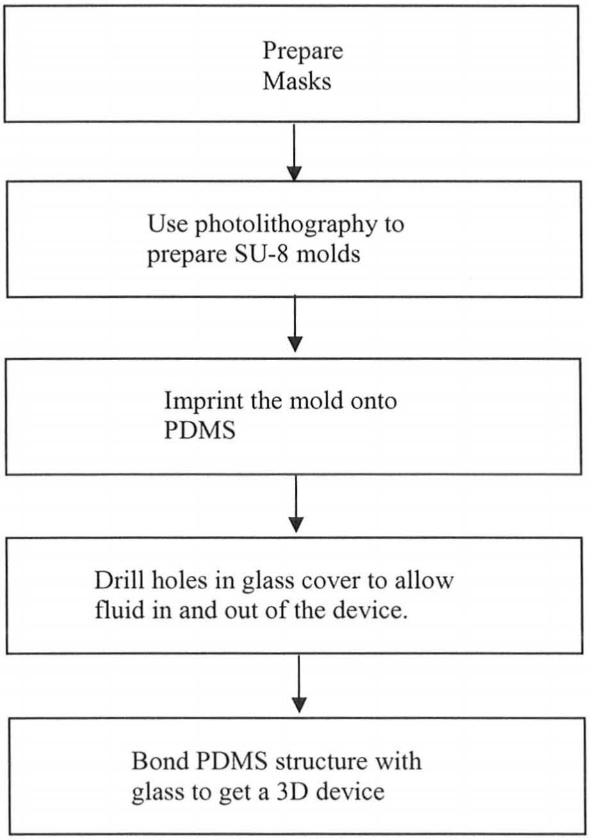

Figure 11-1: Fabrication flow chart

Our devices are 50μm in height. Thus it is hard to get vertical walls in silicon using wet-etching. If sloped-walled channels will be used, the critical dimension and therefore, the Reynolds number of fabricated device will be different from the modeled device. Therefore, vertical walls are preferred. Thus we proposed to use well-known PDMS fabrication methods. Also, the bonding strength of PDMS and glass is good [32]. High bonding strength between PDMS and glass will avoid the problem of fluid leakage during the experiments.

The fabricated devices will be tested for their pressure recovery, no-load mass flow rate, non-linearity in the transfer curves, output characteristic curve, input characteristic curve/ load line and fan-out at Re~600. An experimental set-up to test the fabricated devices is shown in Figure 11-2.

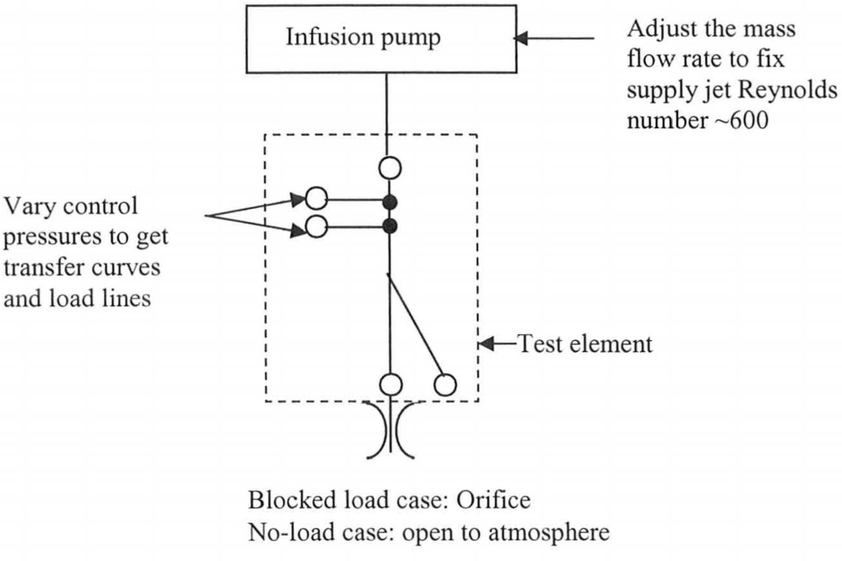

Figure 11-2: Possible experimental set-up

Usually, static pressure is measured using a pressure sensor. A pressure is connected to the place where pressure needs to be measured by a T-junction. A schematic of static pressure measurement is shown in Figure 11-3.

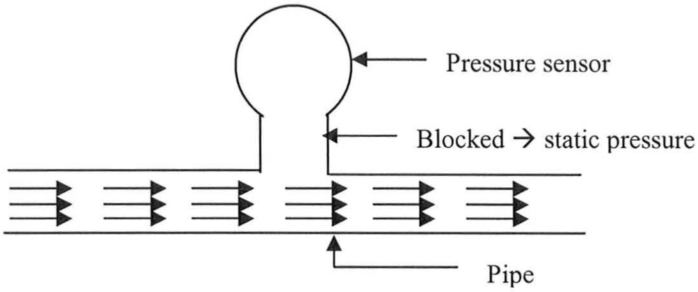

Figure 11-3: A schematic of static pressure measurement using pressure sensor

A vast majority of pressure sensors use piezoresistive sense elements to detect stress in a thin silicon diaphragm in response to a pressure load. Others use capacitive methods to sense the displacement of a thin diaphragm [33].

Mass-flow rate can be measured using a hot-wire anemometer as shown in Figure 11-4. It measures the fluid velocity by measuring the heat convected by the fluid. An anemometer consists of a platinum wire. The heat lost due to convection is a function of the fluid velocity [34].

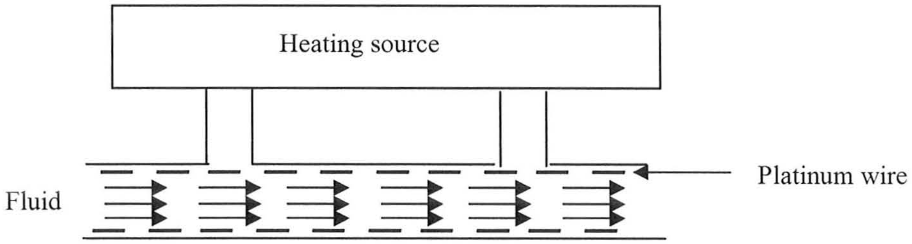

Figure 11-4: A schematic of mass flow measurement using hot-wire anemometer

The next goal will be to identify the transducers that will enable the various current operations available in the microfluidic domain to fit into the microfluidic logic circuits. It is believed that some of the transducers are already available but no one has thought of such integration. The output signal of the microfluidic logic circuitry is in the form of a pressure signal. This signal can either be used to display a user friendly message by using pressure-actuated LEDs or can serve as input for further operations.

For example in a hypothetical scenario, microfluidic logic circuits could be used to test the patient's blood sample to determine its pH value. A transducer could convert the pH level of the blood sample to a pressure signal. A Microfluidic comparator could be used to compare the obtained pressure signal against the base pressure signal. The output signal of the comparator can then be converted to a user-friendly signal by making use of pressure-actuated LEDs. Thus we need to develop a transducer which could convert the pH signal to a pressure signal. There exist materials which change their properties based on pH changes. These materials can be used to make valves which open/close based on pH value, thereby converting the pH signal to a microfluidic signal.

REFERENCES

1. K. Foster, G. Parker, *Fluidics: Components and Circuits*, New York: Wiley Interscience, 1970.
2. Joseph M. Kirshner, Silas Katz, *Design theory of Fluidic Components*, New York: Academic Press, 1975.
3. G.A. Parker, B. Jones '*Proceedings of Cranfield Fluidics Conference*', **2**, C3-29-C3-50 (1967).
4. B.J. Steptoe, *Proceedings of Cranfield Fluidics Conference*, **2**, B3-21-B3-32 (1967).
5. R.A. Oels, R.F. Boucher, E. Markland, *Proceedings of Cranfield Fluidics Conference*, 1, D3-45-D3-56 (1966).
6. N.M. Moris, *An Introduction to Fluid Logic*, London: McGraw-Hill, 1973.
7. Humphrey Tarumoto, *Fluidics*, Revised Edition, 1968.
8. M. Lucius Walker, Jr. and R. Pierce Trask, II, *Advances in Fluidics*, Edited by: Forbes T. Brown, The American Society of Mechanical Engineers, New York, 1967.
9. W. Zhan, R.M. Crooks, *Journal of American Chemical Society*, **125**, 9934-9935 (2003).
10. Tor Vestad, David W.M. Marr, Toshinori Munakata, *Applied Physics Letters*, **84**, 5074-5075 (2004).
11. N. Pye, M McCormick, E Chowanietz, *International symposium on flow visualization*, **9**, 404-1-404-10 (2000).
12. N. Pye, M McCormick, E Chowanietz, M. Harper, M. Goodwin, *Microsystem Technologies*, **4**, 197-200 (1998).
13. M.M. Athavale, H.Y. Li, A.J. Przekwas, B.H. Piekarski, R.J. Zeto and S.M. Tenney, *Technical Proceedings of the International Conference on Modeling and Simulation of Microsystems (MSM),* 522-527 (1998).

14. Tae-Hyun Kim, Chang-Ho Cho, Dong-Il Dan Cho, *Journal of Micromechanical and Microengineering*, **8**, 7-14 (1998).
15. Alex Groisman, Markus Enzelberger, Stephen R. Quake, *Science*, **300**, 955-958 (2003).
16. Patrick Tabeling, *Introduction to Microfluidics*, First Edition, New York: Oxford University Press Inc., 2005.
17. M. Morris Mano, *Digital Logic and Computer Design*, Prentice Hall, 1979.
18. Walter A. Triebel, *Integrated Digital Electronics*, Toronto: Prentice-Hall of Canada, Ltd., 1979.
19. Rainer Waser, *Nanoelectronics and Information Technology*, Second corrected edition. Germany: Wiley-VCH Verlag GmbH & Co. KGaA, 2005.
20. Robert W. Keyes, *Proceedings of the IEEE*, **69**, 2, 267-278 (1981).
21. Robert W. Keyes, *Reviews of Modern Physics*, **61**, 2, 279-297 (1989).
22. Robert W. Keyes, *Science*, **230**, 138-144 (1985).
23. Vojin G. Oklobdzija, *High-performance system design: Circuits and Logic*, IEEE press, 1999.
24. ANSYS-CFX user manuals.
25. Harry R. Nara, *Vector Mechanics for Engineers*, New York: Wiley, 1962
26. B. Cheng, S. Roy, A. Asenov, *Solid-state circuits conference*, 219-222 (2004)
27. Jan M. Rabaey, Anantha Chandrakasan and Borivoje Nikolic, *Digital Integrated Circuits: A design Perspective*, Second Edition, Prentice Hall, 2003.
28. Donald A. Neamen, *Electronic circuit analysis and design*, Second Edition, McGraw Hill, 2001.
29. Masakazu Shoji, *CMOS digital circuit technology*, Prentice Hall, 1988.
30. Stephen D. *Senturia, Microsystem Design, Fifth printing*, London: Kluwer Academic publishers, 2003.
31. Gregory T.A. Kovacs, *Micromachined Transducers Sourcebook*, Toronto: WCB McGraw-Hill, 1998.

32. Shantanu Bhattacharya, Arindom Dutta, Jordan M. Berg, and Shubhra Gangopadhyay, *Journal of Microelectromechanical systems*, 14, 3, 590-597 (2005).
33. Nadim Maluf, *An introduction to Microelectromechanical Systems Engineering*, Artech house, Inc., 2000.
34. H.H. Bruun, *Hot-wire anemometry: principles and signal analysis*, Oxford science publications, 1995.
35. Arthur W. Lo, *IRE Transactions on Electronic Computers*, 416-425 (1961).
36. Donald F. Young, Bruce R. Munson, Theodore H. Okiishi, *A brief introduction to fluid mechanics*, John Wiley & sons, Inc., 2004.
37. Marc A. Unger, Hou-Pu Chou, Todd Thorsen, Axel Scherer, Stephen R. Quake, *Science*, **288**, 113-116 (2000).
38. D J Laser and J G Santiago, *Journal of Micromechanical Microengineering*, **14**, R35-R64 (2004).
39. Sedra and Smith, *Microelectronic Circuits*, Oxford University Press, 4th edition, 1998.
40. Duane Lindner, *Lab on a Chip*, **1**, Issue: 1, pp. 15N - 20N (2001).

APPENDIX

The simulator assumes a parabolic velocity profile for the constant pressure boundary condition. A comparison of the velocity profile at the supply for constant pressure and constant supply are shown in Figure A-1.

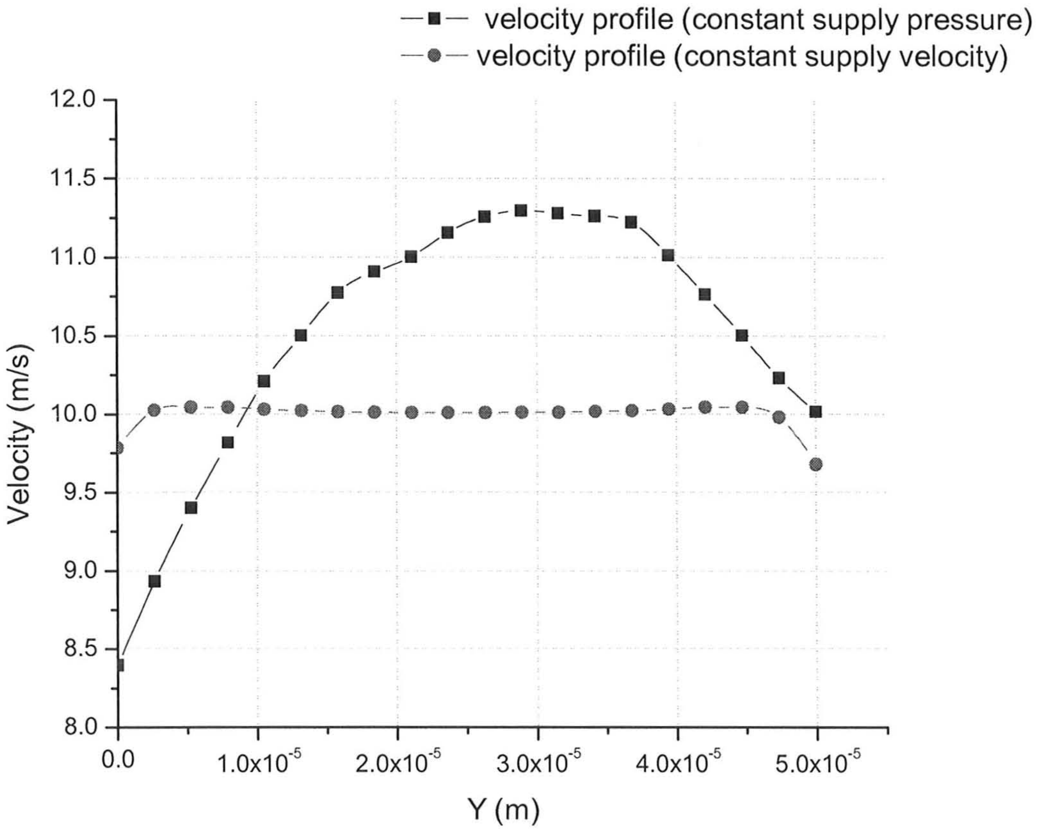

Figure A-1: Supply velocity profile at constant supply pressure and constant supply velocity

In the experiments we do not expect a parabolic velocity profile even on applying a constant pressure at the supply. Thus constant pressure boundary condition at the supply might not be realistic boundary conditions for the simulations.